DEVELOPMENT OF DATA DRIVEN MODELS TO PREDICT PRESSURE DROP IN

WIRE-WRAPPED ROD BUNDLES

A Dissertation

by

GABRIEL CAIO QUEIROZ TOMAZ

Submitted to the Graduate and Professional School of
Texas A&M University
in partial fulfillment of the requirements for the degree of

DOCTOR OF PHILOSOPHY

Chair of Committee,	Yassin Hassan
Committee Members,	Rodolfo Vaghetto
	Victor Ugaz
	Debjyoti Banerjee
Head of Department,	Guillermo Aguilar

May 2022

Major Subject: Mechanical Engineering

ABSTRACT

The Generation IV reactors (Gen IV) are a set of new designs of nuclear reactors under development by a consortium of counties to meet the energy necessities of the future, including sustainability, safety, and economic feasibility. The liquid metal fast reactor design (LMFRs) is one of the most prominent Gen VI options. Liquid metal is has a large thermal conductivity, allowing for a significant power density. Moreover, in opposition to the traditional water reactors, LMFRs operate at near atmospheric pressures as metals have a high boiling temperature. One of the most common fuel designs for LMFRs is the tightly packed wire-wrapped rod bundle. The wires around the fuel pins keep the distance between the rods, contribute to the flow mixing, homogenize the temperature field, and increase the flow friction. Thus, the knowledge of the pressure drop through the bundle and the flow split across the flow area is fundamental in the design of LMFR reactors. The first part of this work presents a recalibration of the UCTD correlation for friction factor in wire-wrapped rod bundles using Multi-Objective Genetic Algorithm in the turbulent regime, improving its prediction of the flow split. When applying this methodology to the laminar regime, this study identified that the laminar data available in the literature is insufficient to extend this method to this regime. The second part of this work presents a dataset of 93 CFD simulations of laminar flows in wire-wrapped rod bundles. The data includes the friction factor and the flow split between the interior, edge, and corner regions for bundles with 7 to 91 pins. This publication also presents an ANN-based model to predict these flow parameters based on the CFD dataset. The accuracy of the predictions is verified with a dataset of experimental data collected from the open literature composed of 42 bundles.

DEDICATION

I dedicate this work to the women who provided me support, fulfillment, and genuine joy: my

mother, wife, and daughter.

ACKNOWLEDGMENTS

I want to say thanks to my advisor Dr. Yassin Hassan. His support, motivation, and faith were indispensable to the success of this work. Doing research with Dr. Hassan was a breathtaking experience of learning, hard work, and growth. I would also like to thank the other members of my committee: Dr. Rodolfo Vaghetto, Dr. Victor Ugaz, and Dr. Debjyoti Banerjee, for their input and dedication. I have acknowledged the importance of Dr. Yu Min Chen to this work for his collaboration. I am also thankful to Dr. Thien Nguyen for his commitment to my learning. I am grateful to Dr. André Campagnole for the friendship and his mentorship during a long extent of my journey in science. I want to thank Sero Yang, Beth Nam, Marilyn Delgado, Vasileios Kyrialopoulos, Alessandro Vanni, and Merinda Voila for their friendship during the exceptional time I spent doing this research.

I am incredibly grateful to my wife Camila Matozinhos for being a wonderful woman and partner. I also feel enormously lucky for the fantastic mother she is. Moreover, I am thankful for her vital support on Computational Fluid Dynamics.

CONTRIBUTORS AND FUNDING SOURCES

TABLE OF CONTENTS

LIST OF FIGURES

ix

LIST OF TABLES

1. INTRODUCTION

The Liquid Metal Fast Reactor (LMFR) is one of the leading designs proposed by the Generation VI International Forum. Of of the fuel designs often considered for LMFR is the wire-wrapped rod bundle. The rods are tightly packed inside a hexagonal duct. The rods have wires around in a helical trajectory, providing mechanical support to the bundle and mixing the flow, enhancing heat transfer and temperature homogenization. However, the presence of the wires also increases the resistance to the flow, requiring more pumping power.

In order to better understand the thermal-hydraulic characteristics of this design, extensive experimental and numerical studies have been conducted. Merzari et al. [5] simulated a heated 37-pin rod bundle with wall solved large edge simulation (LES). Brockmeyer et al. [6] coupled CFD with finite elements to study flow-induced vibrations in a 7-pin wire-wrapped rod bundle. Recent advancements in flow visualization techniques allowed the measurements of velocity fields in regions not accessible before. Goth et al. [7] used matched-index-of-refraction (MIR) between the fluid and bundle to measure turbulent flows inside a 61-pin rod bundle using particle image velocimetry (PIV), with these results being later compared with CFD using large edge simulation [8]. Song et al. [9] used another combination of MIR materials to take PIV measurements in the edge and corner subchannels and compared the velocity fields and pressure drop measurements with CFD simulations. Childs et al. [10] analyzed the effects of blockages of different sizes in different locations in the friction factor.

One of the flow parameters of primary interest in rod bundles is the pressure drop. Since the conception of reactors with wire-wrapped rod bundles, several experiments were performed to support the development of pressure drop correlations, pioneered by Rehme [11], Baumann [12], and Reihman [13]. Novendstern [14], Rehme [15] and Engel [16] proposed the first widely used correlations.

The Cheng and Todreas correlation (CTD) was proposed in 1986 [17] and became the most used correlation for pressure drop in wire-wrapped rod bundles. The correlation was updated in

1

2013 [18] to improve its predictions for the transition region. In 2018 the Upgraded CTD (UCTD) was published [19], updating the laminar boundary equation, recalibrating the equation for the transition region, and expanding its validity range to 7-pin bundles by correcting the pin number effect.

The UCTD correlation is robust to evaluate pressure drop and flow split. It is currently the reference correlation to analyze the pressure drop in wire-wrapped rod bundles. However, gaps persist. First, the accuracy of UCTD for the flow split across the bundle regions should be improved for licensing. The fluid's heterogeneity of the flow velocity is directly related to the incidence of hot spots in the bundle, so the flow split is a primary concern.

Moreover, the industry and regulators are increasingly interested in the flow characteristics of the laminar regime. Many designs rely on natural circulation to provide cooling in emergency scenarios. Since most studies were concerned with the normal operation of the reactor, there is a lack of data available in the literature for the laminar flow.

The first objective of this work is to recalibrate the UCTD [19] correlation improving its accuracy when predicting the friction factor of the different regions in the rod bundle, thus improving the predictions of the flow split. The UCTD coefficients were recalculated using Multi-Objective Genetic Algorithms. It is demonstrated that UCTD is improved for the turbulent regime by decreasing the error for the flow split prediction while keeping the accuracy of the bundle average friction factor similar. However, the results for the laminar regime point to the fact that the limited number of experiments available in the laminar regime, especially with flow split data, limits the correlation formulation's complexity and leads the optimization process to overfit.

The second objective of this work is to create a new dataset of flows in wire-wrapped rod bundles in the laminar regime using Computational Fluid Dynamics (CFD) and develop a high order model based on Artificial Neural Networks (ANN). The new dataset has 93 simulated bundles dispersed through a more extensive range of pitch to diameter ratio (P/D) and height-to-diameter ratio (H/D) and contains flow split data for all the cases there are only three experimental bundles known to have flow split data. The ANN model is highly accurate at representing the numerical

results. Moreover, the ANN predictions of the experimental data are accurate.

2. OPTIMIZATION OF THE UCTD CORRELATION USING GENETIC ALGORITHMS*

2.1 UCTD Correlation for friction factor

The UCTD correlation predicts the friction factor for all flow regimes, from laminar to fully turbulent. The friction factor constant is calculated as $C_{fiT} = f_i \times Re_i^m$, with $m = 0.18$ for fully turbulent flows and $m = 1$ in the laminar regime. The subscript i refers to the bundle region, being $i = 1, 2, 3$ for interior, edge and corner regions respectively. The index $i = b$ is used when the quantity is respective to the average of the whole bundle. Fig. 2.1 shows the typical geometry of a wire-wrapped rod bundle.
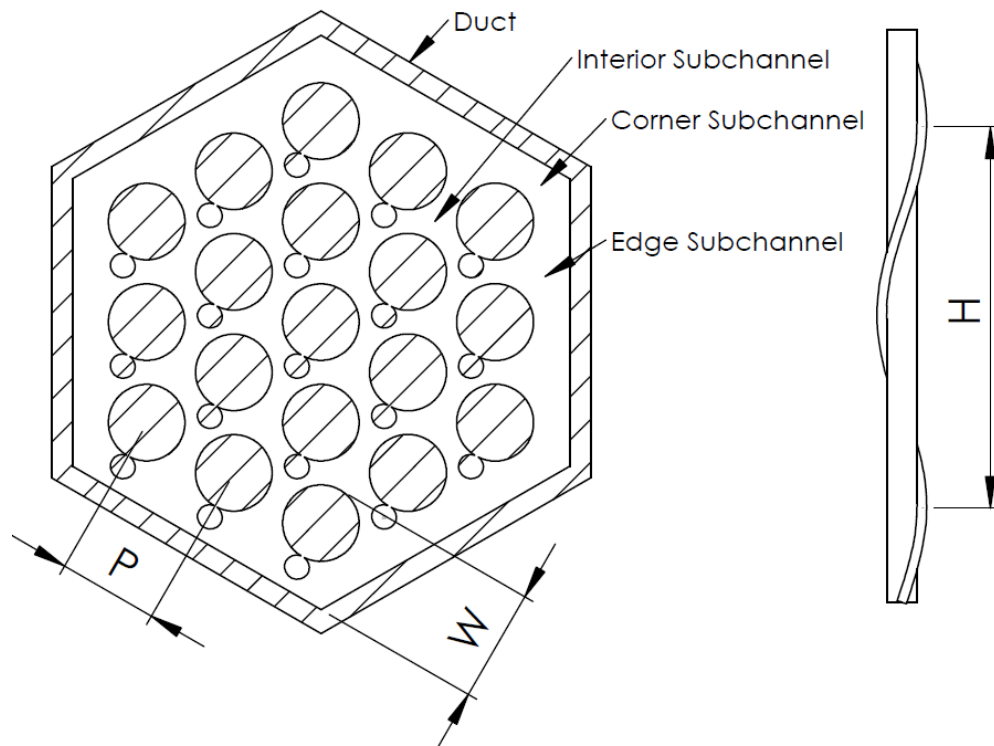
Figure 2.1: Wire-wrapped rod bundle geometry.

2.1.1 UCTD formulation for the fully turbulent regime

Equations 2.1, 2.2 and 2.3 are used to calculate the friction factor constant for the three types of subchannel. By considering the balance of mass, the bundle average friction factor for the turbulent regime (C_{fbT}) can be calculated from the constants of each region as in Eq. 2.4. The coefficients C'_{fiT} are the bare rod subchannel friction factor constants, P_w and P'_w are the wetted perimeters for the wired and the bare bundles, respectively, A_r is the projected area of the wire, A' is the average cross-sectional area of the bare bundle, De is the hydraulic diameter and D_w is the diameter of the wire. The UCTD publication [19] provides the full description of how the geometrical parameters are computed.

$$C_{f1T} = C'_{f1T} \left(\frac{P'_{w1}}{P_{w1}} \right) + W_{dT} \left(\frac{3A_{r1}}{A'_1} \right) \left(\frac{De_1}{H} \right) \left(\frac{De_1}{D_w} \right)^{0.18} \tag{2.1}$$

$$C_{f2T} = C'_{f2T} \left(1 + W_{sT} \left(\frac{A_{r2}}{A'_2} \right) tan^2\theta \right)^{1.41} \tag{2.2}$$

$$C_{f3T} = C'_{f3T} \left(1 + W_{sT} \left(\frac{A_{r3}}{A'_3} \right) tan^2\theta \right)^{1.41} \tag{2.3}$$

$$C_{fbT} = De_b \left(\sum_{i=1}^{3} \left(\frac{N_i A_i}{A_b} \right) \left(\frac{De_i}{De_b} \right)^{0.0989} \left(\frac{De_i}{C_{fiT}} \right)^{0.54945} \right)^{-1.82} \tag{2.4}$$

Compared to the bare bundle, the wrapped wire on the rods will cause energy loss. The wire drag constant (W_d) correlates the friction increase for the interior subchannels, and the wire sweeping constant (W_s) does the respective for the edge and corner subchannels. Equations 2.5 and 2.6 show how W_d and W_s are calculated for the fully turbulent regime. The coefficients C_1, C_2, C_3, C_4, a and b are them calibrated with experimental data.

$$W_{dT} = \left(C_1 + C_2 \left(\frac{D_w}{D} \right) + C_3 \left(\frac{D_w}{D} \right)^2 \right) \left(\frac{H}{D} \right)^{C_4} \tag{2.5}$$

$$W_{sT} = a \log \left(\frac{H}{D} \right) + b \tag{2.6}$$

2.1.2 UCTD formulation for the laminar and transition regime

The friction factor constants in the laminar regime are calculated with Equations 2.7, 2.8, 2.9 and 2.10. For the laminar flow, the drag (W_{dL}) and sweeping (W_{sL}) constants are assumed to be proportional to W_{dT} and W_{sT} as in Equations 2.11 and 2.12. The coefficients C_d and C_s define this proportionality. In the original correlation, C_d is derived analytically to be 1.4 [17], then C_s is found empirically.

$$C_{f1L} = C'_{f1L} \left(\frac{P'_{w1}}{P_{w1}} \right) + W_{dL} \left(\frac{3A_{r1}}{A'_1} \right) \left(\frac{De_1}{H} \right) \left(\frac{De_1}{D_w} \right) \tag{2.7}$$

$$C_{f2L} = C'_{f2L} \left(1 + W_{sL} \left(\frac{A_{r2}}{A'_2} \right) tan^2\theta \right) \tag{2.8}$$

$$C_{f3L} = C'_{f3L} \left(1 + W_{sL} \left(\frac{A_{r3}}{A'_3} \right) tan^2\theta \right) \tag{2.9}$$

$$C_{fbL} = De_b \left(\sum_{i=1}^{3} \left(\frac{N_i A_i}{A_b} \right) \left(\frac{De_i}{De_b} \right) \left(\frac{De_i}{C_{fiL}} \right) \right)^{-1} \tag{2.10}$$

$$W_{dL} = C_d \cdot W_{dT} \tag{2.11}$$

$$W_{sL} = C_s \cdot W_{sT} \tag{2.12}$$

$$f_i = \begin{cases} \dfrac{C_{fiL}}{Re}, & \text{if } Re_b < Re_{bL} \\[2ex] \dfrac{C_{fiT}}{Re^{0.18}}, & \text{if } Re_b > Re_{bT} \\[2ex] \dfrac{C_{fiL}}{Re}\left(1 - \psi_i\right)^{1/3}\left(1 - \psi_i^\lambda\right) + \dfrac{C_{fiT}}{Re^{0.18}} \cdot \psi_i^{1/3}, & \text{if } Re_{bL} \le Re_b \le Re_{bT} \end{cases} \tag{2.13}$$

$$Re_{bL} = 320 \left(10^{\left(\frac{P}{D}-1\right)}\right) \tag{2.14}$$

$$Re_{bT} = 10{,}000 \left(10^{0.7\left(\frac{P}{D}-1\right)}\right) \tag{2.15}$$

The friction factor in the transition regime is calculated with Eq. 2.16, where $\lambda = 7$ and ψ is the intermittency parameter defined by Eq. 2.17.

$$f_{iTr} = f_{iL}\left(1 - \psi_i\right)^{1/3}\left(1 - \psi_i^\lambda\right) + f_{bT} \cdot \psi_i^{1/3} \tag{2.16}$$

$$\psi_i = log\left(\frac{Re_i}{Re_{iL}}\right) / log\left(\frac{Re_{iT}}{Re_{iL}}\right) \tag{2.17}$$

2.1.3 Flow splitting calculation

The flow split parameter can be calculated from the friction factor in each subchannel type, assuming the pressure difference equal for all subchannels and the conservation of mass. In this case, the relative velocity in each region is adjusted. The CTD publication [2] presents the derivation of the flow split parameters from the assumptions above. The flow split parameters are calculated using Equations 2.19, 2.18 and 2.20.

$$X_2 = 1/(S_2 + (X_1/X_2)S_1 + (X_3/X_2)S_3) \tag{2.18}$$

$$\frac{X_1}{X_2} = \left(\frac{De_1}{De_2}\right)^{(1+m)/(2-m)} \left(\frac{C_{f2}}{C_{f1}}\right)^{1/(2-m)} \tag{2.19}$$

$$\frac{X_3}{X_2} = \left(\frac{De_3}{De_2}\right)^{(1+m)/(2-m)} \left(\frac{C_{f2}}{C_{f3}}\right)^{1/(2-m)} \tag{2.20}$$

2.2 Recalibration Methodology

2.2.1 Experimental Dataset

The recalibration process was performed based on the data available in the scientific literature. The bundle average friction factor data originated from 159 different experiments. From those, 80 bundles are the same used to recalibrate UCTD, and details of these experiments are presented by Chen et al. [19]. The data from the other 79 bundles was obtained from other experiments [21, 4, 22, 23, 24, 25, 26, 27, 28, 29, 30, 31, 32, 2, 9, 33], summarized in Tab. 2.1. The column $Group$ indicates what flow regimes the bundle has data in. The terms L, Tr, and T indicates data in the laminar, transition and turbulent regimes, respectively.

Table 2.1: Bundles not included in the UCTD development but considered in this study.

ID	Year	N_r	D (mm)	D_w (mm)	P/D	W/D	H/D	Group
Rehme11b	1967	19	12	1.5	1.125	1.125	8.33	TrT
Rehme11c	1967	37	12	1.5	1.125	1.125	8.33	TrT
Rehme11d	1967	61	12	1.5	1.125	1.125	8.33	TrT
Rehme12b	1967	19	12	1.5	1.125	1.125	12.5	TrT
Rehme12c	1967	37	12	1.5	1.125	1.125	12.5	TrT
Rehme12d	1967	61	12	1.5	1.125	1.125	12.5	TrT
Rehme13b	1967	19	12	1.5	1.125	1.125	16.67	TrT
Rehme13c	1967	37	12	1.5	1.125	1.125	16.67	TrT
Rehme13d	1967	61	12	1.5	1.125	1.125	16.67	TrT
Rehme14b	1967	19	12	1.5	1.125	1.125	25	TrT

Table 2.1 continued from previous page

ID	Year	N_r	D (mm)	D_w (mm)	P/D	W/D	H/D	Group
Rehme14c	1967	37	12	1.5	1.125	1.125	25	TrT
Rehme14d	1967	61	12	1.5	1.125	1.125	25	TrT
Rehme15b	1967	19	12	1.5	1.125	1.125	50	TrT
Rehme15c	1967	37	12	1.5	1.125	1.125	50	TrT
Rehme15d	1967	61	12	1.5	1.125	1.125	50	TrT
Rehme21a	1967	7	12	2.8	1.233	1.233	8.33	TrT
Rehme21b	1967	19	12	2.8	1.233	1.233	8.33	TrT
Rehme21c	1967	37	12	2.8	1.233	1.233	8.33	TrT
Rehme22a	1967	7	12	2.8	1.233	1.233	12.5	TrT
Rehme22b	1967	19	12	2.8	1.233	1.233	12.5	TrT
Rehme22c	1967	37	12	2.8	1.233	1.233	12.5	TrT
Rehme23a	1967	7	12	2.8	1.233	1.233	16.67	TrT
Rehme23b	1967	19	12	2.8	1.233	1.233	16.67	TrT
Rehme23c	1967	37	12	2.8	1.233	1.233	16.67	TrT
Rehme24a	1967	7	12	2.8	1.233	1.233	25	TrT
Rehme24b	1967	19	12	2.8	1.233	1.233	25	TrT
Rehme24c	1967	37	12	2.8	1.233	1.233	25	TrT
Rehme25a	1967	7	12	2.8	1.233	1.233	50	TrT
Rehme25b	1967	19	12	2.8	1.233	1.233	50	TrT
Rehme25c	1967	37	12	2.8	1.233	1.233	50	TrT
Rehme31a	1967	7	12	3.3	1.275	1.275	8.33	TrT
Rehme31b	1967	19	12	3.3	1.275	1.275	8.33	TrT
Rehme31c	1967	37	12	3.3	1.275	1.275	8.33	TrT
Rehme32a	1967	7	12	3.3	1.275	1.275	12.5	TrT
Rehme32b	1967	19	12	3.3	1.275	1.275	12.5	TrT

Table 2.1 continued from previous page

ID	Year	N_r	D (mm)	D_w (mm)	P/D	W/D	H/D	Group
Rehme32c	1967	37	12	3.3	1.275	1.275	12.5	TrT
Rehme33a	1967	7	12	3.3	1.275	1.275	16.67	TrT
Rehme33b	1967	19	12	3.3	1.275	1.275	16.67	TrT
Rehme33c	1967	37	12	3.3	1.275	1.275	16.67	TrT
Rehme34a	1967	7	12	3.3	1.275	1.275	25	TrT
Rehme34b	1967	19	12	3.3	1.275	1.275	25	TrT
Rehme34c	1967	37	12	3.3	1.275	1.275	25	TrT
Rehme35a	1967	7	12	3.3	1.275	1.275	50	TrT
Rehme35b	1967	19	12	3.3	1.275	1.275	50	TrT
Rehme35c	1967	37	12	3.3	1.275	1.275	50	TrT
Rehme41a	1967	7	12	4.1	1.343	1.343	8.33	TrT
Rehme41b	1967	19	12	4.1	1.343	1.343	8.33	TrT
Rehme42a	1967	7	12	4.1	1.343	1.343	12.5	TrT
Rehme42b	1967	19	12	4.1	1.343	1.343	12.5	TrT
Rehme42c	1967	37	12	4.1	1.343	1.343	12.5	TrT
Rehme43a	1967	7	12	4.1	1.343	1.343	16.67	TrT
Rehme43b	1967	19	12	4.1	1.343	1.343	16.67	TrT
Rehme43c	1967	37	12	4.1	1.343	1.343	16.67	TrT
Rehme44a	1967	7	12	4.1	1.343	1.343	25	TrT
Rehme44b	1967	19	12	4.1	1.343	1.343	25	TrT
Rehme44c	1967	37	12	4.1	1.343	1.343	25	TrT
Rehme45a	1967	7	12	4.1	1.343	1.343	50	TrT
Rehme45b	1967	19	12	4.1	1.343	1.343	50	TrT
Rehme45c	1967	37	12	4.1	1.343	1.343	50	TrT
Rehme51a	1967	7	12	5	1.417	1.417	8.33	TrT

Table 2.1 continued from previous page

ID	Year	N_r	D (mm)	D_w (mm)	P/D	W/D	H/D	Group
Rehme51b	1967	19	12	5	1.417	1.417	8.33	TrT
Rehme51c	1967	37	12	5	1.417	1.417	8.33	TrT
Rehme52a	1967	7	12	5	1.417	1.417	12.5	TrT
Rehme52b	1967	19	12	5	1.417	1.417	12.5	TrT
Rehme52c	1967	37	12	5	1.417	1.417	12.5	TrT
Rehme53a	1967	7	12	5	1.417	1.417	16.67	TrT
Rehme53b	1967	19	12	5	1.417	1.417	16.67	TrT
Rehme53c	1967	37	12	5	1.417	1.417	16.67	TrT
Rehme54a	1967	7	12	5	1.417	1.417	25	TrT
Rehme54b	1967	19	12	5	1.417	1.417	25	TrT
Rehme54c	1967	37	12	5	1.417	1.417	25	TrT
Rehme55a	1967	7	12	5	1.417	1.417	50	TrT
Rehme55b	1967	19	12	5	1.417	1.417	50	TrT
Rehme55c	1967	37	12	5	1.417	1.417	50	TrT
Baumann1	1968	61	6	1	1.167	1.167	16.7	T
Baumann2	1968	61	6	1	1.167	1.167	25	T
Baumann3	1968	19	6.62	1.5	1.227	1.227	15.1	T
Baumann4	1968	19	6.62	1.5	1.227	1.227	22.7	T
Reihman1	1969	37	6.756	0.406	1.079	1.1	22.56	TrT
Reihman10	1969	217	6.35	0.762	1.135	1.143	48	TrT
Reihman11	1969	37	7.62	0.914	1.15	1.178	40	TrT
Reihman12	1969	19	6.35	0.762	1.156	1.184	48	TrT
Reihman13	1969	37	6.35	0.762	1.148	1.171	96	TrT
Reihman14	1969	37	4.978	0.597	1.145	1.158	61.22	TrT
Reihman2	1969	37	6.756	0.406	1.079	1.1	45.11	TrT

Table 2.1 continued from previous page

ID	Year	N_r	D (mm)	D_w (mm)	P/D	W/D	H/D	Group
Reihman3	1969	37	6.35	0.762	1.148	1.171	12	TrT
Reihman4	1969	37	6.35	0.762	1.148	1.171	24	TrT
Reihman5	1969	37	6.35	0.762	1.148	1.171	48	TrT
Reihman6	1969	37	6.096	1.016	1.196	1.22	50	TrT
Reihman7	1969	37	5.994	1.08	1.215	1.24	50.85	TrT
Reihman8	1969	37	6.35	2.012	1.376	1.434	24	TrT
Reihman9	1969	37	6.35	2.012	1.376	1.434	48	TrT
FFTF$_A NL$	1970	217	5.84	1.42	1.243	1.35	52.17	TrT
Okamoto1	1970	19	6.3	1.2	1.221	1.117	40.48	TrT
Okamoto2	1970	91	6.3	1.2	1.221	1.117	40.48	TrT
Davidson	1971	217	6.39	1.808	1.283	1.283	48	T
Grazzini	1971	91	6.68	1.2	1.18	1.206	23.952	T
Wakasugi1	1971	91	6.3	1.2	1.221	1.167	14.286	TrT
Wakasugi2	1971	91	6.3	1.2	1.221	1.167	20.635	TrT
Wakasugi3	1971	91	6.3	1.2	1.221	1.167	30.159	TrT
Wakasugi4	1971	91	6.3	1.2	1.221	1.167	41.27	TrT
Hoffmann1	1973	61	6	1.9	1.317	1.317	16.67	T
Hoffmann2	1973	61	6	1.9	1.317	1.317	33.3	T
Hoffmann3	1973	61	6	1.9	1.317	1.317	50	T
Chiu1	1979	61	12.73	0.8	1.067	1.069	8	Tr
Chiu2	1979	61	12.73	0.8	1.067	1.069	4	Tr
Engel	1979	61	12.85	0.94	1.082	1.08	7.7821	LTrT
Burns	1980	37	12.72	1.91	1.156	1.177	21	LT
Spencer	1980	217	5.84	1.42	1.252	1.242	51.74	TrT
Carelli	1981	61	12.7	0.635	1.05	1.05	20	TrT

Table 2.1 continued from previous page

ID	Year	N_r	D (mm)	D_w (mm)	P/D	W/D	H/D	Group
Itoh1	1981	91	6.3	1.27	1.216	1.216	15.03	TrT
Itoh2	1981	91	6.3	1.27	1.216	1.216	22.54	TrT
Itoh3	1981	91	6.3	1.27	1.216	1.216	32.22	TrT
Itoh4	1981	91	6.3	1.27	1.216	1.216	45.08	TrT
Itoh5	1981	127	5.5	0.9	1.176	1.178	38	LTrT
Itoh6	1981	127	5.5	0.9	1.176	1.178	53.27	TrT
Itoh7	1981	169	6.5	1.32	1.214	1.241	47.39	LTrT
Marten11	1982	37	15.98	0.66	1.041	1.041	8.38	LTrT
Marten12	1982	37	15.98	0.66	1.041	1.041	12.6	LTrT
Marten13	1982	37	15.98	0.66	1.041	1.041	17.01	LTrT
Marten21	1982	37	15.51	1.12	1.072	1.072	8.34	LTrT
Marten22	1982	37	15.51	1.12	1.072	1.072	12.54	LTrT
Marten23	1982	37	15.51	1.12	1.072	1.072	16.68	LTrT
Marten31	1982	37	15.11	1.53	1.101	1.101	8.31	LTrT
Marten32	1982	37	15.11	1.53	1.101	1.101	12.31	LTrT
Marten33	1982	37	15.11	1.53	1.101	1.101	16.61	LTrT
Cheng	1984	37	15.04	2.26	1.154	1.164	13.4	LTrT
Efthimiadis	1984	19	18.92	4.6	1.248	1.248	35.2	L
Kunsch	1984	127	7.59	1.195	1.157	1.167	21.05	TrT
Marten41	1987	37	16.21	0.35	1.022	1.038	8.3	LTrT
Marten42	1987	37	16.21	0.35	1.022	1.038	12.5	LTrT
Marten43	1987	37	16.21	0.35	1.022	1.038	16.7	LTrT
Marten51	1987	37	15.87	0.65	1.041	1.056	8.3	LTrT
Marten52	1987	37	15.87	0.65	1.041	1.056	12.5	LTrT
Marten53	1987	37	15.87	0.65	1.041	1.056	16.7	LTrT

Table 2.1 continued from previous page

ID	Year	N_r	D (mm)	D_w (mm)	P/D	W/D	H/D	Group
Marten61	1987	37	15.35	1.1	1.072	1.087	8.3	LTrT
Marten62	1987	37	15.35	1.1	1.072	1.087	12.5	LTrT
Marten63	1987	37	15.35	1.1	1.072	1.087	16.7	LTrT
Marten71	1987	37	14.87	1.5	1.101	1.12	8.3	LTrT
Marten72	1987	37	14.87	1.5	1.101	1.12	12.5	LTrT
Marten73	1987	37	14.87	1.5	1.101	1.12	16.7	LTrT
Sahu1	1997	19	6.6	1.65	1.255	1.255	22.727	T
Sahu2	1997	19	6.6	1.65	1.255	1.255	30.303	T
Sahu3	1997	19	6.6	1.65	1.255	1.255	37.879	T
Chun1	2001	19	8	2	1.256	1.265	25	LTrT
Chun2	2001	19	8	2	1.255	1.268	37.5	LTrT
Chun3	2001	19	8	1.4	1.18	1.176	25	LTrT
Chun4	2001	19	8	1.4	1.178	1.18	37.5	LTrT
Choi	2003	271	7.4	1.4	1.2	1.2	24.84	TrT
Berthoux	2010	19	16	3.84	1.24	1.24	21.88	TrT
Kennedy	2015	127	6.55	1.8	1.282	1.279	40.458	TrT
Chang1	2016	37	8	1	1.131	1.133	27.69	TrT
Chang2	2017	61	8	1	1.14	1.14	29.86	T
Ohshima1	2017	127	5.5	0.9	1.176	1.178	38	LTrT
Ohshima2	2017	169	6.5	1.32	1.211	1.206	47.231	LTrT
Ohshima3	2017	271	7.5	1.4	1.2	1.2	22	TrT
Padmakumar	2017	217	6.6	1.65	1.255	1.27	30.3	LTrT
Pacio	2018	19	8.2	2.2	1.279	1.29	40	TrT
Vaghetto	2018	61	15.9	3	1.189	1.231	30	LTrT
Fan	2020	19	12.903	1.953	1.151	1.204	11.16	TrT

Table 2.1 continued from previous page

ID	Year	N_r	D (mm)	D_w (mm)	P/D	W/D	H/D	Group
Jeong	2020	19	9.58	1.59	1.315	1.315	27.3	Tr
Liang	2020	37	10	0.9	1.09	1.14	9.55	TrT
Song	2020	19	20	3	1.2	1.2	23.1	T
Li	2020	37	7	1.5	1.229	1.237	21.429	LTr

The flow split data is composed of two separate sets of experiments: the 8-bundle dataset of flow split in the edge subchannel also used in the UCTD development and the experiment from Xi'an Jiaotong University published by Liang et al. [2]. The latter is the only experimental work known by the author to have flow split data for the interior, edge, and corner subchannels.

2.2.2 Multi-Objective Genetic Algorithm Optimization

The coefficients of the original UCTD correlation were recalibrated using Multi-Objective Genetic Algorithms (MOGA). The genetic algorithms (GA) are a subset of the evolutionary algorithms (EA), heuristic methods for optimisation based on the concept of natural selection. In GA, the individuals or phenotypes, are a set of parameters that constitute a solution for a optimization problem. In the context of this work, an individual is the set of empirical coefficients of the UCTD formulation.

In GA, the fitness of the individuals of a population is calculated, for example through a error function. The best individuals are selected and merged to create off-springs, or a new set of solutions based on the selected individuals. The addition of a mutation step promotes diversity in the new population, expanding the search space of the method. Then the process repeats itself with the new population until a termination criteria is met. Figure 2.2 shows the basic schematics of GA.

2.2.2.1   Fitness

The fitness function of the bundle average friction factor is defined as the mean squared error between the mean C_{fb} of each experiment in the dataset of experiments and the prediction ($\widehat{C_{fb}}$) as
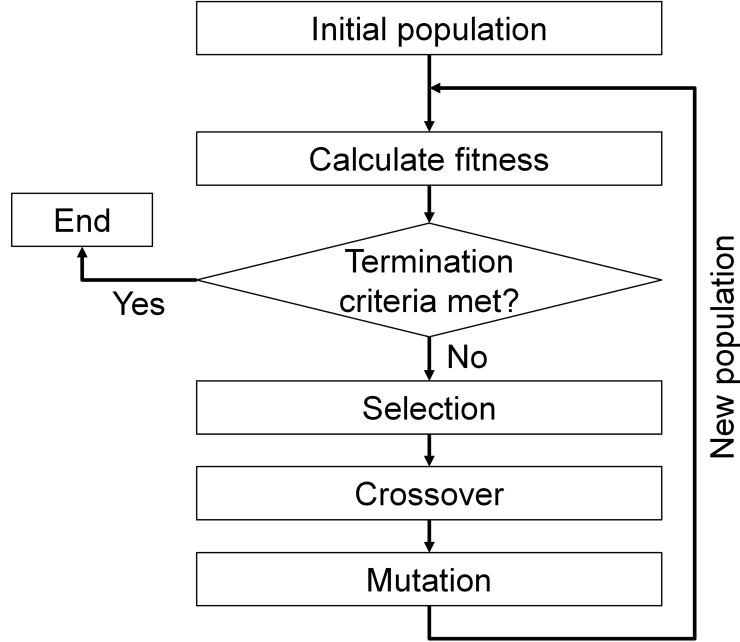
Figure 2.2: Steps of a Genetic Algorithm.

presented in 2.21. The fitness function of the flow split is calculated by summing the mean squared error of the XJU bundle flow split ($X_{xju,i}$) predictions and the mean squared error in the 8-bundle X_2 predictions as presented in 2.22.

$$error(C_{fb}) = \frac{1}{n} \sum_{j=1}^{n} \left(C_{fb,j} - \widehat{C_{fb,j}} \right)^2 \tag{2.21}$$

$$error(X) = \frac{1}{m} \sum_{j=1}^{m} \left(X_{2,j} - \widehat{X_{2,j}} \right)^2 + \frac{1}{3} \sum_{i=1}^{3} \left(X_{i,xju} - \widehat{X_{i,xju}} \right)^2 \tag{2.22}$$

2.2.2.2 Selection

Since the optimization process has two objectives, there is a trade-off between the accuracies of the average friction factor and flow split. The Pareto front is the set of individuals where no better solution for one objective is found without deteriorating the accuracy for the other objective. It is desirable from the selection method to keep the population well distributed along the Pareto front, so a solution with the most desirable balance between the objectives can be selected. The

16

Non-dominated Sorting Genetic Algorithm III (NSGA-III) [1] was selected as the sorting function. When selecting the most fit individuals, this method considers, in addition to the fitness function, the relative position of the new individual in the optimized front, as exemplified in Figure 2.3 from the NSGA-III publication. In this instance, a population is initialized in a reference plane (left) for three objectives. When selecting the new individuals (right), the method selects a better solution that is still close to the reference line from the parent solution. This approach is type of niche preservation. This study adopted an initial population of 200 solutions.
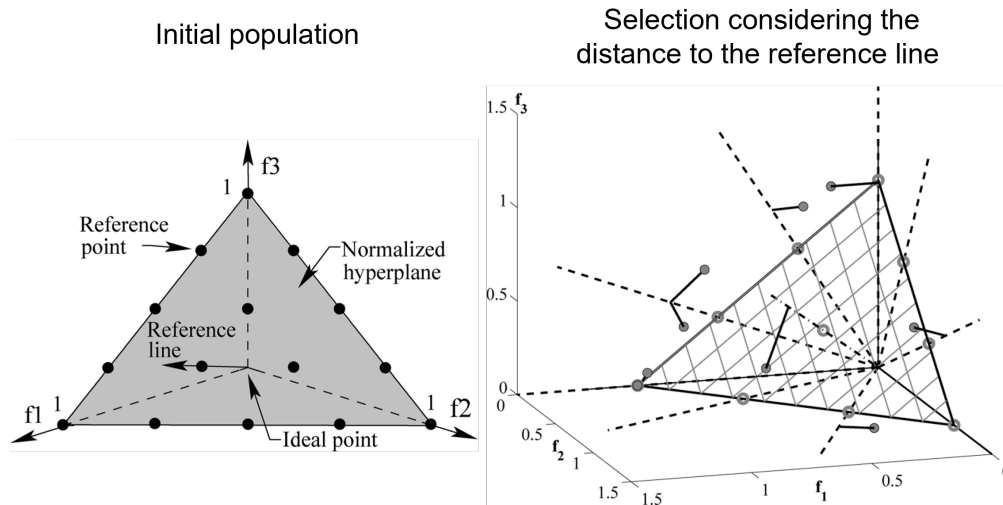
Figure 2.3: Niche preservation in the NSGA-III method. A population is initiated in a reference plane (left), then the new individuals are selected keeping the reference lines populated (righ). Adapted from Deb and Himanshu [1].

Fig. 2.4 shows the obtained solutions for the turbulent regime with the Pareto's front. The solution is selected from the Pareto's front elbow as a good balance between the objectives. The solutions to the right of the elbow have a steep worsening of the C_{fbT} fitness without a significant gain for flow split. Conversely, solutions to the left of the elbow do not provide a significant improvement in the C_{fbT} fitness to justify the loss in the flow split accuracy.

17
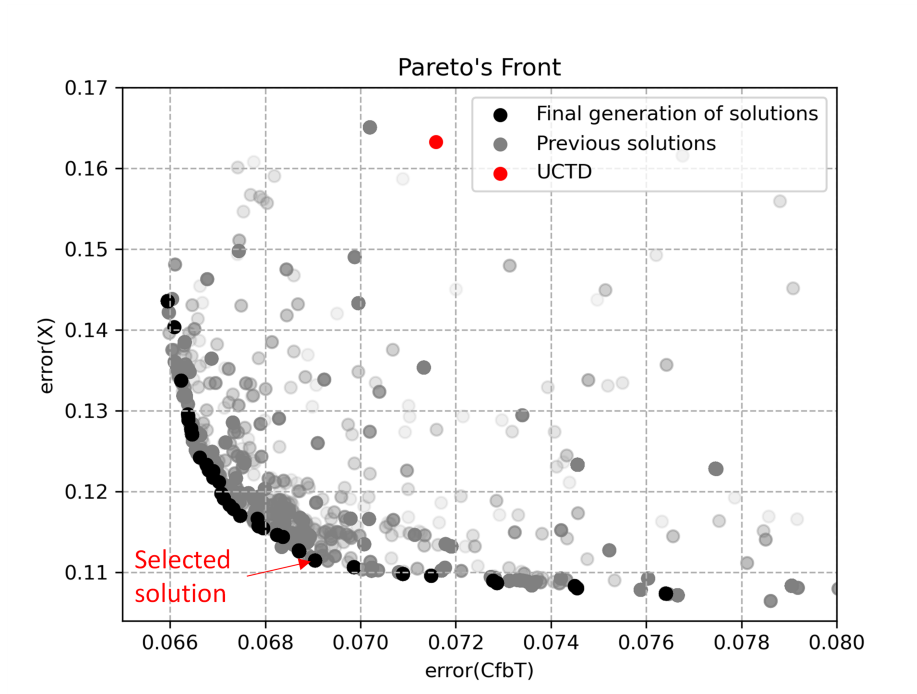
Figure 2.4: Pareto's front of the solutions for the fully turbulent flow regime.
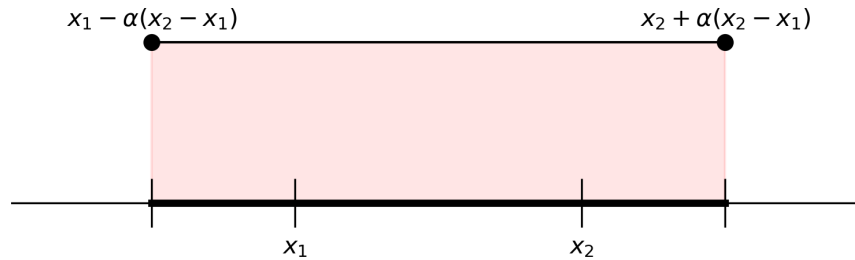
Figure 2.5: Interval where an offspring can be drawn from parents x_1 and x_2.

2.2.2.3 *Crossover and mutation*

This study used blend crossover for the generation of off-springs. For parents x_1 and x_2, where $x_1 < x_2$, off-springs are drawn randomly from the interval $[x_1 - \alpha(x_2 - x_1), x_2 - \alpha(x_2 - x_1)]$, illustrated in Figure 2.5. the parameter α defines the extrapolation limit from the parents, and it is set to 0.5 in this work. The offsprings undergo mutation by a factor following a Gaussian distribution defined with a mean of zero and unitary standard deviation.

18

2.2.2.4 Termination and convergence

The optimization process is terminated after 50 generations. Figure 2.6 shows the convergence of the fitness functions. Both fitness functions converge around the twentieth generation. The convergence of the best solution obtained with the MOGA method is better represented by the individuals with the best average between $Fitness(C_{fbT})$ and $Fitness(X)$, which ultimately leads to the selected solution. Under these criteria, convergence is also obtained after 20 generations.
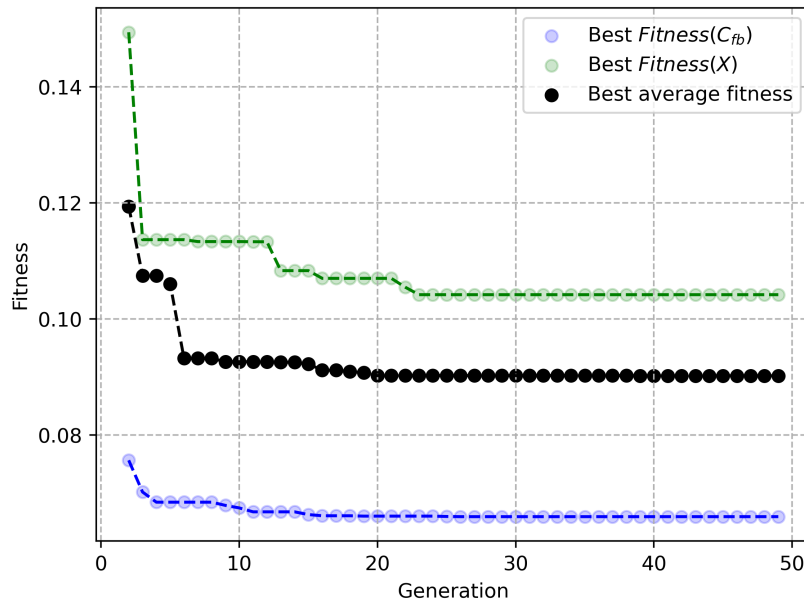
Figure 2.6: Solution convergence over the generations.

2.2.2.5 Constraints

A constraint function was added to penalize solutions that predict C_{fb} that decreases as the number of pins increases for geometries with the same pitch to diameter ratio (P/D). The experimental data support that the interior subchannels have higher friction losses. Thus, as the number of pins increases, the friction factor has to increase for the same P/D. However, if the optimization

is unconstrained, the solutions with the minimal loss allow for an inversion in this trend, especially for bundles with a high ratio of wire lead length to rod diameter (H/D). The penalty function is a summation of the square of the number of inverted points in the Rehme bundles [11], which are the ones in which this direct comparison is possible.

Figure 2.7 shows the inversion occurring in the predictions of Rehme bundles in an unconstrained model. Figures 2.8 to 2.12 show the pin number effect for the MOGA model with the constraint and compare the results with UCTD and the experimental data. The inversion is completely avoided. However, the optimization process has the tendency to minimize the differences in C_{fbt} between the bundles to the limit in $H/D = 50$, stressing the tendency of inversion.
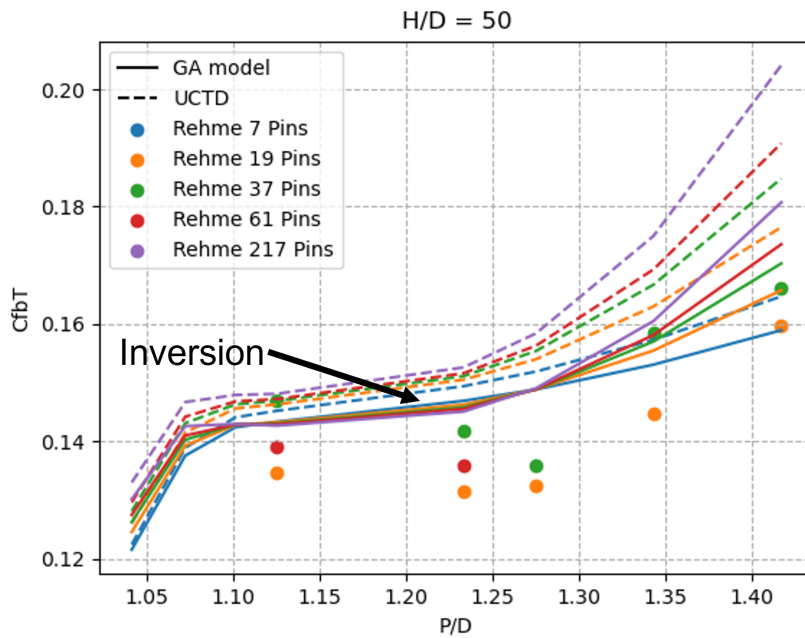
Figure 2.7: Pin number effect for $H/D = 50$ in the Rehme data using an unconstrained MOGA model.
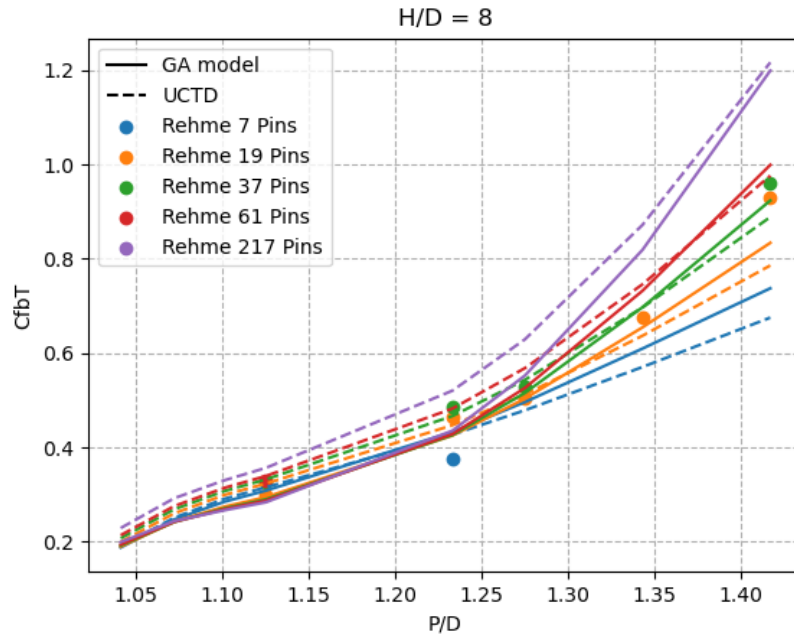
Figure 2.8: Pin number effect for $H/D = 8$ in the MOGA model compared to UCTD.
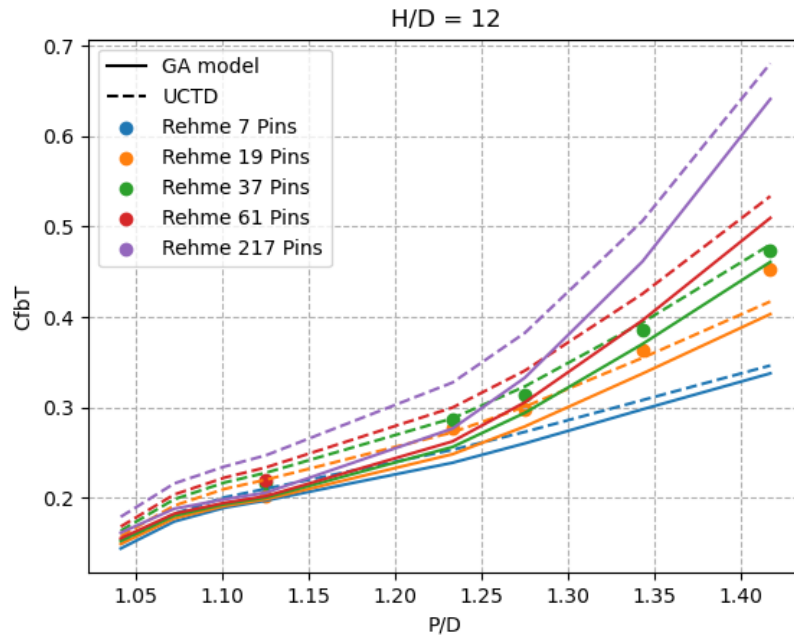
Figure 2.9: Pin number effect for $H/D = 12$ in the MOGA model compared to UCTD.
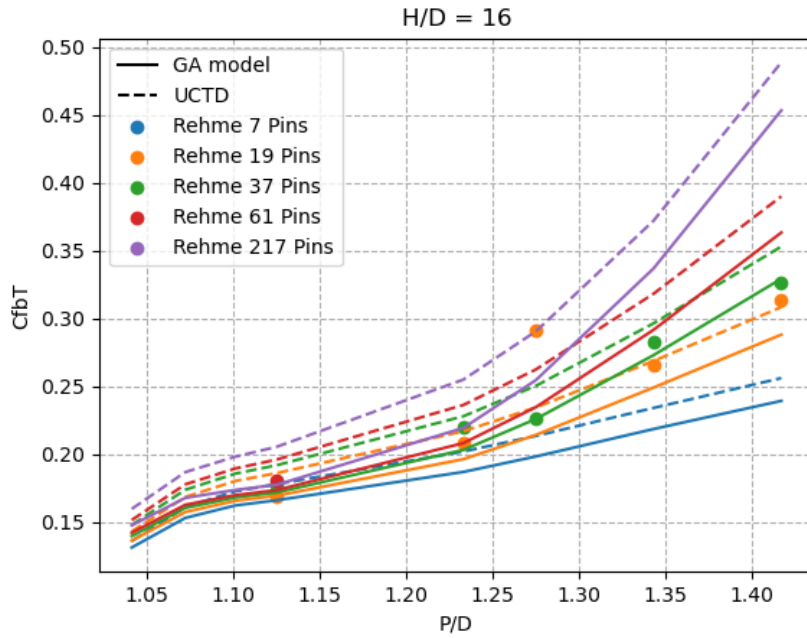
Figure 2.10: Pin number effect for $H/D = 16$ in the MOGA model compared to UCTD.
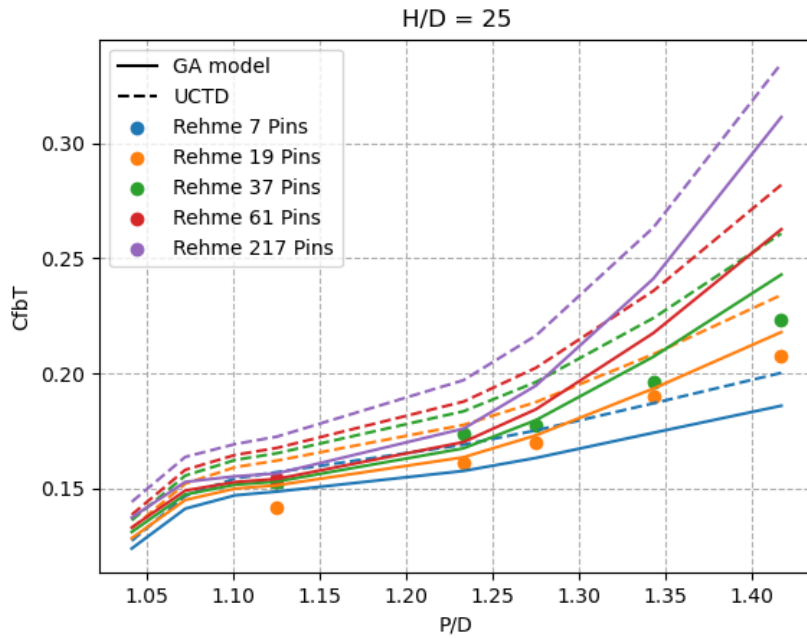
Figure 2.11: Pin number effect for $H/D = 25$ in the MOGA model compared to UCTD.
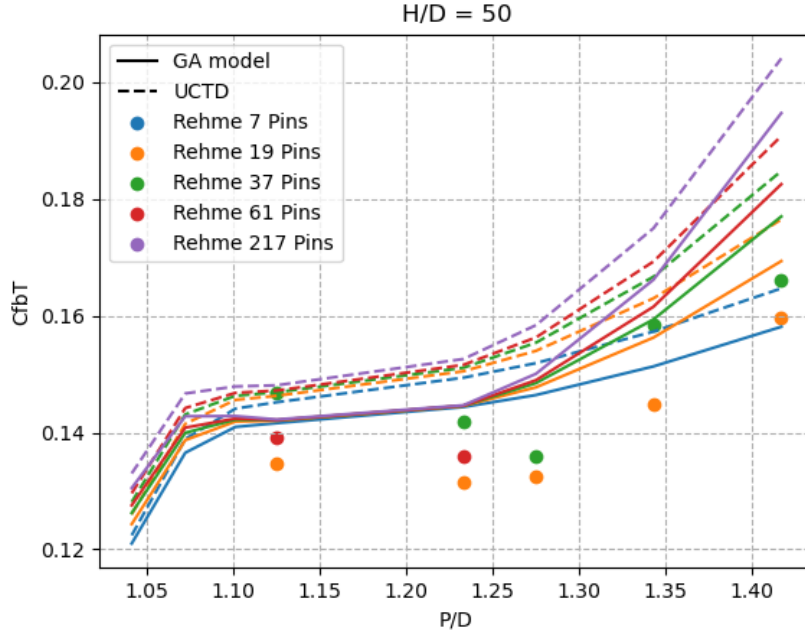
Figure 2.12: Pin number effect for $H/D = 50$ in the MOGA model compared to UCTD.

2.3 Results

Considering that W_{dL} and W_{sL} are functions of W_{dL} and W_{sL} respectively, the optimization process is performed in the turbulent region first. After all the coefficients for W_{dL} and W_{sL} are calculated, the coefficients for the laminar region, C_d and C_s, are optimized with data in the laminar and transition regimes.

2.3.1 Average bundle friction factor in the fully turbulent regime

Table 2.2 presents the original coefficients of the UCTD correlation and the ones obtained with the MOGA optimization in the turbulent region.

The correlation with the new values performs almost in the same way as the original UCTD for C_{fbT} predictions. Fig. 2.13 shows the comparison of the predicted and the experimental friction factors for the same dataset using UCTD and the new model, respectively.

Table 2.2: Original coefficients of UCTD the ones obtained with the MOGA optimization for the turbulent regime.

	C_1	C_2	C_3	C_4	a	b
UCTD	19.56	-98.71	303.47	-0.541	-11	19
MOGA	13.36	-81.38	285.78	-0.555	-19.12	28.40
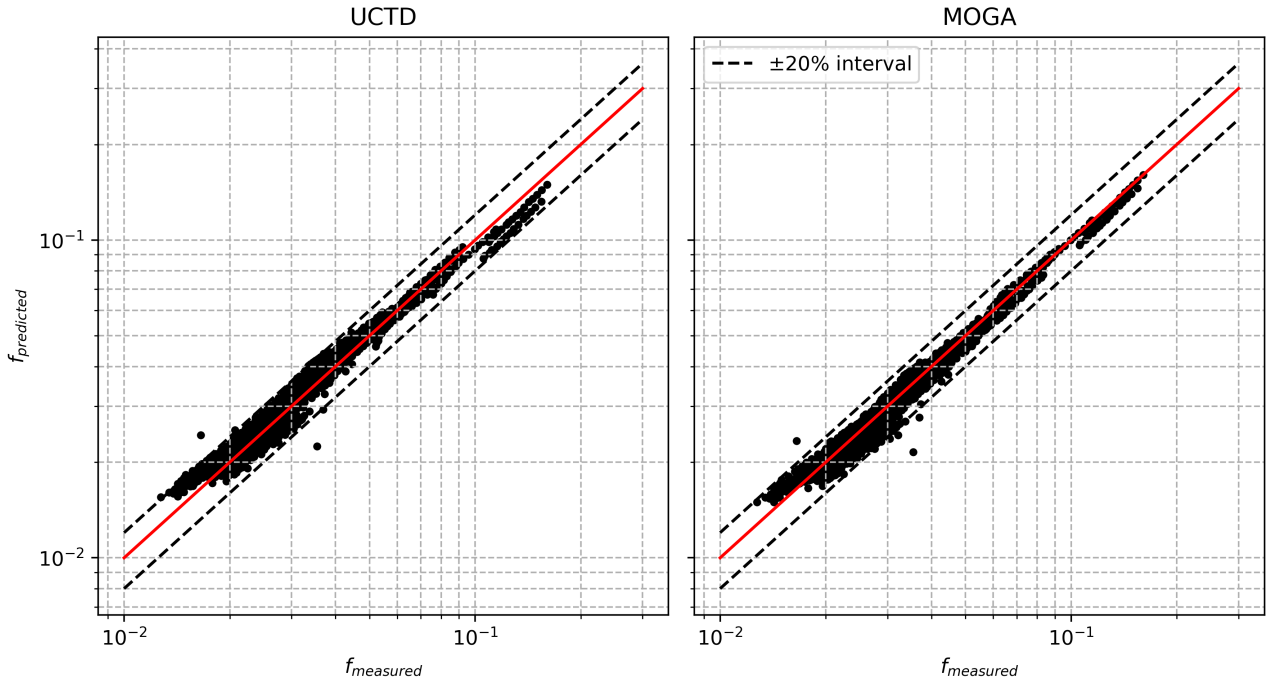
Figure 2.13: Comparisons between the experimental data for friction factor and the predictions for UCTD (left) and the MOGA recalibrated model (right).

Table 2.3 presents a summary of how well both models predict the dataset. The mean error of the bundle average friction factor was virtually unchanged, but the standard deviation of the error (STD) is higher for the MOGA optimized model. The distribution interval ($D.I.$) of 90% is defined as the amplitude of the error distribution between the 5th and 95th percentiles. The new model improved this parameter. In general, the indices of goodness suggest some marginal improvement for f_b. Since the primary purpose of this work is to improve the predictions of the flow split, keeping the accuracy in the f_b predictions is an acceptable outcome.

Table 2.3: Indices of goodness of the predictions from the original UCTD and the model with new coefficients for the turbulent regime.

	Mean error (f_b)	STD (f_b)	90% $D.I$ (f_b)
UCTD	6.64 %	8.80 %	±12.5 %
MOGA	6.23 %	11.9 %	±10.5 %

2.3.2 Flow split prediction in the turbulent regime

The accuracy of the flow split prediction, however, was substantially improved. Fig. 2.14 shows a comparison between the predictions from the MOGA recalibrated correlation and UCTD for the flow split experimental data from XJU. The predictions of the flow split parameters for interior and edge were significantly improved for the fully turbulent regime. The loss of accuracy for the corner subchannel occurred because both C_{f2T} and C_{f3T} are functions of W_{sT}; thus, it is not possible to improve one without worsening the other. However, the total flow area of the edge subchannels is much larger than the one of the corner.

Some overfitting on the XJU data may be expected since it composes a term of the flow split loss function; thus, the accuracy for this specific experiment does not provide a definitive reference of the model. Although a cross-validation evaluation is unfeasible due to the limited dataset, the model's performance in the 8-bundle X_2 dataset provides a good insight into the MOGA model generalization. Fig. 2.15 shows the improvement obtained with the MOGA model for X_2 at the highest Reynolds number available in each experiment. The updated model reduces the mean prediction error for X_2 from 9.3 % to 6.8 %.

2.3.3 Bundle average friction factor in the laminar and transition regimes

Table 2.4 presents the coefficients obtained with the MOGA method for the laminar flow. While the recalculated coefficients for the turbulent regime remained in the same range as the original ones, C_d and C_s obtained with the MOGA optimization are an order of magnitude different. This
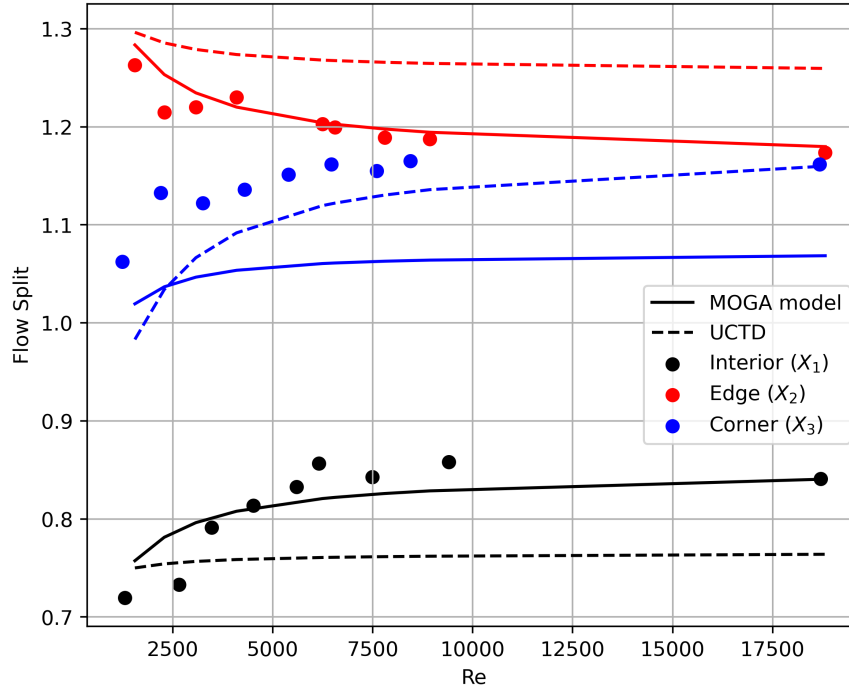
Figure 2.14: Comparison between the experimental data of flow split from XJU [2] and the predictions by UCTD and the recalibrated model.

discrepancy might raise the possibility that the solutions are not physically feasible.

Table 2.4: Original coefficients of UCTD the ones obtained with the MOGA optimization for the laminar regime.

	C_d	C_s
UCTD	1.4	1
MOGA	23.0	0.401

However, the new coefficients did not significantly change the average friction factor prediction. Fig. 2.16 shows a comparison between the experimental and the predicted average friction factors for the original UCTD correlation and the recalibrated model.

26
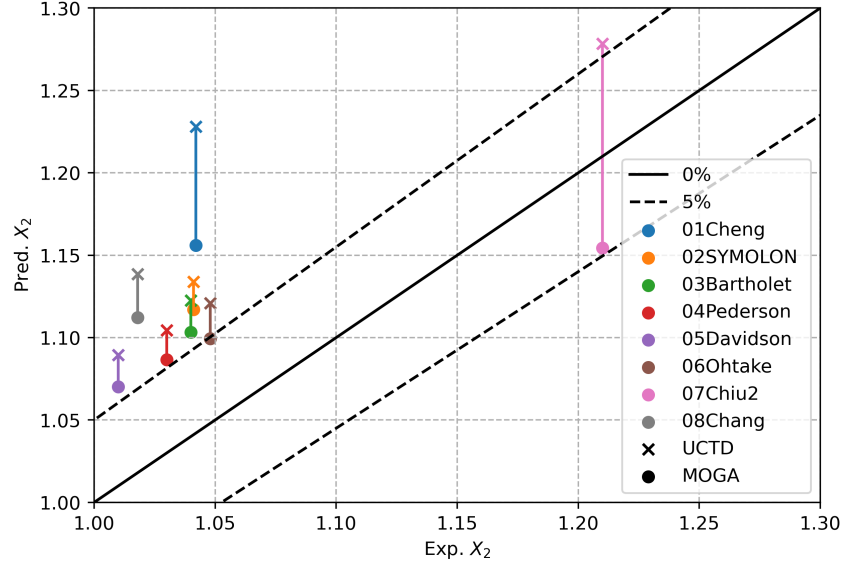
Figure 2.15: Comparison between the experimental data and the predictions of the flow split parameter in the edge region (X_2) by UCTD and the recalibrated model.

Table 2.5: Indices of goodness of the predictions from the original UCTD and the model with new coefficients for the laminar regime.

	Mean error (f_b)	STD (f_b)	90% $D.I$ (f_b)
UCTD	13.4 %	19.5 %	±26.0 %
MOGA	12.8 %	20.0 %	±26.0 %

Table 2.6: Indices of goodness of the predictions from the original UCTD and the model with new coefficients for the transition regime.

	Mean error (f_b)	STD (f_b)	90% $D.I$ (f_b)
UCTD	9.08 %	15.6 %	±21.6 %
MOGA	9.88 %	18.8 %	±21.1 %
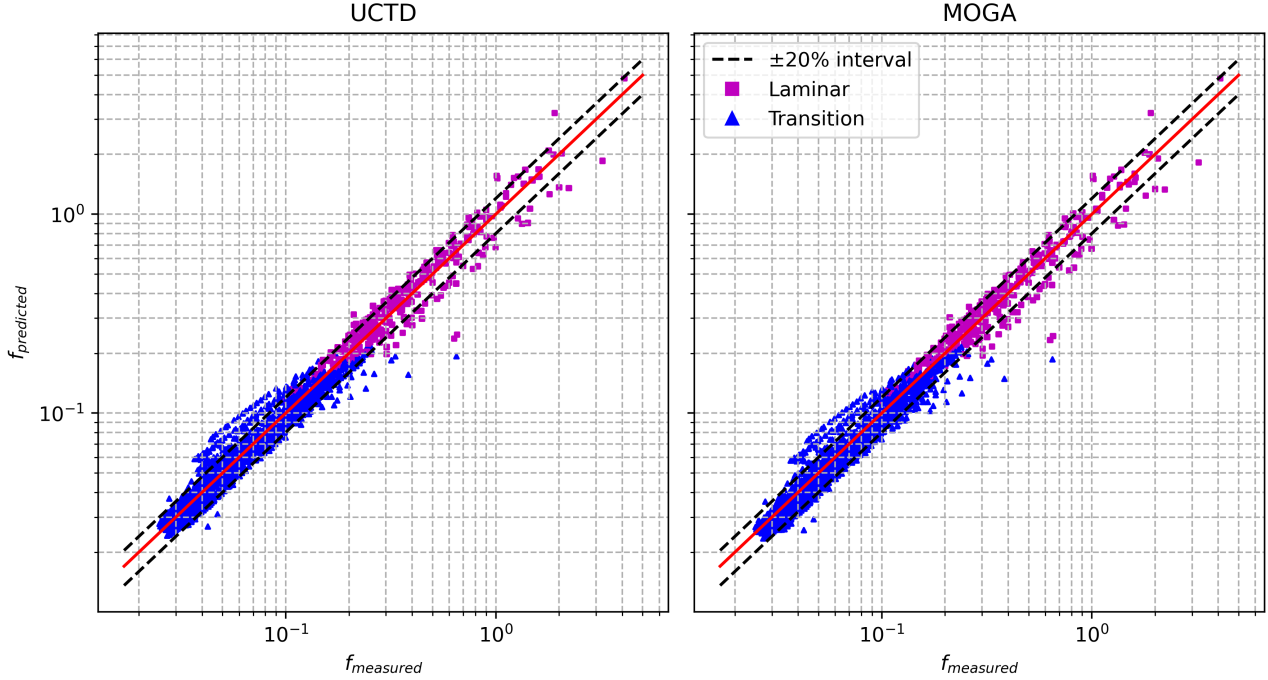
Figure 2.16: Comparison between the experimental data for friction factor and the predictions of the laminar and transition regimes.

Fig. 2.17 shows the loss domain for coefficients in the range of $0 \leq C_d \leq 100$ and $0 \leq C_s \leq 1$. The value of C_d is represented by the point color, increasing from the left to the right side. The tick color represents the value of C_s, increasing from the bottom to the top. The Pareto front is not well defined as for the case of the turbulent region (Fig. 2.4). The folded curve means that solutions with distinct coefficients wielding the same losses are obtained.

Moreover, one can observe that the lowest flow split loss is achieved with C_s equal to 0 or even negative, with the physical meaning of and friction factor in the edge and corner subchannels equal or smaller than the one of the bare bundle, which is nonphysical. This deficiency stems from the small dataset, limiting the degree of complexity the UCTD formulation could have or introducing overfitting to the optimization process. These results point to an ill-defined problem from the point of view of optimization.
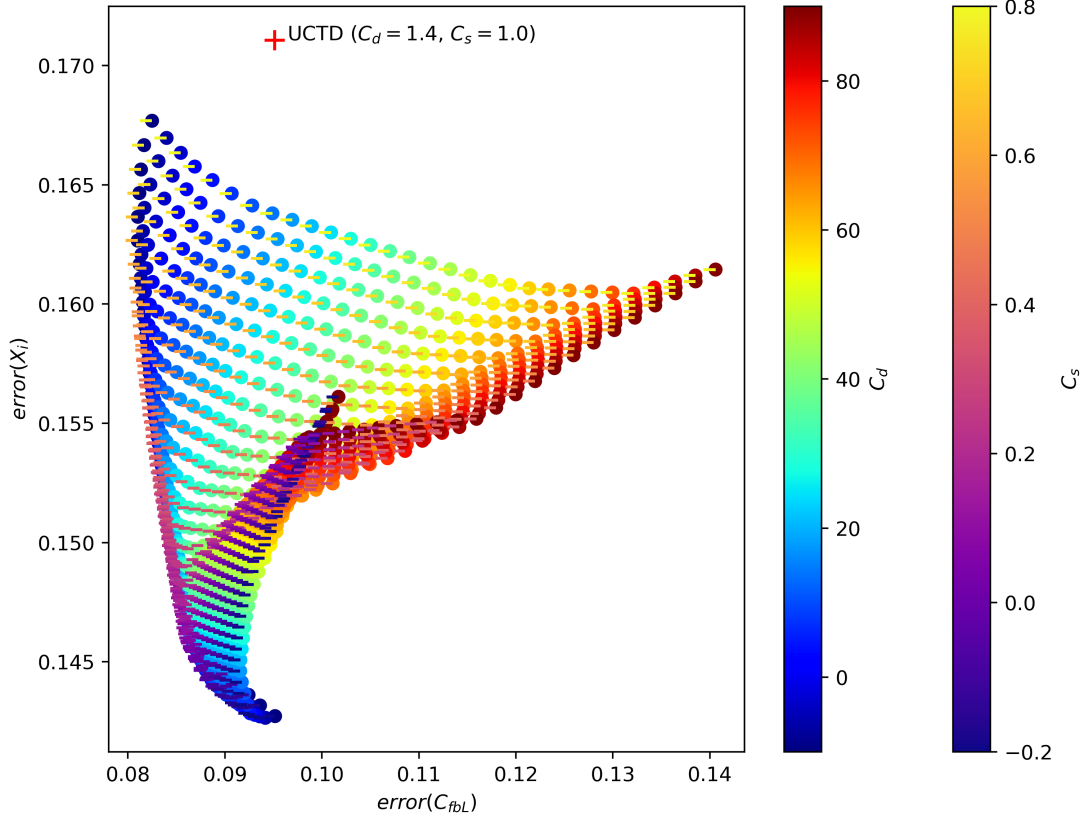
Figure 2.17: Loss domain curve for the optimization in the laminar and transition regions.

2.4 Conclusions

This work presented updated coefficients for the UCTD correlation for friction factor in wire-wrapped rod bundles obtained with Multi-Objective Genetic Algorithm optimization. After creating a set of non-dominated solutions by the Multi-objective Genetic Algorithm optimization, it was observed that UCTD already predicts the average friction factor well, but it is dominated for flow split. The recalibrated correlation reduced the average error of the flow split predictions in the turbulent region from 9.3% to 6.8% compared to the original UCTD for the 8-bundle dataset of flow split parameter in the edge region while performing close in the average friction factor. When observing the predictions for the XJU experiment, the only data that contains information for the interior, edge, and corner subchannels, a significant improvement was observed, although some level of overfitting may be present. The new coefficients for the laminar regime are far from

the original UCTD coefficients, implying that they may not be physical. However, the predictions are similar to the average friction factor, and the flow split was also improved compared to UCTD. The discrepancy in the coefficient values may indicate data starvation and the necessity to modify the equations for the laminar region. This limitation was mitigated with the creation of a complementary dataset using CFD simulations, presented in Chapter 3, allowing the creation of a high order model for the laminar regime using Artificial Neural Networks, as presented in Chapter 4.

3. SIMULATIONS

The Reynolds number adopted in the simulations has to be low enough to ensure that no transition to turbulent flow would occur in any geometry. Therefore, the database is composed of simulations performed with a Reynolds number that ensures the linear relationship between the friction factor and the inverse of the Reynolds number. Considering that the typical laminar boundary in literature occurs between $Re = 300$ and $Re = 1200$, a Reynolds number of $Re = 250$ was selected. While satisfying the condition of being lower than the observed critical Re in the experiments, this value is still close to the flow condition of most of the experiments in the validation database considered in this study.

Since the simulations are respective to flows known to be laminar and steady, no macroscopic fluctuations are expected. Therefore, there is no need to use CFD models intended to solve any timescale of the flow or to introduce any turbulent viscosity to model turbulence. The simulations are isothermal and incompressible, and both viscosity and density are constant.

3.1 Governing Equations

The Navier-Stokes (NS) equations are known for being challenging to solve analytically due to the nonlinear convective term. Therefore, the NS equations are discretized to be used in CFD codes.

$$\frac{\partial}{\partial t}\int_V \rho \, dV + \oint_A \rho \cdot \boldsymbol{v} \cdot d\boldsymbol{a} = \int_V S_u dV \tag{3.1}$$

$$\frac{\partial}{\partial t}\int_V \rho \boldsymbol{v} \, dV + \oint_A \rho \boldsymbol{v} \otimes \boldsymbol{v} \cdot d\boldsymbol{a} = -\oint_A p \boldsymbol{I} \cdot d\boldsymbol{a} + \oint_A \boldsymbol{T} \cdot d\boldsymbol{a} + \int_V \boldsymbol{f_b} dV + \int_V \boldsymbol{s_u} dV \tag{3.2}$$

31

$$\frac{\partial}{\partial t} \int_V \rho E dV + \oint_A \rho H \boldsymbol{v} d\boldsymbol{a} = - \oint_A \boldsymbol{q} \cdot d\boldsymbol{a} + \oint_A \boldsymbol{T} \cdot \boldsymbol{v} d\boldsymbol{a} + \int_V \boldsymbol{f_b} \cdot \boldsymbol{v} dV + \int_V \boldsymbol{S_u} dV \qquad (3.3)$$

The equations 3.1, 3.2 and 3.3 are extensively simplified due to the assumptions of the model. As the flow is steady, all the time derivatives are removed from the equations. Since the flow is incompressible, the constitutive equation is reduced to the integral over the control volume of the velocity vector. Moreover, without any microscopic fluctuation in the flow, these equations can be directly described in terms of the mean quantities without resorting to constitutive equations for the Reynolds stress tensor, which is zero for laminar flows. These characteristics deem numerical simulations of laminar flows considerably more robust than solutions for turbulent flows, particularly by avoiding turbulence modeling uncertainties. This characteristic makes CFD an attractive solution to the expansion of the available data of laminar flows in wire-wrapped rod bundles.

3.2 Domain Modeling

3.2.1 Boundary Conditions

Figure 3.1 shows the boundaries of the computational domain. The fluid makes contact with three solid bodies: the rods, the wires, and the hexagonal enclosure. All the walls are defined as no-slip boundaries, where $u = v = w = 0$. The computational domain encompasses the height of a full helical pitch of the wire around the base rod, so that the cross-sections of the inlet and outlet are equal. As a consequence, the inlet and outlet boundaries are defined as periodic. All the physical quantities of the outlet boundary, except pressure, are replicated in the inlet boundary. The solver computes the pressure field so that the mass flow rate will match a fixed given value. These boundary conditions define the flow in an infinite duct, therefore categorizing the flow in the computational model as fully developed.

Periodic Inlet and Outlet   No-Slip Walls
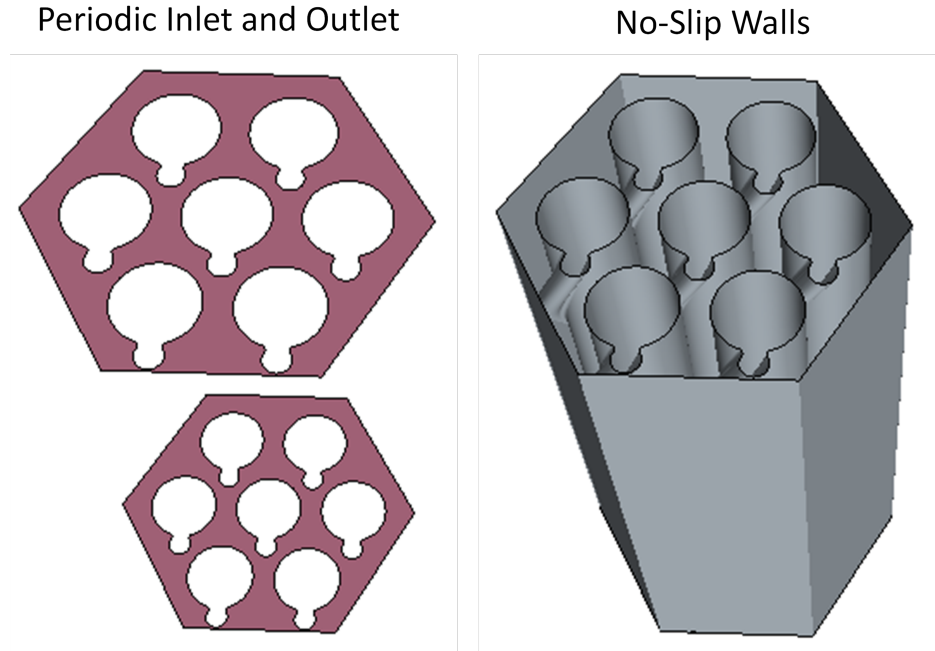
Figure 3.1: Boundary conditions are set as periodic for the inlet and outlet (left), and no-slip for all the solid surfaces (right).

3.2.2 Modeling of contact point

The simulated geometries refer to the standard geometry of a wire-wrapped rod bundle described in the previous sections. All the bundles simulated refer to tightly packed geometries, where there is no physical gap between the rods and wires and between the wires and the channel wall. However, the contact point between geometries with curved surfaces is known to create discretization problems. This issue arises because the contact tends to parallel planes with an infinitesimal gap in between. This geometry leads to strongly skewed mesh elements, which causes numerical instability. Several studies involving multiple bodies of curved shape faced this issue, notably packed bed of spheres [34, 35, 36]. In these studies, the strategies to handle the meshing of contact points often include reducing the body size, increasing the radius to create volume overlaps, capping the contact region, or bridging the bodies in the contact point.

The problem of meshing in the contact region is already known in the wire-wrapped rod bundle simulation field. Bieder et al. [37] investigate different wire geometries balancing the meshing

performance and accuracy at predicting hot spot temperatures. This study considered a wire displaced into the rod, smoothing the contact point and using a wire of squared geometry instead, concluding that the first strategy is the best one. Delchini et al. [38] evaluated the sensitivity of the pressure drop to the modeling of the contact between wire and rod. The authors proposed two models: a close-gap approach, in which the contact point between the wire and rod is enlarged, and an open-gap approach, in which the wire is recessed to create a gap in the contact location. The authors concluded that the open-gap approach better represents the flow. The works of Jeong et al. [39] and Bovati et al. [40] also resorted to the open-gap approach to simulate wire-wrapped rod bundles.

The open-gap strategy was selected based on the results obtained in the literature. The contact between the wire and its base rod is smoothed with fillets of a diameter of $D_w/3$. The wire is recessed into its base rod by 7.5% of the wire diameter. Figure 3.2 shows the actual geometry of a tightly packed wire-wrapped rod bundle, in which the pitch is equal to the sum of the rod and the wire diameters, and the geometry modeled for the CFD simulations.
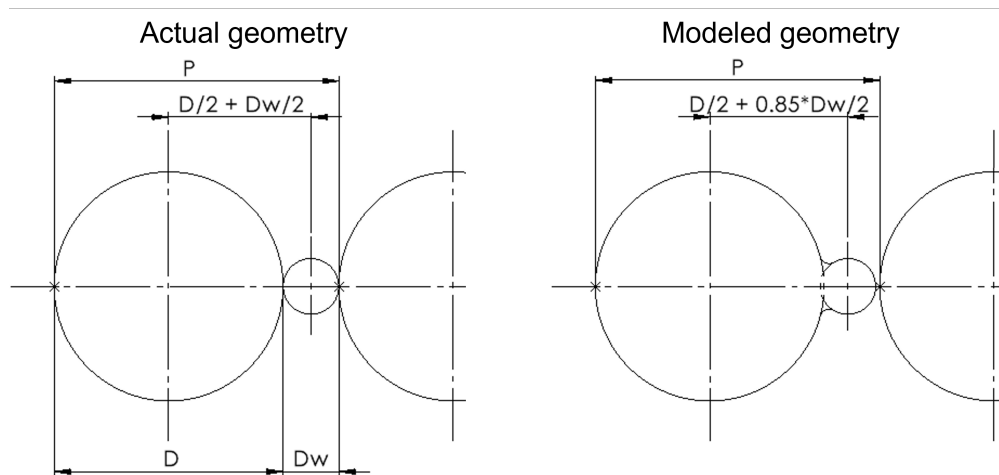
Figure 3.2: Actual geometry of a wire-wrapped rod bundle (left) and modeled geometry for the CFD simulations (right).

The modeled geometry has an objective to achieve a balance between accuracy compared to

the actual geometry and numerical performance. It is desirable to yield a mesh with a smooth transition between the contact point and the rest of the domain; simultaneously, the gap cannot be big enough to interfere with the flow. Figure 3.3 shows the contact region mesh, where the skewness of the elements is observed to be well controlled, as well as the growth rate from the contact to the rest of the domain. From the axial velocity contour, one can notice that the velocity in the gap between the wire and the next rod is negligible.
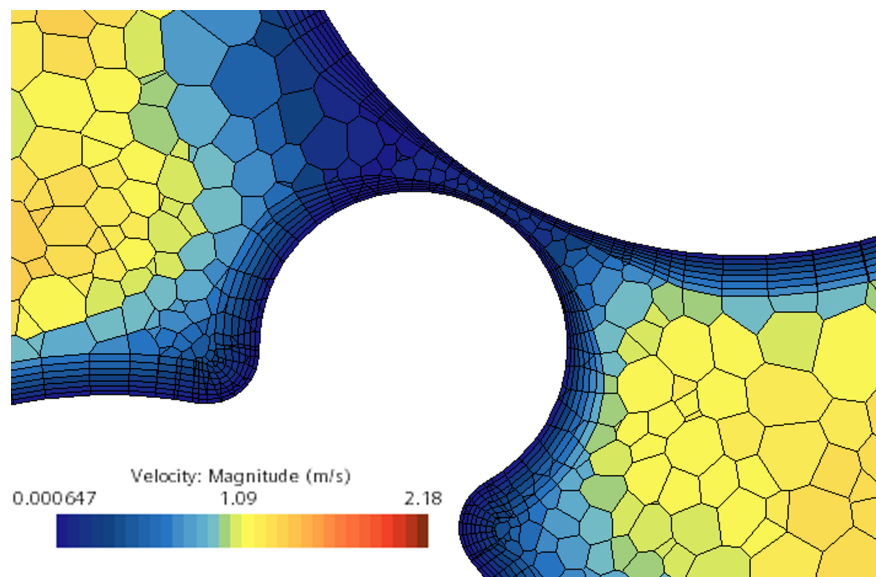
Figure 3.3: Mesh and contour of velocity magnitude for a bundle with P/D = 1.32 at an elevation in which the wire makes contact with the neighboring rod. The velocity magnitude at the contact is negligible.

3.2.3 Meshing

The literature contains works involving CFD simulations of wire-wrapped rod bundles with different types of meshes. The adopted meshing strategy reflects the available repository of CFD codes and the specific objectives of each study, the depth in which the study investigated the meshing process itself, and the available computational resources. Early works typically used tetrahedral mesh elements. In 2007, Gajapathy et al. [41] used tetrahedral elements with the code STAR-CD. Bieder et al. [37] also used tetrahedral meshes with the code Trio_U a work published in 2010.

Since more capable meshing codes became available, more recent works used hexahedral and polyhedral meshes. Zhao et al. [42], in 2017, used a hexahedral mesh with OpenFOAM to simulate turbulent flows at the range of P/D between 1.11 and 1.22. In the same year, Jeong et al. [39] developed a method to generate hexahedral meshes to be used with the code CFX, dividing the flow domain into outer fluid and inner fluid using a circular boundary line containing the rod and the wire. This strategy allowed the authors to obtain elements with a good shape and with a controlled refinement.

Podila and Rao [43] simulated in 2014 the Canadian SCWR using the code STAR-CCM+ for both the bare rod bundle and the wire-wrapped rod bundle. The authors used hexahedral meshes for the bare bundle. However, they opted for the polyhedral mesh to simulate the wire-wrapped bundles due to the flexibility of this type of mesh to model complex geometries. Delchini et al. [38] (2017) found the hexahedral mesh more accurate than polyhedral mesh when simulating a single pin geometry. However, they resorted to polyhedral when simulating a 7-pin bundle to save computational effort. Recently, Bovati et al. [40] simulated the 61-pin wire-wrapped rod bundle facility at Texas A&M University using Star-CCM+ and polyhedral meshes, reaching a good agreement with the experimental data.

The polyhedral meshing of STAR-CCM+ has demonstrated to generate reliable representations of complex geometries, including wire-wrapped rod bundles. In addition to that, this work involved the simulation of geometries in a vast range of P/D. The gap between the rods is the most critical feature to mesh, and the range of P/D is between 1.02 to 1.42. The gap width varies between 12% to 58% of the hydraulic diameter; thus, there is a dramatic change in the refinement requirements between the tested geometries. This characteristic makes the polyhedral meshing preferred to this work.

The same mesh parameters were used for all geometries for consistency between the simulations. The element base size is 10% of the hydraulic diameter. Seven prismatic layers are used to improve the wall shear stress quantification. The number of elements is roughly proportional to H/D and N_r due to the increase of the fluid domain size. The P/D, on the other hand, causes a

sharp increase in the number of elements as the requirement for more refinement the gap increases. Figure 3.4 show the meshes
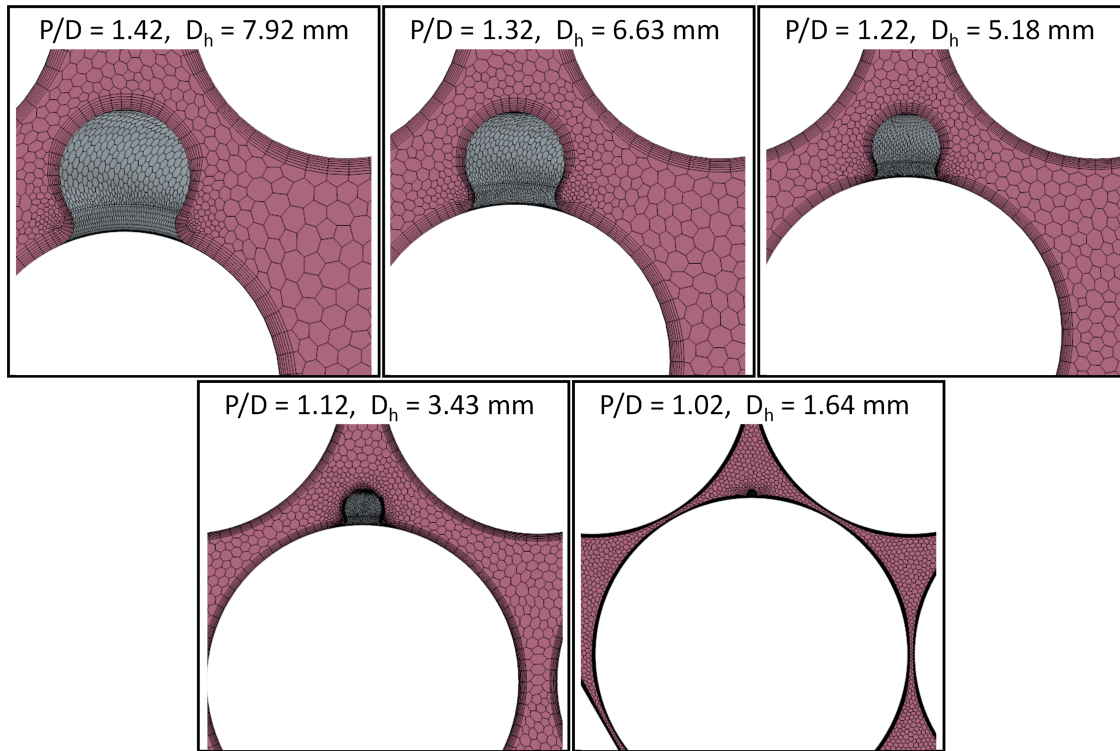
Figure 3.4: Meshes of 7-pin bundles at the P/D range of 1.42 to 1.02 with $H/D = 8$. The hydraulic diameter is also presented for each bundle.

Figure 3.5 shows how the number of elements in the meshes evolve as a function of P/D and H/D. The mesh refinement is not strongly affected by H/D since the wire pitch does not affect the flow cross-section significantly. The impact of H/D on the discretized domain is mainly limited to the height of the fluid domain. Thus, the relationship between H/D and the number of elements is almost linear. On the other hand, the computational cost of the simulations increases sharply as P/D decreases, especially for very low P/D. Besides the relationship mentioned above between P/D and D_h, the gap between the rods becomes very narrow, requiring substantial mesh refinement in this region to properly model the cross-flow between subchannels.
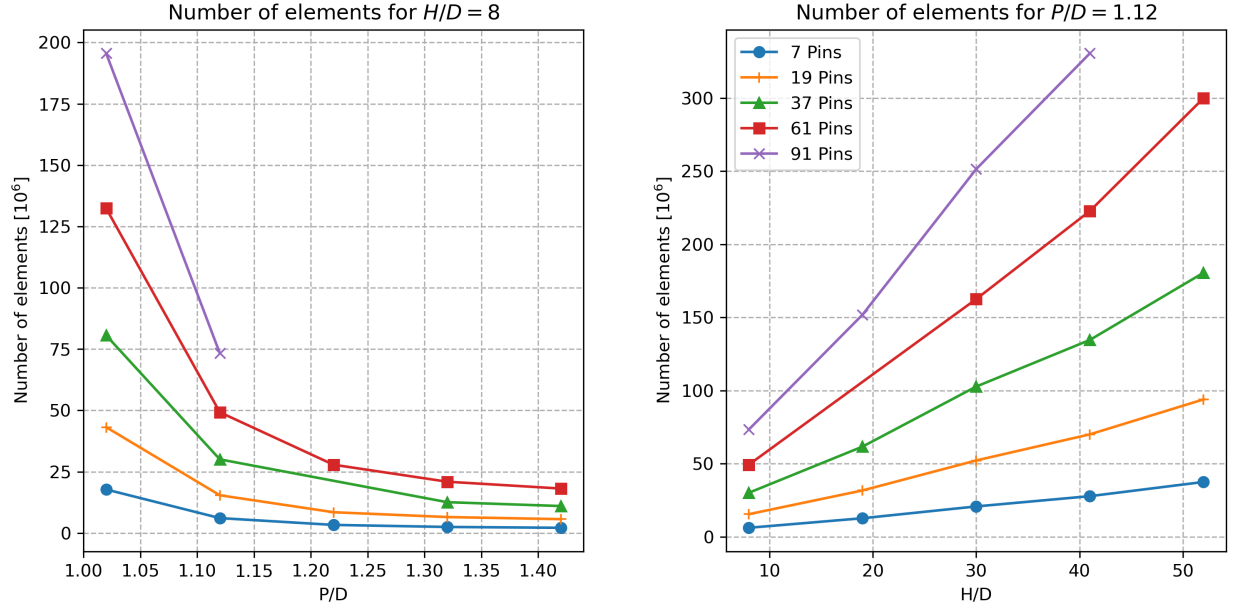
Figure 3.5: Number of elements in the meshes as a function of P/D (left) and as a function of H/D (right).

3.2.4 Post-processing

The pressure drop is the first quantity of interest obtained from the CFD simulations. The pressure field is not uniform across the flow area. Since the wires impel the fluid sideways, a lateral pressure gradient is established in the direction of inclination of the wire, as shown in Figure 3.7. Therefore, in order to compute the pressure of the bundle, the average pressure in the flow area for the inlet and outlet are calculated using Equation 3.4. A_j denotes for the area of the node j normal to y, and A is the flow area. Pressure drop is then calculated as the difference between the average pressures of the inlet and outlet as in Equation 3.5.

$$\bar{P} = \frac{1}{A} \int_i A_j * P_j \tag{3.4}$$

$$\Delta P = \bar{P}_{inlet} - \bar{P}_{outlet} \tag{3.5}$$

The relationship between the pressure drop (ΔP) and friction factor is calculated from the
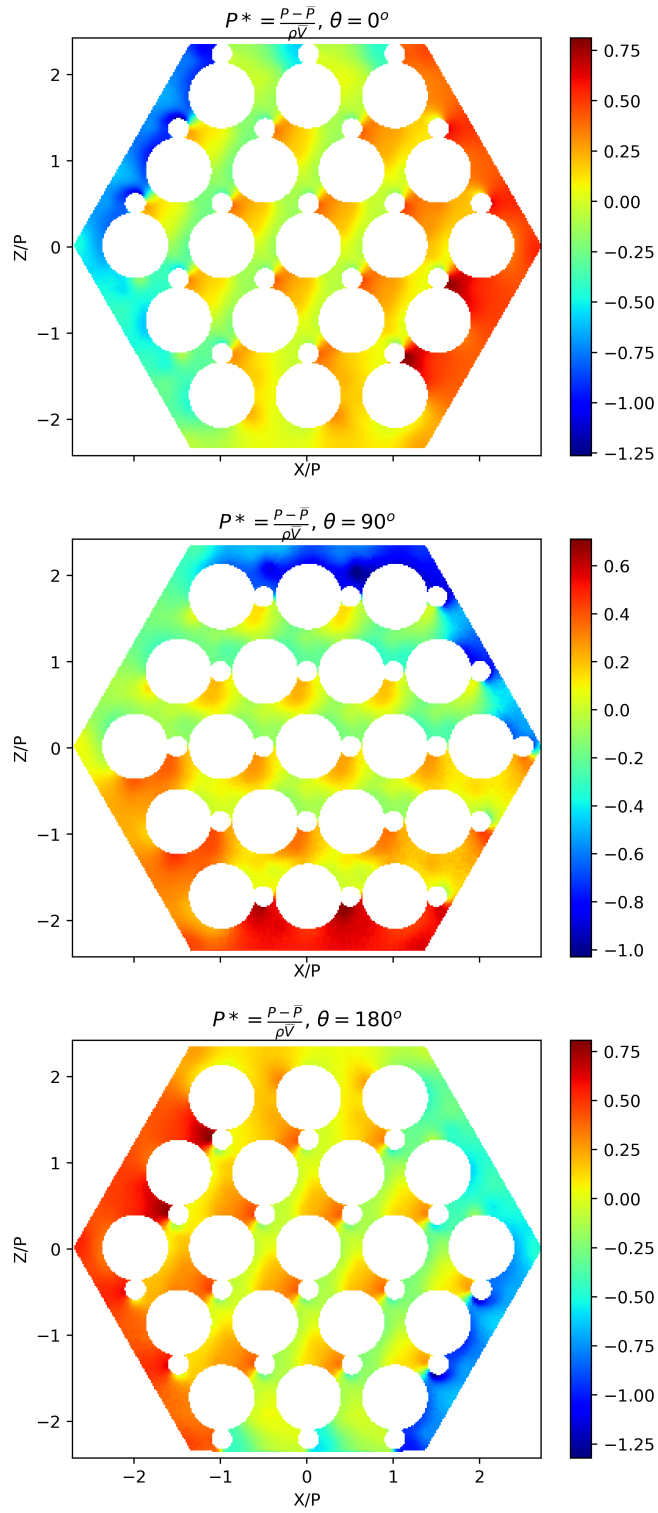
Figure 3.6: Normalized pressure gradients in the lateral direction for different elevations.
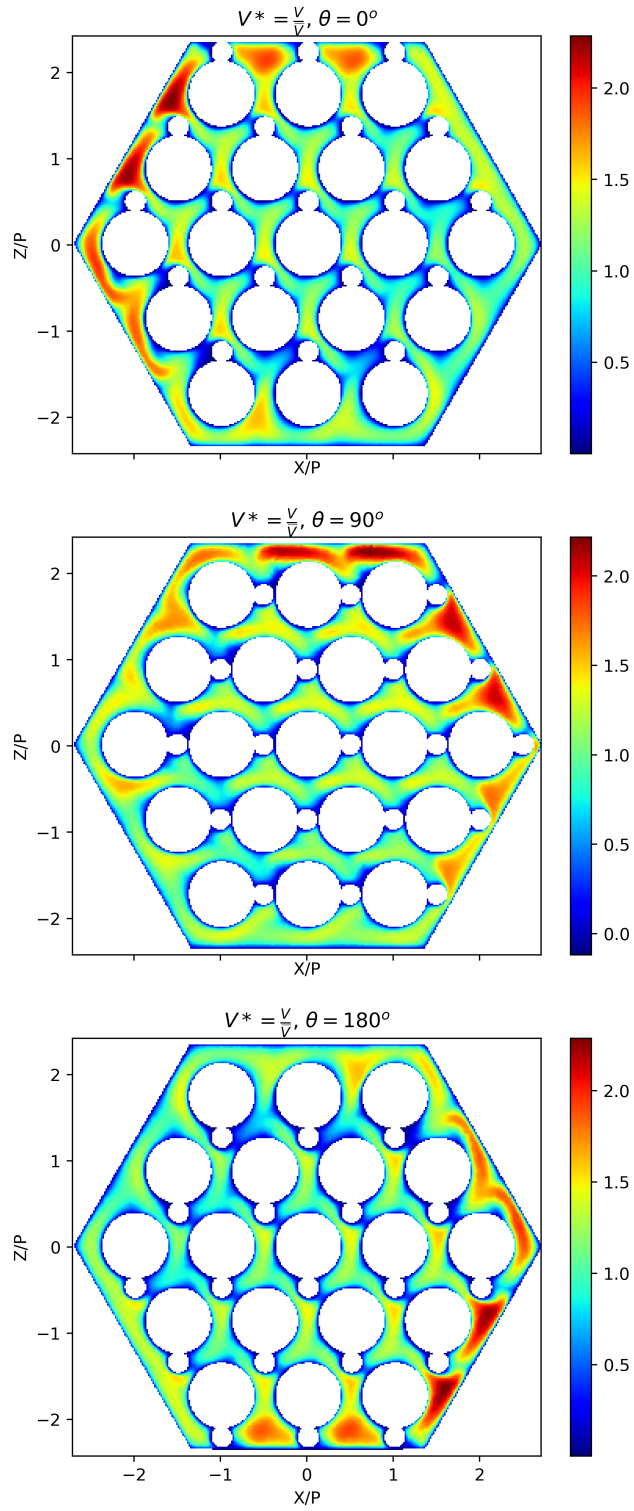
Figure 3.7: Contours of normalized axial velocity for different elevations.

Darcy-Weisbach equation shown in Equation 3.6, where H is the domain height, D_h is the hydraulic diameter, ρ is the density, and $\bar{V}$ the mean axial velocity of the flow.

$$\Delta P = f_b \frac{H}{D_h} \frac{\rho \bar{V}^2}{2} \tag{3.6}$$

As $\bar{V}$ and ρ are set to be unitary in the simulations, the friction factor of the simulated bundles is calculated as in Equation 3.7.

$$f_b = \frac{2D_h \Delta P}{H} \tag{3.7}$$

The second quantity of interest is the flow split between the regions. Figure 3.8 shows how the flow area is divided between the interior, edge, and corner regions. The flow split for a given elevation y is calculated as the ratio between the mean axial velocity in the region i (i = 1, 2, and 3 for interior, edge, and corner, respectively) and the bundle mean axial velocity. Since the flow area in the subchannels depends on the wire position, the flow split fluctuates over y. Therefore, this study considers as the flow split parameter the mean of the flow split over one wire pitch as in Equation 3.8.

$$X_i = \frac{1}{H} \int_H \bar{V}_i(y)/\bar{V}(y) dy \tag{3.8}$$

3.2.5 Evaluation of Grid Convergence and Spatial Discretization Uncertainty

Numerical simulations of flows involve the discretization of the space domain into a grid. As the grid is refined, the uncertainty of the spatial discretization tends asymptotically to zero. Thus, it is suitable for CFD analysis to verify how close to the ideal grid independence condition a simulation is and quantify the discretization uncertainty. Since this work involves the statistical representation of the behavior of the pressure drop as a function of different geometries, there is an acute sensitivity to grid uncertainties over the geometric parameters of interest; otherwise, the grid dependencies would be indistinguishably represented by the machine learning model.
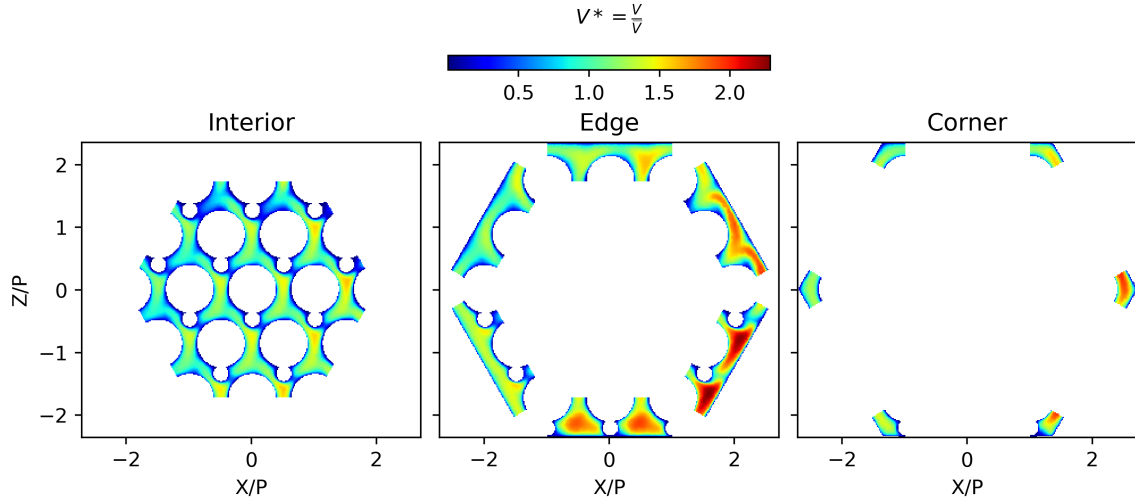
Figure 3.8: Axial velocity contours in the interior, edge and corner regions.

The grid convergence was investigated for the two limits of P/D since this is the most significant geometrical parameter to meshing. The evaluation of the discretization uncertainty used the Grid Convergence Index (GCI) method of Celik et al. [44]. This method requires three grids with successive refinements to quantify the discretization uncertainty of the finer grid. First, the parameter h is calculated for each mesh using Equation 3.9, where V is the domain volume, and N is the number of elements in the grid. The refinement ratio is defined by Equation 3.10.

$$h = \left[\frac{1}{N} \sum_{i=1}^{N} (\Delta V_i) \right]^{1/3} \tag{3.9}$$

$$r_{coarse,fine} = \frac{h_{coarse}}{h_{fine}} \tag{3.10}$$

Table 3.1 and 3.2 presents the mesh size information for the $P/D = 1.02$ and the $P/D = 1.42$ bundles respectively. The refinement ratio was aimed at $r = 1.3$. Figures 3.9 and 3.10 show how the pressure drop and the flow split parameters varied as a function of the mesh size for both bundles. Monotonic convergence occurs in all cases, with all variables presenting asymptotic

behavior.

Table 3.1: Mesh sizes and refinement ratio for $Nr = 7$, $H/D = 8$ and $P/D = 1.02$.

Mesh identifier	Number of nodes (N)	$h = (V/N)^{1/3}$	Refinement ratio based on h
1	17,788,208	0.000328	$r_{21} = 1.301$
2	8,086,959	0.000429	$r_{32} = 1.302$
3	3,665,273	0.000562	—

Table 3.2: Mesh sizes and refinement ratio for $Nr = 7$, $H/D = 8$ and $P/D = 1.42$.

Mesh identifier	Number of nodes (N)	$h = (V/N)^{1/3}$	Refinement ratio based on h
1	2,167,868	0.000328	$r_{21} = 1.308$
2	968,146	0.000429	$r_{32} = 1.311$
3	429,919	0.000562	—

Equation 3.11 computes the GCI value, where the indices 1 to 3 refer to the three meshes used in the method, from the finer to the coarser.

$$GCI^{21} = \frac{F_s \epsilon_{21}}{r_{21}^p - 1} \tag{3.11}$$
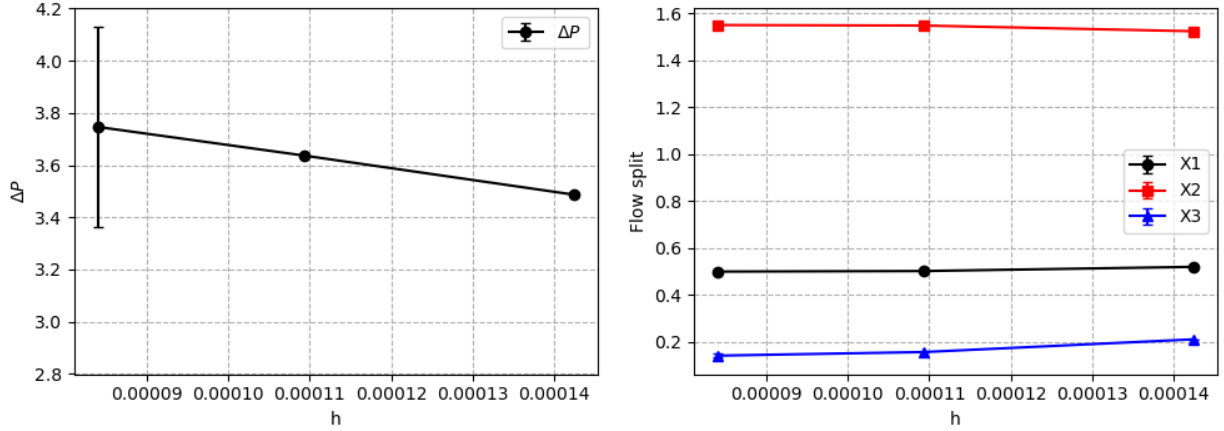
Figure 3.9: Pressure drop and flow split in a bundle with $Nr = 7$, $H/D = 8$ and $P/D = 1.02$ for subsequently refined meshes.
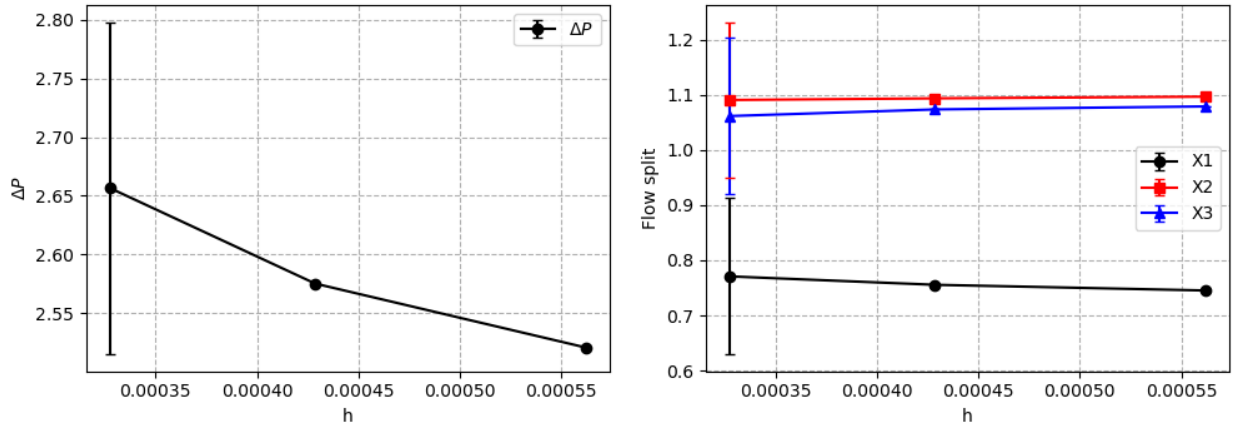
Figure 3.10: Pressure drop and flow split in a bundle with $Nr = 7$, $H/D = 8$ and $P/D = 1.42$ for subsequently refined meshes.

A safety factor of $F = 1.25$ is used when the method is used with three meshes. The apparent order of grid convergence p is calculated using the Equations 3.12, 3.13 and 3.14.

$$p = \frac{1}{ln(r_{21})} ln \left| \frac{\epsilon_{32}}{\epsilon_{21}} \right| + q(p) \tag{3.12}$$

$$q(p) = ln \frac{r_{21}^p - s}{r_{32}^p - s} \tag{3.13}$$

$$s = 1 \cdot sgn\left(\frac{\Phi_{32}}{\Phi_{21}}\right) \tag{3.14}$$

Table 3.3 summarizes the results obtained from the GCI simulations and their respective uncertainties.

Table 3.3: Results obtained with the bundles of $P/D = 1.02$ and $P/D = 1.42$ with their respective uncertainties.

P/D	ΔP	X_1	X_2	X_3	$U_{\Delta P}$	U_{X_1}	U_{X_2}	U_{X_3}
1.02	3.75 ± 0.38	0.50 ± 0.00	1.55 ± 0.00	0.14 ± 0.01	10%	0.1%	0.2%	5.5%
1.42	2.65 ± 0.20	0.77 ± 0.04	1.09 ± 0.14	1.06 ± 0.01	7.6 %	5.0 %	13 %	1.2 %

3.3 Numerical Dataset

The new dataset of numerical simulations has 93 bundles with friction factor and flow split data. The points follow a regular distribution through the geometrical parameters. Thus, there is data at $P/D = [1.02, 1.12, 1.22, 1.32, 1.42]$, $H/D = [8, 19, 30, 41, 52]$, and $N_r = [7, 19, 37, 61, 91]$. The dataset presented in this work does not contain any simulation representative of the exact geometry of an known experimental bundle. Figure 3.11 shows the distribution of the numerical and the experimental data, highlighting how the superpose each other. The experimental data is limited to $P/D < 1.256$, while the claimed validity of UCTD is for $1.02 \leq P/D \leq 1.42$. The numerical dataset closes this data gap. Moreover, the experimental data is clustered around some geometries, leaving considerable windows in its range without data. The CFD dataset do not have bundles with more than 91 pins, or 5 rings of rods around the central rod. Although the expansion of the dataset beyond 5 rings may be an important expansion of this work, the results obtained with this dataset presented in chapter 4 suggest that this problem is not very sensitive to the number of

pins for $N_r > 91$.
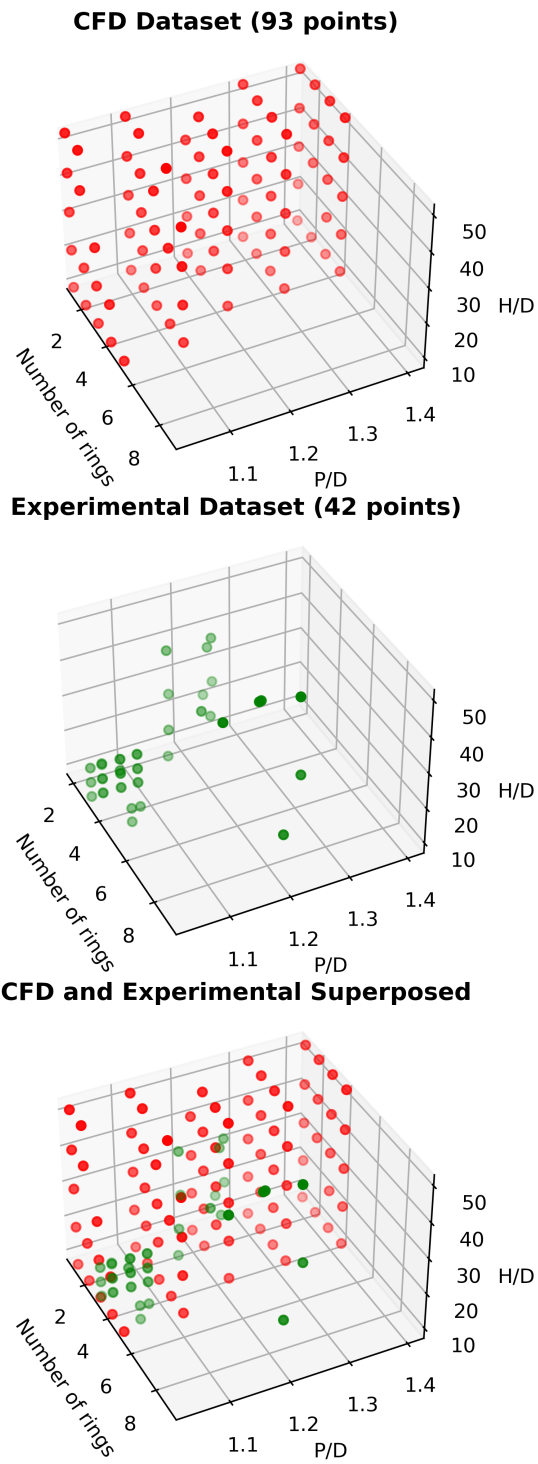
Figure 3.11: Distribution of the numerical and the experimental data in N_r, P/D, and H/D.

Figure 3.12 shows the histograms of the numerical and experimental dataset in N_r, P/D, and H/D, highlighting how the numerical dataset expands the data availability in P/D and H/D. Although there there are bundles with $N_r > 91$ in the experimental dataset, their number is also limited. Nevertheless, the model presented in this work was still able to predict them accurately even with the ANN being trained with the presented numerical dataset.
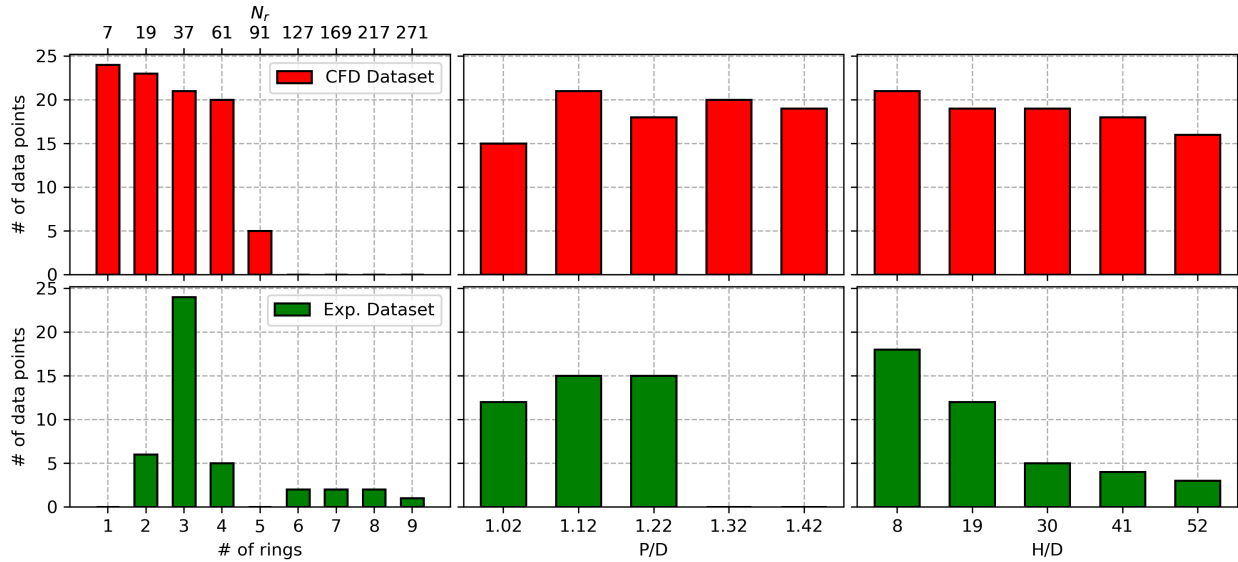
Figure 3.12: Histograms of the data distribution in N_r (left), P/D (center), and H/D (right).

Table 3.4 presents the geometrical information of the simulated bundles in the dataset. Each bundle has an identifier in the format $nXXpY\_YYhZZ$, where XX is the number of pins, Y_YY the P/D, and ZZ the H/D. Table 3.4 also presents the results of friction factor (f_b) and flow split (X_i).

Table 3.4: CFD dataset.

ID	Geometry and Results				
	N_r	D	D_w	P/D	H/D
n7p1_02h8	7	10	0.2	1.02	8
	f_b	X_1	X_2	X_3	
	0.154	0.590	1.297	0.222	
	N_r	D	D_w	P/D	H/D
n7p1_02h19	7	10	0.2	1.02	19
	f_b	X_1	X_2	X_3	
	0.153	0.585	1.300	0.221	
	N_r	D	D_w	P/D	H/D
n7p1_02h30	7	10	0.2	1.02	30
	f_b	X_1	X_2	X_3	
	0.152	0.587	1.299	0.220	
	N_r	D	D_w	P/D	H/D
n7p1_02h41	7	10	0.2	1.02	41
	f_b	X_1	X_2	X_3	
	0.152	0.584	1.300	0.220	
	N_r	D	D_w	P/D	H/D
n7p1_02h52	7	10	0.2	1.02	52
	f_b	X_1	X_2	X_3	
	0.152	0.594	1.296	0.219	

Table 3.4 continued from previous page

ID	Geometry and Results				
	N_r	D	D_w	P/D	H/D
n19p1_02h8	19	10	0.2	1.02	8
	f_b	X_1	X_2	X_3	
	0.164	0.635	1.372	0.238	
	N_r	D	D_w	P/D	H/D
n19p1_02h19	19	10	0.2	1.02	19
	f_b	X_1	X_2	X_3	
	0.165	0.633	1.373	0.239	
	N_r	D	D_w	P/D	H/D
n19p1_02h41	19	10	0.2	1.02	41
	f_b	X_1	X_2	X_3	
	0.156	0.607	1.396	0.229	
	N_r	D	D_w	P/D	H/D
n19p1_02h52	19	10	0.2	1.02	52
	f_b	X_1	X_2	X_3	
	0.163	0.638	1.369	0.236	
	N_r	D	D_w	P/D	H/D
n37p1_02h8	37	10	0.2	1.02	8
	f_b	X_1	X_2	X_3	
	0.170	0.671	1.482	0.253	

Table 3.4 continued from previous page

ID	Geometry and Results				
	N_r	D	D_w	P/D	H/D
n37p1_02h19	37	10	0.2	1.02	19
	f_b	X_1	X_2	X_3	
	0.165	0.648	1.513	0.247	
	N_r	D	D_w	P/D	H/D
n37p1_02h30	37	10	0.2	1.02	30
	f_b	X_1	X_2	X_3	
	0.160	0.646	1.513	0.240	
	N_r	D	D_w	P/D	H/D
n61p1_02h8	61	10	0.2	1.02	8
	f_b	X_1	X_2	X_3	
	0.173	0.712	1.531	0.272	
	N_r	D	D_w	P/D	H/D
n61p1_02h19	61	10	0.2	1.02	19
	f_b	X_1	X_2	X_3	
	0.169	0.690	1.570	0.266	
	N_r	D	D_w	P/D	H/D
n91p1_02h8	91	10	0.2	1.02	8
	f_b	X_1	X_2	X_3	
	0.171	0.720	1.656	0.280	

Table 3.4 continued from previous page

ID	Geometry and Results				
	N_r	D	D_w	P/D	H/D
n7p1_12h8	7	10	1.2	1.12	8
	f_b	X_1	X_2	X_3	
	0.377	0.783	1.209	0.660	
	N_r	D	D_w	P/D	H/D
n7p1_12h19	7	10	1.2	1.12	19
	f_b	X_1	X_2	X_3	
	0.321	0.779	1.239	0.565	
	N_r	D	D_w	P/D	H/D
n7p1_12h30	7	10	1.2	1.12	30
	f_b	X_1	X_2	X_3	
	0.306	0.768	1.252	0.538	
	N_r	D	D_w	P/D	H/D
n7p1_12h41	7	10	1.2	1.12	41
	f_b	X_1	X_2	X_3	
	0.300	0.762	1.257	0.532	
	N_r	D	D_w	P/D	H/D
n7p1_12h52	7	10	1.2	1.12	52
	f_b	X_1	X_2	X_3	
	0.296	0.761	1.259	0.526	

Table 3.4 continued from previous page

ID	Geometry and Results				
	N_r	D	D_w	P/D	H/D
n19p1_12h8	19	10	1.2	1.12	8
	f_b	X_1	X_2	X_3	
	0.373	0.798	1.258	0.646	
	N_r	D	D_w	P/D	H/D
n19p1_12h19	19	10	1.2	1.12	19
	f_b	X_1	X_2	X_3	
	0.323	0.791	1.276	0.568	
	N_r	D	D_w	P/D	H/D
n19p1_12h30	19	10	1.2	1.12	30
	f_b	X_1	X_2	X_3	
	0.311	0.787	1.283	0.550	
	N_r	D	D_w	P/D	H/D
n19p1_12h41	19	10	1.2	1.12	41
	f_b	X_1	X_2	X_3	
	0.306	0.785	1.286	0.546	
	N_r	D	D_w	P/D	H/D
n19p1_12h52	19	10	1.2	1.12	52
	f_b	X_1	X_2	X_3	
	0.302	0.782	1.290	0.539	

Table 3.4 continued from previous page

ID	Geometry and Results				
	N_r	D	D_w	P/D	H/D
n37p1_12h8	37	10	1.2	1.12	8
	f_b	X_1	X_2	X_3	
	0.375	0.829	1.291	0.667	
	N_r	D	D_w	P/D	H/D
n37p1_12h19	37	10	1.2	1.12	19
	f_b	X_1	X_2	X_3	
	0.325	0.818	1.316	0.582	
	N_r	D	D_w	P/D	H/D
n37p1_12h30	37	10	1.2	1.12	30
	f_b	X_1	X_2	X_3	
	0.313	0.817	1.319	0.567	
	N_r	D	D_w	P/D	H/D
n37p1_12h41	37	10	1.2	1.12	41
	f_b	X_1	X_2	X_3	
	0.310	0.817	1.319	0.565	
	N_r	D	D_w	P/D	H/D
n61p1_12h8	61	10	1.2	1.12	8
	f_b	X_1	X_2	X_3	
	0.377	0.849	1.328	0.692	

Table 3.4 continued from previous page

ID	Geometry and Results				
	N_r	D	D_w	P/D	H/D
n61p1_12h30	61	10	1.2	1.12	30
	f_b	X_1	X_2	X_3	
	0.315	0.837	1.358	0.589	
	N_r	D	D_w	P/D	H/D
n61p1_12h52	61	10	1.2	1.12	52
	f_b	X_1	X_2	X_3	
	0.308	0.837	1.359	0.581	
	N_r	D	D_w	P/D	H/D
n91p1_12h8	91	10	1.2	1.12	8
	f_b	X_1	X_2	X_3	
	0.379	0.869	1.347	0.700	
	N_r	D	D_w	P/D	H/D
n91p1_12h19	91	10	1.2	1.12	19
	f_b	X_1	X_2	X_3	
	0.328	0.854	1.391	0.603	
	N_r	D	D_w	P/D	H/D
n91p1_12h30	91	10	1.2	1.12	30
	f_b	X_1	X_2	X_3	
	0.317	0.856	1.387	0.592	

Table 3.4 continued from previous page

ID	Geometry and Results				
	N_r	D	D_w	P/D	H/D
n91p1_12h41	91	10	1.2	1.12	41
	f_b	X_1	X_2	X_3	
	0.313	0.858	1.382	0.590	
	N_r	D	D_w	P/D	H/D
n7p1_22h8	7	10	2.2	1.22	8
	f_b	X_1	X_2	X_3	
	0.459	0.810	1.103	0.984	
	N_r	D	D_w	P/D	H/D
n7p1_22h19	7	10	2.2	1.22	19
	f_b	X_1	X_2	X_3	
	0.374	0.873	1.110	0.868	
	N_r	D	D_w	P/D	H/D
n7p1_22h30	7	10	2.2	1.22	30
	f_b	X_1	X_2	X_3	
	0.354	0.869	1.129	0.818	
	N_r	D	D_w	P/D	H/D
n7p1_22h41	7	10	2.2	1.22	41
	f_b	X_1	X_2	X_3	
	0.342	0.865	1.144	0.780	

Table 3.4 continued from previous page

ID	Geometry and Results				
	N_r	D	D_w	P/D	H/D
n19p1_22h8	19	10	2.2	1.22	8
	f_b	X_1	X_2	X_3	
	0.450	0.850	1.153	1.014	
	N_r	D	D_w	P/D	H/D
n19p1_22h19	19	10	2.2	1.22	19
	f_b	X_1	X_2	X_3	
	0.368	0.878	1.147	0.873	
	N_r	D	D_w	P/D	H/D
n19p1_22h30	19	10	2.2	1.22	30
	f_b	X_1	X_2	X_3	
	0.350	0.874	1.159	0.826	
	N_r	D	D_w	P/D	H/D
n19p1_22h41	19	10	2.2	1.22	41
	f_b	X_1	X_2	X_3	
	0.341	0.872	1.166	0.797	
	N_r	D	D_w	P/D	H/D
n19p1_22h52	19	10	2.2	1.22	52
	f_b	X_1	X_2	X_3	
	0.336	0.868	1.174	0.776	

Table 3.4 continued from previous page

ID	Geometry and Results				
	N_r	D	D_w	P/D	H/D
n37p1_22h19	37	10	2.2	1.22	19
	f_b	X_1	X_2	X_3	
	0.363	0.893	1.180	0.885	
	N_r	D	D_w	P/D	H/D
n37p1_22h30	37	10	2.2	1.22	30
	f_b	X_1	X_2	X_3	
	0.347	0.888	1.192	0.843	
	N_r	D	D_w	P/D	H/D
n37p1_22h41	37	10	2.2	1.22	41
	f_b	X_1	X_2	X_3	
	0.339	0.888	1.196	0.815	
	N_r	D	D_w	P/D	H/D
n37p1_22h52	37	10	2.2	1.22	52
	f_b	X_1	X_2	X_3	
	0.335	0.885	1.202	0.803	
	N_r	D	D_w	P/D	H/D
n61p1_22h8	61	10	2.2	1.22	8
	f_b	X_1	X_2	X_3	
	0.442	0.895	1.215	1.046	

Table 3.4 continued from previous page

ID	Geometry and Results				
	N_r	D	D_w	P/D	H/D
n61p1_22h19	61	10	2.2	1.22	19
	f_b	X_1	X_2	X_3	
	0.359	0.909	1.198	0.877	
	N_r	D	D_w	P/D	H/D
n61p1_22h30	61	10	2.2	1.22	30
	f_b	X_1	X_2	X_3	
	0.344	0.904	1.210	0.837	
	N_r	D	D_w	P/D	H/D
n61p1_22h41	61	10	2.2	1.22	41
	f_b	X_1	X_2	X_3	
	0.337	0.904	1.213	0.818	
	N_r	D	D_w	P/D	H/D
n61p1_22h52	61	10	2.2	1.22	52
	f_b	X_1	X_2	X_3	
	0.333	0.902	1.217	0.804	
	N_r	D	D_w	P/D	H/D
n7p1_32h8	7	10	3.2	1.32	8
	f_b	X_1	X_2	X_3	
	0.493	0.792	1.093	1.036	

Table 3.4 continued from previous page

ID	Geometry and Results				
	N_r	D	D_w	P/D	H/D
n7p1_32h19	7	10	3.2	1.32	19
	f_b	X_1	X_2	X_3	
	0.377	0.877	1.078	0.958	
	N_r	D	D_w	P/D	H/D
n7p1_32h30	7	10	3.2	1.32	30
	f_b	X_1	X_2	X_3	
	0.353	0.886	1.083	0.932	
	N_r	D	D_w	P/D	H/D
n7p1_32h41	7	10	3.2	1.32	41
	f_b	X_1	X_2	X_3	
	0.343	0.889	1.090	0.910	
	N_r	D	D_w	P/D	H/D
n7p1_32h52	7	10	3.2	1.32	52
	f_b	X_1	X_2	X_3	
	0.335	0.889	1.097	0.889	
	N_r	D	D_w	P/D	H/D
n19p1_32h8	19	10	3.2	1.32	8
	f_b	X_1	X_2	X_3	
	0.485	0.851	1.138	1.078	

Table 3.4 continued from previous page

ID	Geometry and Results				
	N_r	D	D_w	P/D	H/D
n19p1_32h19	19	10	3.2	1.32	19
	f_b	X_1	X_2	X_3	
	0.371	0.893	1.112	0.982	
	N_r	D	D_w	P/D	H/D
n19p1_32h30	19	10	3.2	1.32	30
	f_b	X_1	X_2	X_3	
	0.349	0.895	1.116	0.950	
	N_r	D	D_w	P/D	H/D
n19p1_32h41	19	10	3.2	1.32	41
	f_b	X_1	X_2	X_3	
	0.338	0.894	1.121	0.930	
	N_r	D	D_w	P/D	H/D
n19p1_32h52	19	10	3.2	1.32	52
	f_b	X_1	X_2	X_3	
	0.332	0.894	1.123	0.914	
	N_r	D	D_w	P/D	H/D
n37p1_32h8	37	10	3.2	1.32	8
	f_b	X_1	X_2	X_3	
	0.478	0.881	1.170	1.101	

Table 3.4 continued from previous page

ID	Geometry and Results				
n37p1_32h19	N_r	D	D_w	P/D	H/D
	37	10	3.2	1.32	19
	f_b	X_1	X_2	X_3	
	0.364	0.910	1.139	0.994	
n37p1_32h30	N_r	D	D_w	P/D	H/D
	37	10	3.2	1.32	30
	f_b	X_1	X_2	X_3	
	0.344	0.906	1.143	0.958	
n37p1_32h41	N_r	D	D_w	P/D	H/D
	37	10	3.2	1.32	41
	f_b	X_1	X_2	X_3	
	0.334	0.908	1.148	0.943	
n37p1_32h52	N_r	D	D_w	P/D	H/D
	37	10	3.2	1.32	52
	f_b	X_1	X_2	X_3	
	0.328	0.908	1.149	0.928	
n61p1_32h8	N_r	D	D_w	P/D	H/D
	61	10	3.2	1.32	8
	f_b	X_1	X_2	X_3	
	0.474	0.905	1.182	1.105	

Table 3.4 continued from previous page

ID	Geometry and Results				
	N_r	D	D_w	P/D	H/D
n61p1_32h19	61	10	3.2	1.32	19
	f_b	X_1	X_2	X_3	
	0.358	0.927	1.148	0.990	
	N_r	D	D_w	P/D	H/D
n61p1_32h30	61	10	3.2	1.32	30
	f_b	X_1	X_2	X_3	
	0.339	0.926	1.154	0.958	
	N_r	D	D_w	P/D	H/D
n61p1_32h41	61	10	3.2	1.32	41
	f_b	X_1	X_2	X_3	
	0.330	0.924	1.159	0.940	
	N_r	D	D_w	P/D	H/D
n61p1_32h52	61	10	3.2	1.32	52
	f_b	X_1	X_2	X_3	
	0.325	0.924	1.161	0.927	
	N_r	D	D_w	P/D	H/D
n7p1_42h8	7	10	4.2	1.42	8
	f_b	X_1	X_2	X_3	
	0.526	0.771	1.091	1.062	

Table 3.4 continued from previous page

ID	Geometry and Results				
	N_r	D	D_w	P/D	H/D
n7p1_42h19	7	10	4.2	1.42	19
	f_b	X_1	X_2	X_3	
	0.377	0.866	1.072	0.988	
	N_r	D	D_w	P/D	H/D
n7p1_42h30	7	10	4.2	1.42	30
	f_b	X_1	X_2	X_3	
	0.348	0.875	1.073	0.973	
	N_r	D	D_w	P/D	H/D
n7p1_42h41	7	10	4.2	1.42	41
	f_b	X_1	X_2	X_3	
	0.335	0.881	1.074	0.961	
	N_r	D	D_w	P/D	H/D
n7p1_42h52	7	10	4.2	1.42	52
	f_b	X_1	X_2	X_3	
	0.327	0.886	1.077	0.949	
	N_r	D	D_w	P/D	H/D
n19p1_42h8	19	10	4.2	1.42	8
	f_b	X_1	X_2	X_3	
	0.519	0.848	1.132	1.097	

Table 3.4 continued from previous page

ID	Geometry and Results				
	N_r	D	D_w	P/D	H/D
n19p1_42h30	19	10	4.2	1.42	30
	f_b	X_1	X_2	X_3	
	0.343	0.900	1.101	0.990	
	N_r	D	D_w	P/D	H/D
n19p1_42h41	19	10	4.2	1.42	41
	f_b	X_1	X_2	X_3	
	0.331	0.900	1.103	0.978	
	N_r	D	D_w	P/D	H/D
n19p1_42h52	19	10	4.2	1.42	52
	f_b	X_1	X_2	X_3	
	0.323	0.901	1.104	0.967	
	N_r	D	D_w	P/D	H/D
n37p1_42h8	37	10	4.2	1.42	8
	f_b	X_1	X_2	X_3	
	0.511	0.882	1.161	1.121	
	N_r	D	D_w	P/D	H/D
n37p1_42h19	37	10	4.2	1.42	19
	f_b	X_1	X_2	X_3	
	0.362	0.918	1.121	1.024	

Table 3.4 continued from previous page

ID	Geometry and Results				
	N_r	D	D_w	P/D	H/D
n37p1_42h30	37	10	4.2	1.42	30
	f_b	X_1	X_2	X_3	
	0.337	0.917	1.124	1.004	
	N_r	D	D_w	P/D	H/D
n37p1_42h41	37	10	4.2	1.42	41
	f_b	X_1	X_2	X_3	
	0.326	0.916	1.127	0.992	
	N_r	D	D_w	P/D	H/D
n37p1_42h52	37	10	4.2	1.42	52
	f_b	X_1	X_2	X_3	
	0.319	0.916	1.129	0.982	
	N_r	D	D_w	P/D	H/D
n61p1_42h8	61	10	4.2	1.42	8
	f_b	X_1	X_2	X_3	
	0.505	0.905	1.176	1.132	
	N_r	D	D_w	P/D	H/D
n61p1_42h19	61	10	4.2	1.42	19
	f_b	X_1	X_2	X_3	
	0.355	0.934	1.129	1.028	

Table 3.4 continued from previous page

ID	Geometry and Results				
	N_r	D	D_w	P/D	H/D
n61p1_42h30	61	10	4.2	1.42	30
	f_b	X_1	X_2	X_3	
	0.331	0.932	1.134	1.010	
	N_r	D	D_w	P/D	H/D
n61p1_42h41	61	10	4.2	1.42	41
	f_b	X_1	X_2	X_3	
	0.321	0.931	1.138	0.997	
	N_r	D	D_w	P/D	H/D
n61p1_42h52	61	10	4.2	1.42	52
	f_b	X_1	X_2	X_3	
	0.315	0.930	1.140	0.987	

3.4 Conclusions

The work presented in this section took advantage of the knowledge available in a vast repository in the literature of CFD simulations of wire-wrapped rod bundles to propose a numerical model for the laminar regime. The main challenges in these bundles' spatial discretization were addressed by smoothing the contacts between the wire and the rods and the walls as proposed in previous studies. The spatial discretization was validated using the GCI method. 93 bundles were simulated using the code STAR-CCM+, covering a wide range of P/D and H/D. This work provides an expanded dataset of laminar flows in wire-wrapped rod bundles to support the development of correlations valid for a more comprehensive range of geometries.

4.   ARTIFICIAL NEURAL NETWORK PREDICTION MODEL

Artificial Neural Networks (ANN) have become the preferred machine learning for many applications. Compared to other machine learning methods for regression, ANNs require fewer problem-specific implementations. The workflow generally concentrates on the data pre-process and definition of the parameters of control of the learning process (hyperparameters). This generality of ANNs makes possible the use of publicly available software libraries that not only are highly optimized but also have a vast commercial and academic community of developers and users, such as TensorFlow [45], and PyTorch [46].

When applied to regression problems, ANNs are recognized as highly capable of approximating non-linear functions, a feature often referred to as "Universal Approximation Property." While some studies [47, 48] demonstrated that an ANN with one single hidden layer could fit complex non-linear functions, it may require a hidden layer with an unpractical number of nodes. The capacity to approximate complex functions is also achieved by adjusting the number of hidden layers [49] or the network depth. ANNs with multiple hidden layers are often called Deep Neural Networks (DNN), and the machine learning field concerned with the development and use of DNNs is denominated Deep Learning.

Regression using ANNs is used to generate surrogates for several functions in engineering. The ANN-based surrogates are often used to support an optimization problem, mitigating the data sparsity. In this case, the ANN interpolates the data, which can be numerical [50, 51, 52] of experimental [53]. In some cases, the obtained surrogate provides the cost function to an optimizer. GPU-optimized convolutional neural networks, a special case of sparsely connected ANNs, are capable of reproducing the full flow field of CFD simulations over four orders of magnitude faster than CPU-based CFD solvers [54].

4.1 The Artificial Neural Network

The neural network concept is based on the simplified knowledge of how the human brain works. Unit neurons receive the information obtained from the synapses with other neurons and transmit a response to the subsequent neurons. The complex processes of a nervous system result from the multiple interactions between each neuron. The elementary unit of an artificial neural network is the perceptron. It consists of the summation of all the inputs x weighted by w plus a trainable bias term b applied to a transfer function σ. Therefore the output o_j of a perceptron is given by Equation 4.1. The basic architecture of a perceptron is shown in Figure 4.1

$$o_j = \sigma(b_j + \sum_{i=1}^{n} x_{ij} w_{ij}) \tag{4.1}$$
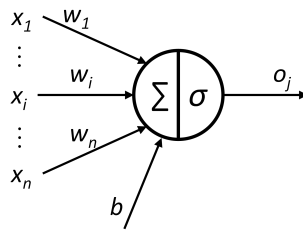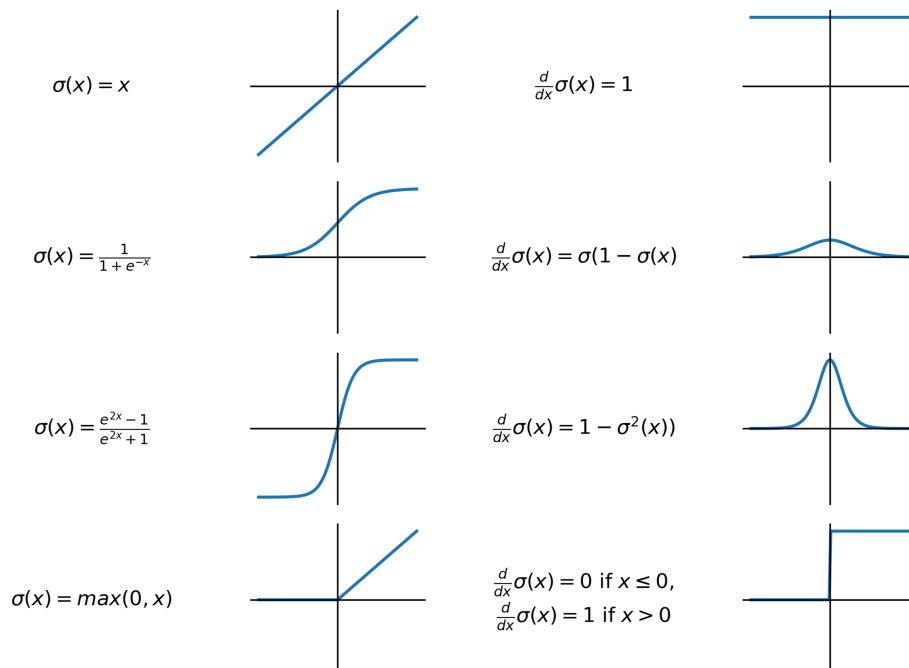

Figure 4.1: Basic architecture of a perceptron.

The transfer functions convert the inputs from the previous layer into an output. The transfer function will attribute a decision character to the node, often associated with a probability distribution. The most common transfer functions in use for ANNs are presented in Table 4.1. There are no rules to define what transfer function is better suited to each problem, with the selection being often empirical. The most used transfer function is the Rectified Linear Unit ($ReLu$). However, its application is generally for deep neural networks and Convolutional Neural Networks, often with more than ten hidden layers. The $ReLu$ function offers the advantage of neutralizing some of the nodes as they assume zero values when the inputs become negative. They alleviate the burden

of training by simplifying the gradient calculation to zero. Thus, the network becomes virtually a sparse ANN, decreasing the tendency to overfitting and increasing training efficiency. Its application to smaller networks, especially for regression, is limited since its discontinuous derivative tends to create oscillations to gradients during optimization. For this role, the hyperbolic tangent ($tanh$) is one of the most popular transfer functions, as it provides values in both the positive and negative range and has a continuous derivative. During the early days of the ANN research, the $sigmoid$ function was the most common. It became out of favor as it returns only positive values and tends to zero when receiving negative values. The accumulation of zeroes in the network minimizes the gradients and stalls training, a limitation known as "gradient vanishing" [55].

Table 4.1: Common transfer functions for ANNs.

$\sigma(x) = x$		$\frac{d}{dx}\sigma(x) = 1$	
$\sigma(x) = \frac{1}{1+e^{-x}}$		$\frac{d}{dx}\sigma(x) = \sigma(1-\sigma(x)$	
$\sigma(x) = \frac{e^{2x}-1}{e^{2x}+1}$		$\frac{d}{dx}\sigma(x) = 1 - \sigma^2(x))$	
$\sigma(x) = max(0,x)$		$\frac{d}{dx}\sigma(x) = 0$ if $x \leq 0$, $\frac{d}{dx}\sigma(x) = 1$ if $x > 0$	

The perceptron is essentially a linear classifier. Although the transfer function may be non-linear, the function input is a linear combination of weights, meaning that the perceptron is not

capable of discovering non-linear relationships between a set of inputs and outputs. However, combining multiple layers of perceptrons with non-linear transfer functions forms a network capable of reproducing non-linear functions. Such a network is denominated the feed-forward neural network [56], or sometimes multi-layer perceptrons. Figure 4.2 shows the typical schematics of a densely connected feed-forward neural network.
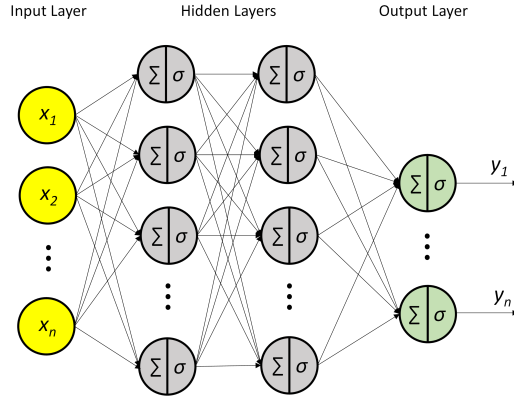

Figure 4.2: Basic architecture of a feed-forward neural network.

Training is performed using a dataset of size N given by $S = \{(\vec{x_i}, \vec{y_i} = f^*(x_i)), i \in [n]\}$. The weights of the network are adjusted using the backpropagation method [57] in such way that the network function f will approximate f^*. The most common error function used in backpropagation, and the one adopted in this study, is the mean squared error. The error function $E(X, \theta)$ for a set of weights and biases denoted θ and the calculated output $\hat{y}_i$ is calculated using Equation 4.2.

$$E(X, \theta) = \frac{1}{2N} \sum_{i=1}^{N} (\hat{y}_i - y_i)^2 \qquad (4.2)$$

$$E(X, \theta) = \frac{100\%}{N} \sum_{i=1}^{N} \left| \frac{\hat{y}_i - y_i}{\hat{y}_i} \right| \qquad (4.3)$$

The partial derivative of the error is calculated in respect to each weight by applying the chain rule (Equation 4.4), where $o_j^k = b_{jk} + \sum(x_{ij}^k w_{ij}^k)$.

70

$$\frac{\partial E}{\partial w_{ij}^k} = \frac{\partial E}{\partial a_j^k} \frac{\partial a_j^k}{\partial w_{ij}^k} \tag{4.4}$$

The weights are adjusted at each training step (t). In the most simple form of backpropagation, the change in the weight value is proportional to a learning rate coefficient (α) and the gradient $\frac{\partial E}{\partial w_{ij}^k}$. This strategy of optimizing a function by applying steps related to the function gradient is defined as gradient descent.

Several gradient-based algorithms have been proposed in order to improve the optimization efficiency [58, 59], with some of these developments accounting for some of the noticeable advancements in machine learning recently [60, 61]. The main addition from the most advanced methods to the aforementioned basic approach is incorporating momentum to the gradient descent. By building inertia in the search direction, the optimization with momentum becomes more resilient to gradient oscillations and helps the search to move on from flat spots. Algorithms with momentum generally converge faster and are less prone to get trapped at a local minimum.

The Adam [62] method for stochastic optimisation was adopted since it provided accurate results at a faster rate. The method employs adaptive learning rates for each parameter based on first and second moments of the gradients. The same coefficient values ($\alpha = 0.001$, $\beta_1 = 0.9$, $\beta_2 = 0.999$ and $\epsilon = 10^{-8}$) proposed by the authors of the method were used in this study. The two momentum vectors are initiated as zero, then they are calculated by Equations 4.5 and 4.6, respectively, for the current step t.

$$m_t = \beta_1 m_{t-1} + (1 - \beta_1) * \left[\frac{\partial E}{\partial w_t}\right] \tag{4.5}$$

$$v_t = \beta_2 v_{t-1} + (1 - \beta_2) * \left[\frac{\partial E}{\partial w_t}\right]^2 \tag{4.6}$$

Then the bias-corrected first and second moments estimate is computed using Equations 4.7 and 4.8, respectively.

$$\widehat{m_t} = \frac{m_t}{1 - \beta_1^t} \tag{4.7}$$

$$\widehat{v_t} = \frac{v_t}{1 - \beta_2^t} \tag{4.8}$$

Then, the updated weights are calculated based on Equation 4.9.

$$w_{t+1} = w_t - \widehat{m_t} \left(\frac{\alpha}{\sqrt{\widehat{v_t}} + \epsilon} \right) \tag{4.9}$$

4.2 Model definition

The objective of the presented neural network is to interpolate the results of pressure drop and flow split obtained with CFD as a function of the bundle geometry. The dataset is composed by 93 examples, where $x_i \in X := [Nr, \frac{P}{D}, \frac{H}{D}]^T$ and its respective label is $y_i \in Y := [f, X_1, X_2, X_3]^T$. The whole dataset was generated using CFD simulations following the procedure of Chapter 3.

A dataset has to be normalized before training; otherwise, the importance of each independent variable will be biased by its absolute value. The method adopted is the z-score, which means removing the mean of each variable and scaling the standard deviation to unity as in Equation 4.10. The $scaler$ is calculated for each parameter from the training data; then, a scaling layer is added to the input layer. The normalization of the variance decreases the gradient elongation, reducing the zig-zagging during the gradient descent towards the minimum [63].

$$scaler = \frac{x - \bar{x}}{\sigma(x)} \tag{4.10}$$

Apart from the historical decline in the interest for the $sigmoid$ function, it was selected for this model. As all the values involved in this problem are positive, the $sigmoid$ function performed well. The $sigmoid$ function also provided a marginal resistance against overfitting to the model, maybe by selectively neutralizing part of the network similar to the $ReLu$ function. It has the advantage of not introducing oscillations to the gradients, although without the benefit of decreas-

ing the computational cost. The computational cost of training the presented model is relatively low, especially when compared to the typical applications of large CNNs, such as compute vision, which often will involve networks with over tens of millions of trainable parameters. Therefore, a transfer function that improves accuracy and generalization at the cost of training efficiency is beneficial. The transfer function of the output layer is linear. The output of a network in a regression problem works more as a compiler of the results obtained from the hidden layers than a decision unit. The linear function helps stabilize the gradients during the first step of the backpropagation process.

The definition of the number of nodes and layers was empirical to minimize the error in the validation set. The ANN for this work has two hidden layers of 100 nodes each. This model is a dense network, as all nodes in a layer are fully connected to the nodes of the next one. This model is a considerably complex network when compared with other problems of apparent similar size and complexity. Kim et al. [64] used an ANN with a single hidden layer with 15 nodes to predict the bundle average friction factor in wire-wrapped rod bundles with the same dataset as for the UCTD correlation. This larger order of the adopted model provides much more generalization power, recognizing many more features. With the increased model order, however, overfitting becomes a dominant issue. When this model is trained with the CFD dataset at first, the optimization process always converges to a local minimum. The solutions have high variance, and the accuracy is relatively poor. However, the model can be pre-trained before seeing the actual dataset. The UCTD correlation provides the ideal pre-training dataset for this task, as it already approaches the actual function. Moreover, the UCTD correlation is a continuous function, meaning that it can provide infinite data points. There is no such thing as overfitting a continuous function; thus, the "Universal Approximation Property" is applicable.

4.3 Training

Pre-training uses a synthetic dataset of 90,000 data points generated using the original UCTD correlation. The synthetic dataset is formed by a regular grid of shape $9 \times 100 \times 100$ for $7 \leq Nr \leq 271$, $1.02 \leq P/D \leq 1.42$ and $8 \leq H/D \leq 52$. The data were randomly split into a training set and

a validation set in 80% and 20%, respectively. The pre-trained model predicts the synthetic dataset with a mean absolute error of 0.032%, and the maximum absolute error in the whole dataset was 0.047%. After that, the model starts the training with the numerical dataset from the point where it is virtually identical to the UCTD correlation. By starting from a similar function, the search space of this problem is reduced by several orders of magnitude. The pre-training strategy avoided the problem of local minimum trapping, and the final model did not present any concern about outfitting while benefiting from the high order model.

The training was performed using the k-fold cross-validation procedure. One of the primary concerns in this project was that the results could have high variance between the folds [65], especially considering the relatively large size of the ANN. Such characteristics could deem the model unusable as a representation of a continuous function or require averaging of multiple distinct trained learners to control the model variance [64].

The cross-validation was performed using five-folds, so the training/test split ratio of 80%/20%. Figure 4.3 shows the statistics obtained after training with the CFD using the k-fold cross-validation method for the CFD dataset (93 points), the validation dataset (42 points), and the same dataset used for pre-training (90,000 points). The variance of the model is very low, especially for an ANN. The 95th percentile of the standard deviation in the experimental dataset for f_b is 91%, while for X_3 it is 2.59%. The average standard deviation of X_3 is 0.98%, indicating that this method has very high repeatability.

It is noticeable that the variance between the folds in the 90,000 points dataset is slightly higher, with a 90th percentile of 2.23% for f_b and 3.49% for X_3. This uncertainty comes from the fact that the 90,000 points contain the larger bundles, in the range of $91 \leq N_r \leq 271$ pins, which the CFD dataset used for training lacks. Neural networks are exceptional interpolators but are substandard when extrapolating. Therefore, it is remarkable that the presented model can accurately predict the experimental bundles in the higher range of N_r with low variance.

The ANN provides a continuous function that represents the population of the CFD dataset. Figure 4.4 shows the curves of the ANN and UCTD functions for f_b in the space of P/D and
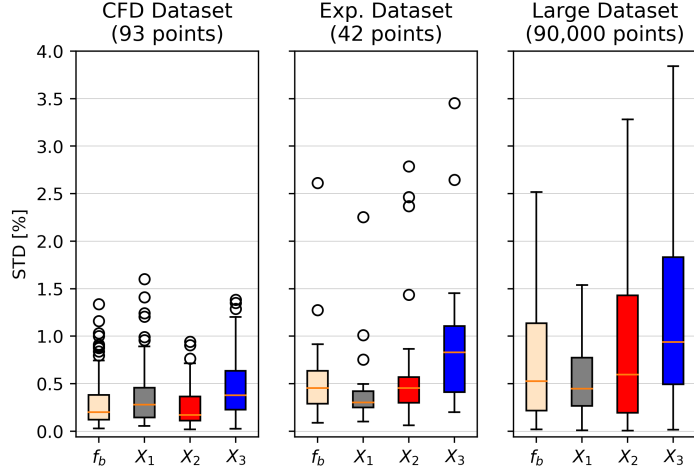
Figure 4.3: Distribution of the standard deviation between the 5 folds after training using the k-fold cross-validation for the dataset of CFD simulations (left), the dataset of experiments (center) and the dataset of 90,000 points used for pre-training with outliers omitted for clarity (right).

H/D for bundles with $7 \leq N_r \leq 61$ and $Re = 250$. As expected, due to the low variance of the ANN predictions, the curves from the ANN model are very smooth, as for UCTD. A well-defined trend to predict a large effect by the number of pins for large P/D and small H/D is observed in the UCTD function, while the ANN keeps the importance of the number of pins relatively small throughout the domain.

Figure 4.5 shows plots of f_b as a function of P/D for the values of H/D in the CFD dataset, $7 \leq N_r \leq 61$ and $Re = 250$. There is a good agreement between the ANN predictions and the CFD data points. The function obtained from the ANN is also smooth. These characteristics strongly support the conclusion that the ANN was capable of representing the underlying features of the CFD dataset. Therefore, the ANN represents the general population of numerical representations of wire-wrapped rod bundles in this range, keeping the simulation parameters. This property of the ANN model allows it to assume the place of other simulations for the whole range of validity of the training for a fraction of the computational cost.

Some critical divergences between the predictions of the ANN model and UCTD are observed in 4.5. The difference in the pin number effect for larger P/D and smaller H/D is notorious,
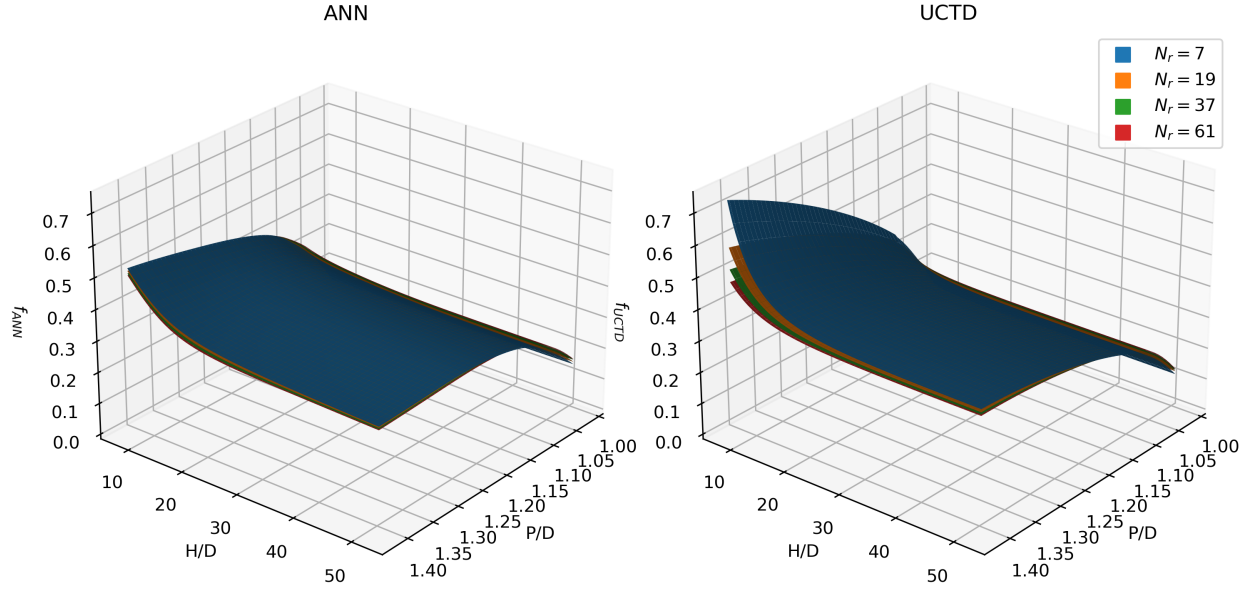
Figure 4.4: Plots of the friction factor as a function of P/D and H/D for the ANN model (left) and UCTD (right).

as observed in Figure 4.4. The extent where the pin effect is the largest is for $P/D > 1.25$. It coincides with the limit of P/D in the experimental dataset ($P/D = 1.256$), in which the UCTD correlation was calibrated. The ANN had data points from the CFD simulations to interpolate this area, while the UCTD correlation could only extrapolate this region for its calibration in the laminar regime. Another discrepant behavior between the two models is that the ANN predicts that for $H/D \approx 19$ the bundle average friction factor starts to decrease at a constant rate for $P/D > 1.2$. In contrast, the UCTD correlation predicts ever-increasing values for f_b in this study's range of P/D. However, the rate of increase in f_b for large P/D values also decreases with H/D for UCTD. Unfortunately, there are no experimental data points in this range for final verification of the behavior of both models, but the numerical data support this trend of the ANN model. Another region of these curves where the ANN and the UCTD disagreed is for f_b values of low P/D and high H/D, with UCTD tending to predict lower f_b values as H/D increases for low P/D. This area of the experimental dataset lacks data points, suggesting that the UCTD might be data starved in this area either. This tendency might be contributing to the higher pitch of

76

the UCTD correlation for larger H/D values. With the lower bound predicting lower values and the center of the range anchored on the experimental data, the overall slope of UCTD tends to be higher for high H/D than for the ANN.
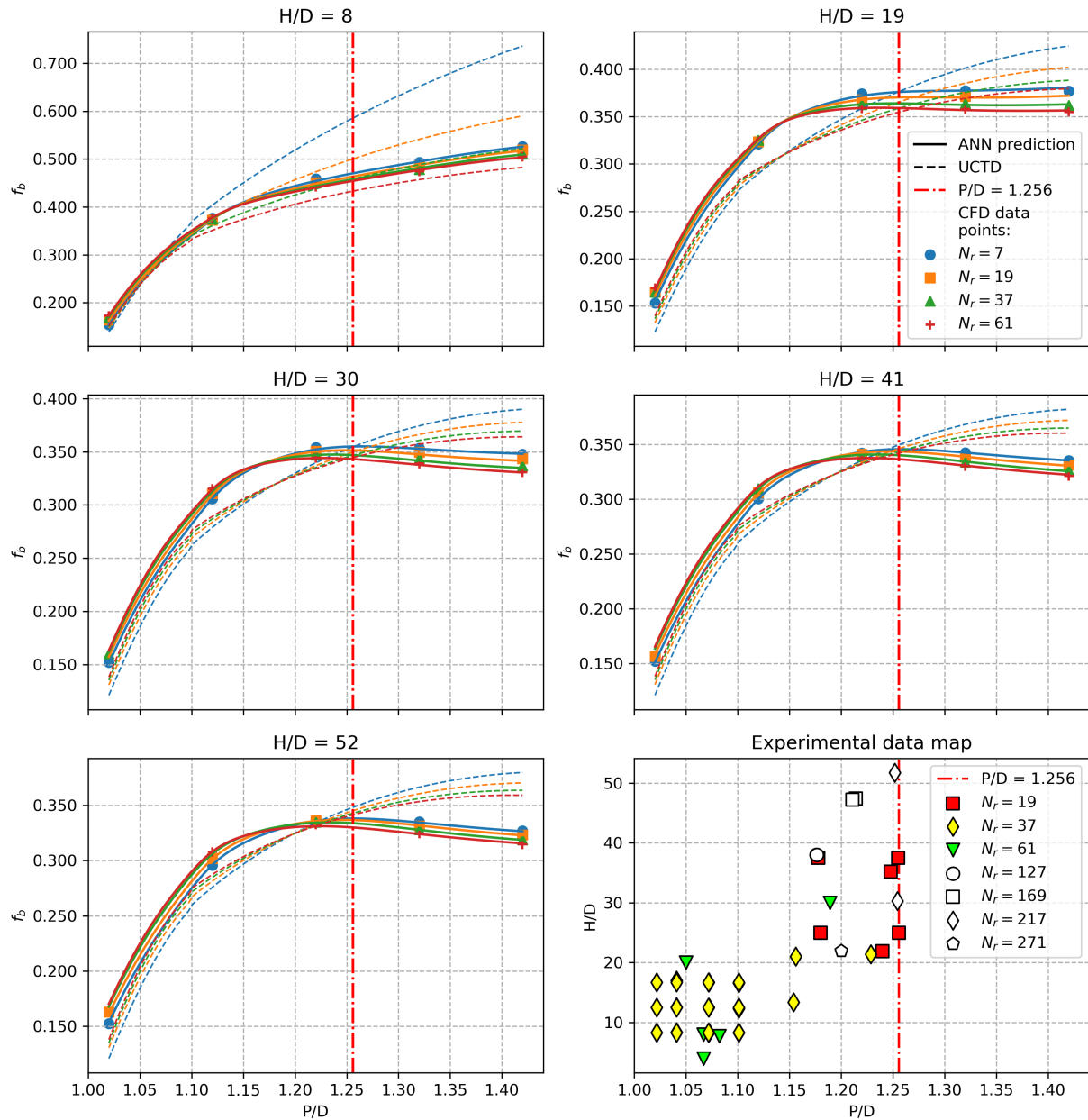

Figure 4.5: f_b as a function of P/D and H/D for bundles with different numbers of pins. The experimental data map (right, bottom) shows the distribution of the experimental dataset in P/D and H/D, with the largest P/D in the experiments delimited ($P/D = 1.126$).

The tendency of UCTD to present larger relative differences to the ANN model for f_b ($d_r^{f_b}$) further from the experimental data is visible in Figure 4.6. One may notice that the experimental points populate the level closer to the relative difference of zero. Moreover, some landmarks in the surface curves are associated with data clusters. For example, the wave at $P/D \approx 1.05$ is centered on the cluster of data points around this point, composed mostly of the Marten [4] bundles. Another area in Figure 4.6 where the trends of UCTD seems to be influenced by the data distribution is the presence of a tab of positive $d_r^{f_b}$ for low H/D and pin number that lowers to negative values as the number of pins increase. This tendency follows the distribution of N_r in the data, with more bundles with $N_r \leq 61$ (mostly $N_r = 37$) at lower P/D and more bundles with $N_r \geq 91$ at higher P/D.
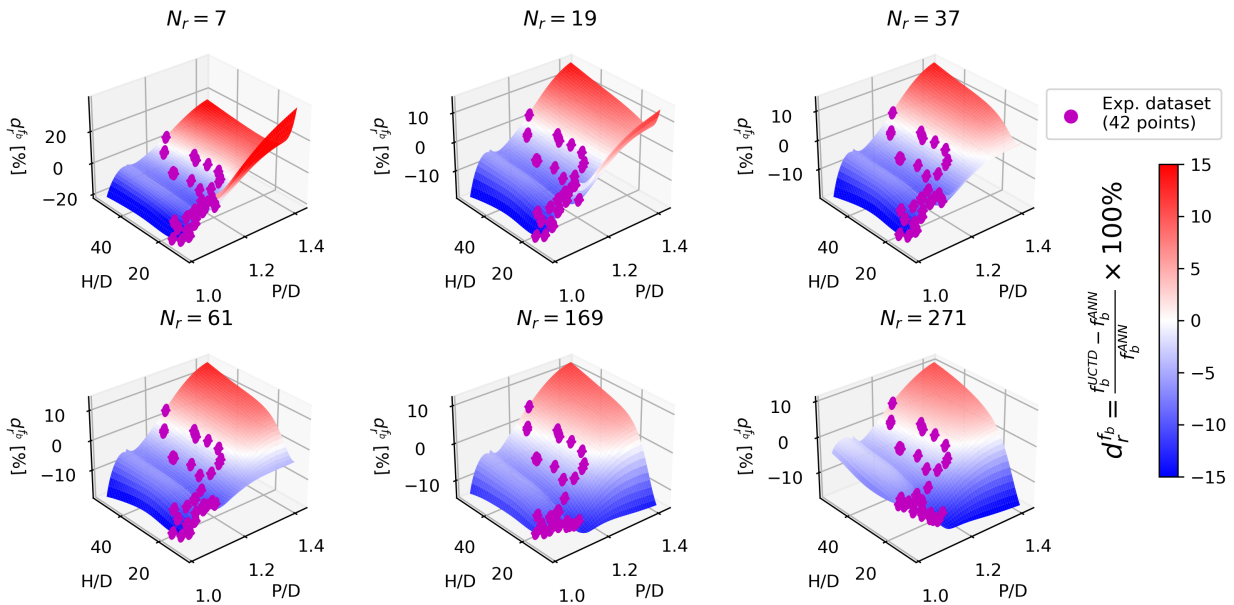

Figure 4.6: Relative differences between the predictions of the ANN model and UCTD for the bundle average friction factor.

Figure 4.7 shows X_1, X_2 and X_3 as a function of P/D. The ANN and the simulation points have an excellent agreement with UCTD for $H/D \geq 19$. The X_3 curves have a more visible divergence, but X_3 is respective to a minimal flow area; thus, any fluctuation in X_1 and X_2 will cause

an oversized response of X_3. Therefore, it still can be considered a good agreement. However, the predictions of UCTD strongly diverge from the ANN model for $H/D = 8$ as P/D increases. Not only is the magnitude of relative differences large, up to 93% for X_1 and 57% for X_2, but also the relative distribution of axial velocity changes. For instance, UCTD predicts that the axial velocity is considerably larger in the interior than in the edge.

The authors of UCTD [19], in the publication of the more recent PCTD correlation [66], note that the hydraulic diameter of the edge subchannels is larger than the interior. Therefore the mean axial velocity in the edge must be larger than the bundle average axial velocity, meaning that the condition of $X_2 > 1$ is necessary for physical validity. The ANN model predicts $X_2 > 1$ for the whole domain, while UCTD violates this condition for bundles with H/D up to 14 in this study's range of P/D.

The presence of bundles with $X_2 < 1$ in UCTD seems to stem from the dependence of UCTD on the experimental data distribution. Figure 4.8 shows the relative difference between UCTD and the ANN model for X_2 ($d_r^{X_2}$). The landmarks of the f_b relative difference surface seem to be strongly influenced by the distribution of the experimental data points. There are larger differences between the two models in a line close to $P/D = 1.15$, more visible for $N_r = 7$, which coincides with the separation between the two clusters of experimental data. For $d_r^{X_2}$, there is as a step slop towards larger P/D and smaller H/D. This region is where the furthest point in P/D from any experimental data is for a similar H/D.

This section demonstrated that the ANN represents the general trends and features of the numerical solutions across all the validity ranges. The CFD dataset is homogeneously distributed in the whole domain of P/D and H/D, meaning that the ANN model is statistically supported in all this range. On the other hand, all the current correlations for pressure drop in wire-wrapped rod bundles are dependent on experimental data, which is scarce. Under this perspective, even though UCTD has a robust formulation based on extensive domain knowledge, it is still susceptible to becoming dependent on the experimental data distribution, therefore prone to provide poor predictions when extrapolating the parameters of the experimental data.
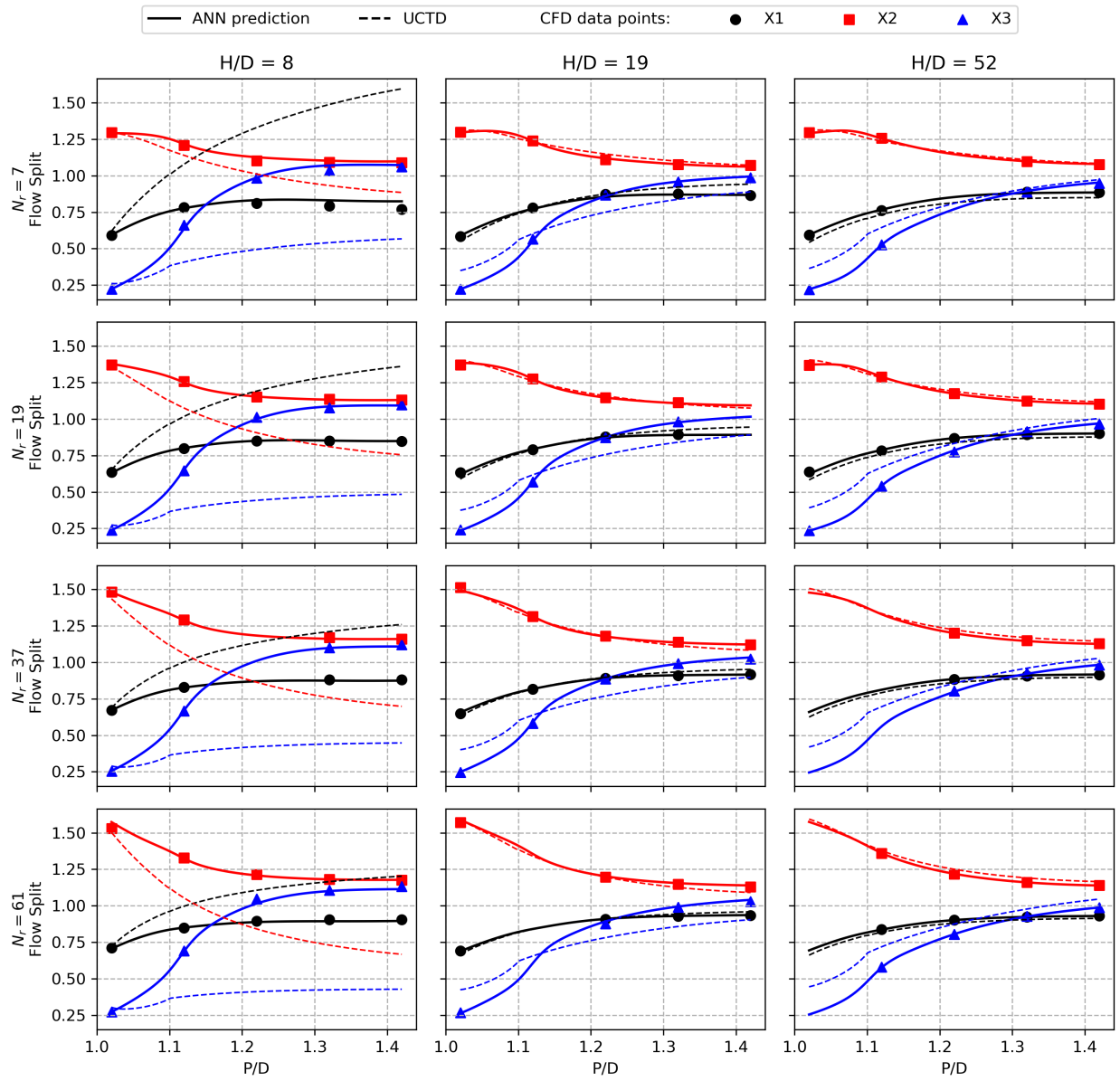
79

Figure 4.7: Flow split parameter for interior (X_1), edge (X_2) and corner (X_2) regions as a function of P/D and H/D for bundles with different numbers of pins.

4.4 Model Verification with Experimental Data

The ANN model accuracy for f_b and X_2 in the experimental data is evaluated and compared with the UCTD correlation. The reference for accuracy chosen for this work is the relative error to the measured values, as presented in Equation 4.11. The dispersion of the error is measured by
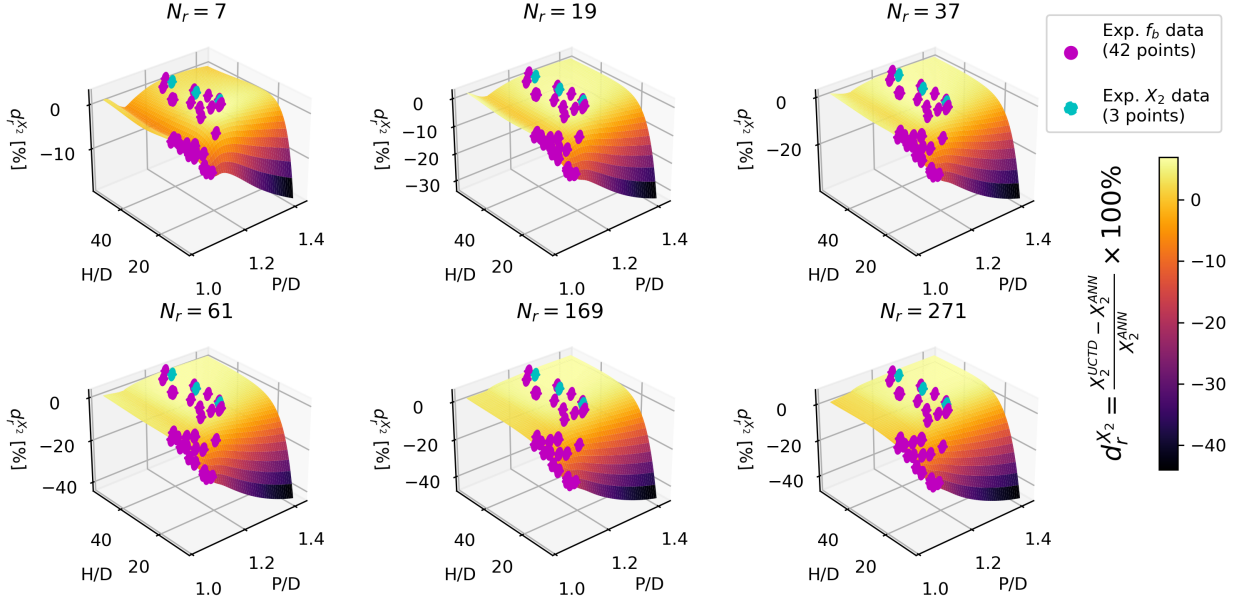
Figure 4.8: Relative differences between the predictions of the ANN model and UCTD for the flow split parameter in the edge region (X_2).

ϵ_{RMS}, as presented in Equation 4.14, where n is the total number of data points.

$$\epsilon = \frac{Prediction - Measurement}{Prediction} \times 100\% \qquad (4.11)$$

$$\epsilon_{Mean} = \frac{1}{n}\sum_n \epsilon_i \qquad (4.12)$$

$$\epsilon_{RMS} = \sqrt{\frac{1}{n}\sum_n \epsilon_i^2} \qquad (4.13)$$

There are 348 data points belonging to 42 bundles at several Reynolds numbers in the laminar regime. A direct evaluation of the predictions for f_b can be performed by comparing each measurement point with the respective prediction. Table 4.2 presents statistics of the relative errors for the ANN model and UCTD in this dataset.

Table 4.2: Mean and RMS of the prediction errors for the ANN model and UCTD for all the 348 data points (42 bundles) of bundle average friction factor in the laminar regime.

$Model$	Mean relative error (f_b)	RMS relative error (f_b)
ANN	10.0%	21.7%
$UCTD$	3.17%	17.7%

The similarity between the predictions of the two models for the experimental dataset is notorious. Figure 4.9 shows a comparison between the predicted and the measured values for f_b for all data points. This consistency between the ANN and UCTD, which are models distinct in their conceptual structures and calibration, highlights the intrinsic uncertainty of the data. The experimental data itself has its error distribution around the true function. Considering the agreement between the two models, this error distribution of measurements seems close to what the ANN and UCTD predict.
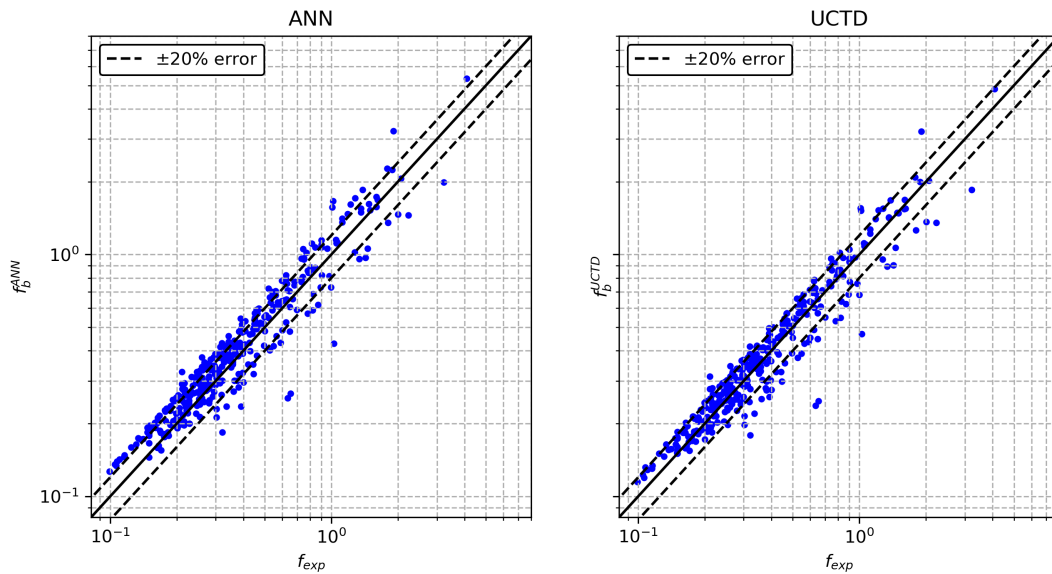

Figure 4.9: Comparison between the measured and the predicted values of average bundle friction factor (f_b).

The estimators of the predictions considering every measurement as individual data points may not represent the population correctly. The bundles in this dataset have different numbers of measurements. Moreover, each experiment has systematic errors from the instrumentation, facility characteristics, and experimental methods. By weighting each measurement point individually, the systematic errors of each bundle are weighted differently in the overall statistics. Besides that, not all the data dispersion quantified by ϵ_{RMS} is a result of the prediction variance. Since this data is for laminar flows, it is expected that the friction factor will follow the line of proportionality defined by C_{fbL}/Re. However, the measurements of each bundle are dispersed around this line due to random errors in the experiment itself.

Figure 4.10 shows examples of laminar data for Chun3 [23], Marten43 [4] and Engel [16]. For Chun3, both the ANN and UCTD predict data with good agreement to C_{fbL}^{exp}, and there is minimal dispersion of the experimental data around it. Thus, Chun3 contributes to good statistics of ϵ_{Mean} and ϵ_{RMS}. However, Chun3 has fewer measurement points in the laminar regime than Marten43 and Engel, so it has less impact on the general statistics if each measurement is accounted for individually. Marten43 will disproportionately introduce a bias to ϵ_{Mean} in the ANN, as the ANN disagrees more with the experimental data than UCTD, and this bundle has a larger number of measurements. The errors of the measurement points, however, are not statistically independent between them, since the relative position of the points is dependent on C_{fbL}^{exp}, so ϵ_{Mean} of the ANN is being overestimated. The Engel bundle has a considerable dispersal of the measurements around the C_{fbL}^{exp} slope; thus, this bundle will increase ϵ_{RMS} due to uncertainties of the experiment itself.

The accuracy is expressed in terms of the laminar friction factor constant of the experiment (C_{fbL}^{exp}), better representing the contribution to the overall statistics of each experiment. C_{fbL}^{exp} is calculated as the mean of $f_b \times Re$ for the measurements of an experiment in the laminar regime. The UCTD criterion for transition Reynolds is adopted. Figure 4.11 shows a comparison between C_{fbL}^{exp} and the predicted values denoted by C_{fbL}^{pred}. Besides the fact that the C_{fbL} plot makes it much easier to understand the distribution of the data, the real contribution of each experiment to the dataset is better demonstrated.
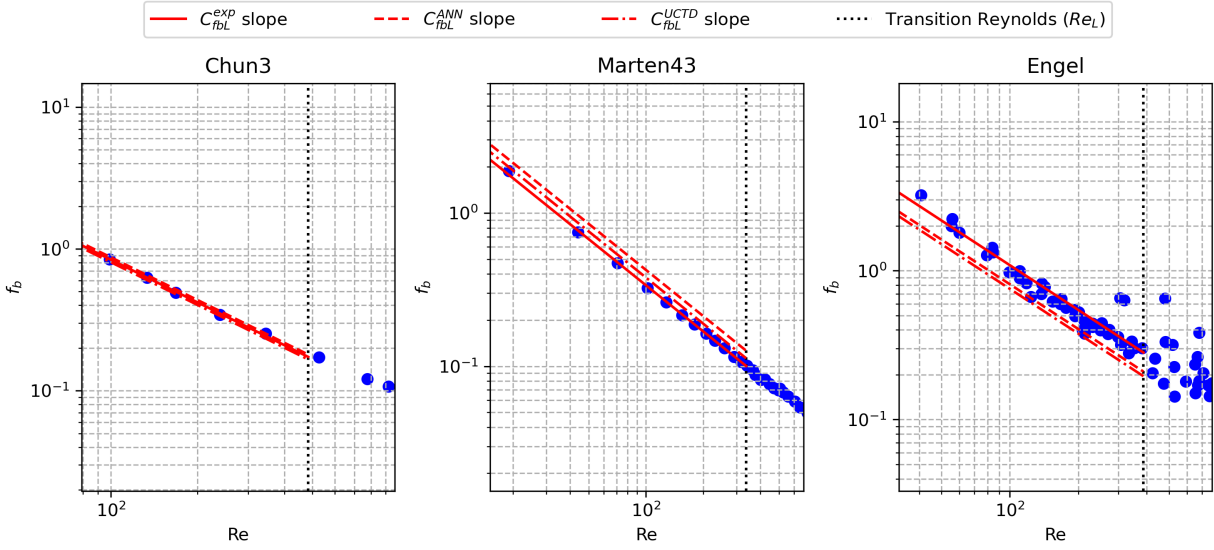
Figure 4.10: Friction factor as a function of Re with the

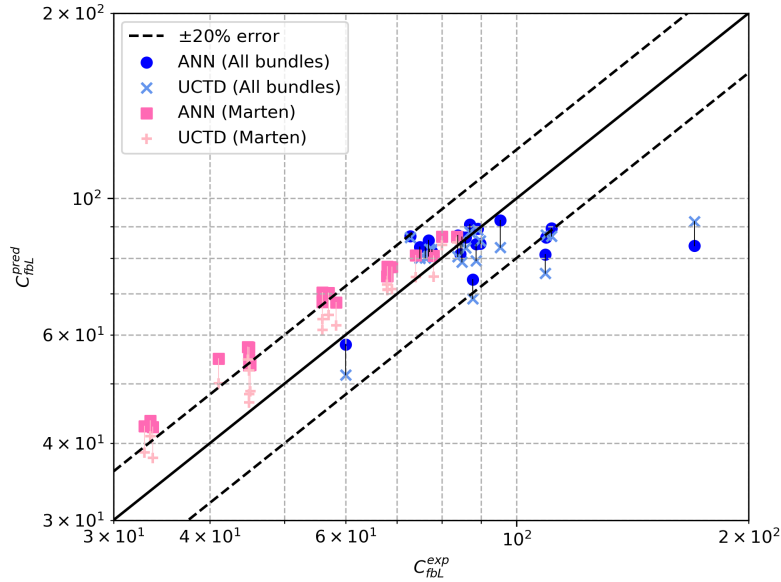$$C_{fbL}^{exp} = \frac{1}{n} \sum_n f_{b,i} Re_i \tag{4.14}$$

Figure 4.11: Relative error between the mean laminar friction factor coefficient (C_{fbL}^{exp}) of the experimental data and the predictions of the ANN and UCTD (C_{fbL}^{pred}).

The ANN model improves the predictions of C_{fbL} for most of the experiments, except for the ones performed by Marten. For this reason, all the experiments from Marten [3, 4] are highlighted to facilitate their identification. For all the other bundles, the ANN tends to partially correct under predictions while not worsening the results of the bundles over predicted by UCTD. Thus, there is a significant overall improvement, especially regarding the tendency of UCTD to underpredict. The tendency of both the ANN model and UCTD to predict higher C_{fbL} values for Marten is systematic, occurring in all this set of experiments.

Figure 4.12 shows the relative errors for C_{fbL} as a function of P/D. The distribution of the errors does not present any clear correlation with P/D. One aspect of the ANN predictions to be assessed is if their relative errors are dependent on the geometry. Since The ANN was entirely trained on CFD data, biases from numerical errors are the main concern. A distinguished skewness in the error distribution by the geometry would indicate inaccuracy in CFD results. However, no clear trend can be identified, highlighting the consistency of the CFD dataset. Figure 4.13 shows the relative errors for C_{fbL} as a function of H/D. No discernible correlation between the prediction errors of the ANN and H/D can be clearly identified, also stressing the independence between the simulation errors and the geometry.

The Marten bundles do not seem to present an exceptionally high uncertainty. These bundles have a relatively low dispersion between their measurements and the C_{fbL}^{exp} slope, as shown in Figure 4.10. However, as these experiments were performed by the same authors and in the same laboratory, they share systematic errors. Therefore, since they represent a large share of the dataset (21 of 42 bundles), the systematic errors of the Marten bundles introduce an oversized bias to the dataset. The existing correlations, including the UCTD, rely on this experimental data for calibration, relying on the Marten work. This dependency between the calibration data and the predictions by UCTD can be why the over predictions of the Marten bundles are smaller for UCTD than for the ANN model. Conversely, UCTD predicts smaller C_{fbL}^{exp} for almost all the other bundles than the ANN model, under predicting most of the remaining dataset.

The ANN model is independent of this experimental dataset. Not even the geometries of the
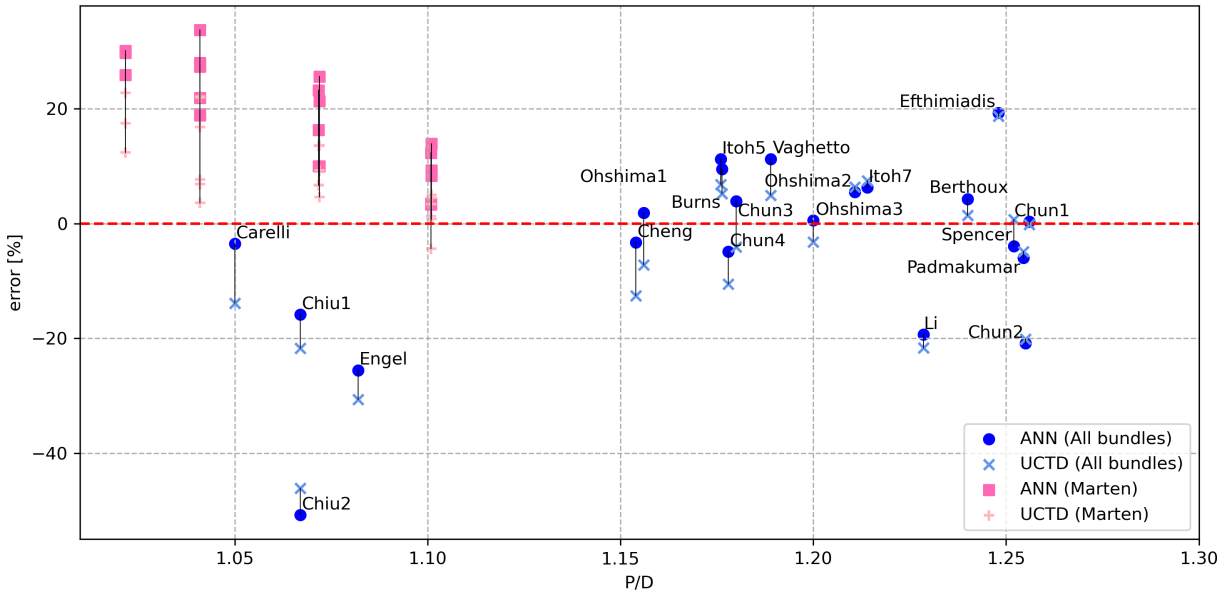
Figure 4.12: Relative error of C_{fbL} between the experimental data and the predictions as a function of P/D.
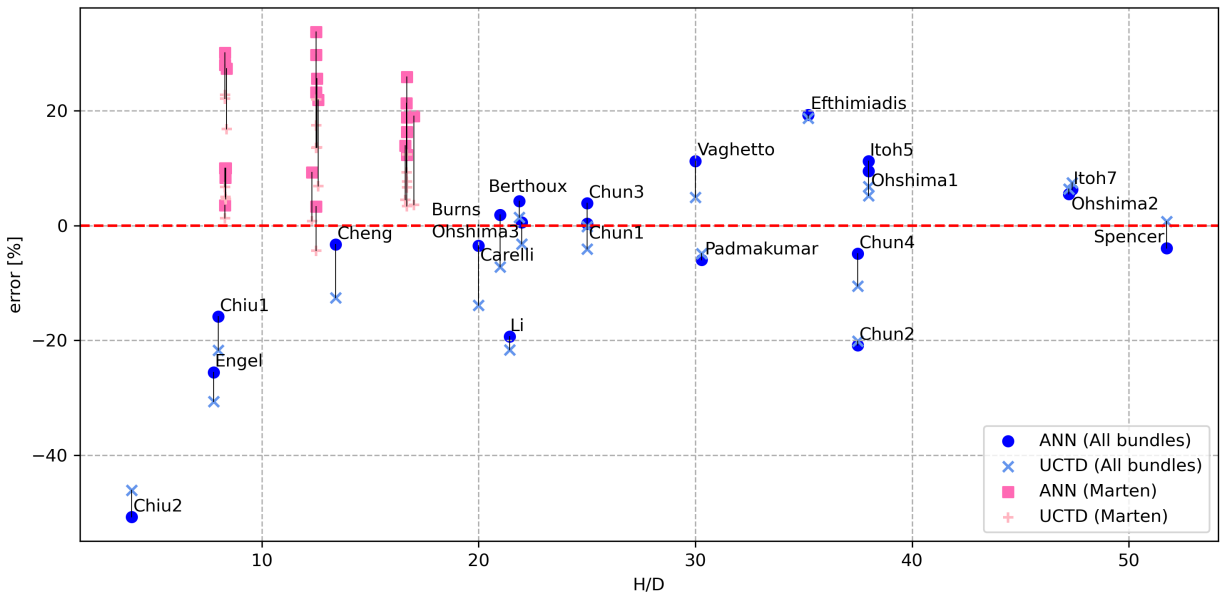

Figure 4.13: Relative error of C_{fbL} between the experimental data and the predictions as a function of H/D.

simulated bundles match with the ones of the experimental data. Apart from the excellent agree-
ment between the ANN predictions and the experimental data by itself, it is remarkable that the
accuracy of the ANN model is comparable to what a model calibrated in this same data can achieve.
The capacity of the ANN model to fit the experimental data is a complete result of its representa-
tion of the phenomena. From this perspective, the ANN model allows a statistical analysis of the
experimental dataset from an independent point of view that was not available before this work.

Tables 4.3 and 4.4 presents the error statistics of the ANN model and UCTD in the experi-
mental dataset considering all the bundles and removing the Marten bundles, respectively. When
considering all bundles, the considerably larger mean relative error in the ANN model results from
the strong bias associated with a large number of bundles from a single author. In Table 4.4, the
UCTD correlation has the largest mean relative error, an indication of how UCTD is skewed by
the fact that half of its calibration in the laminar regime is dependent on the bundles from Marten.
As see in Figures 4.12 and 4.13, the Marten bundles share similar P/D to Carelli, Chiu1, Chiu2
and Engel, and similar H/D to Chiu1, Chiu2, Engel and Cheng. None of these bundles confirm
the trends observed in the Marten bundles and are the work of different groups. The ANN model
performs considerably better than UCTD for all these bundles. Therefore, considering the superior
performance of the ANN model for all the bundles, including the ones similar to the Marten ones,
and its statistical independence to the experimental data, the error statistics excluding the Marten
bundles, are more representative of the relative performance between the ANN model and UCTD.

Table 4.3: Mean and RMS of the relative error in C_{fbL} (42 bundles).

$Model$	Mean relative error	RMS relative error
ANN	7.41%	3.37%
$UCTD$	1.21%	2.03%

Table 4.4: Mean and RMS of the relative error in C_{fbL} not considering the Marten [3, 4] experiments (21 bundles).

$Model$	Mean relative error	RMS relative error
ANN	-3.81%	2.48%
$UCTD$	-6.92%	2.63%

The amount of data available to verify the flow split is limited to the three bundles listed in Table **??**. The accuracy of the ANN model and UCTD are similar, with a too-small dataset to allow a clear distinction. The relevance of this result is that the flow split predictions of the ANN model are based on the training in the 93 simulated bundles. Hence they represent the set of physical rules from the CFD calculations throughout the dataset range. As shown in Figure 4.7, UCTD incurs in nonphysical behavior for low H/D. The ANN model performs similarly with the experimental data and is more reliable across all the geometries. The ANN can be considered a better predictor of flow split.

4.5 Conclusions

The ANN model presented in this section fully represents the statistics of the dataset of CFD simulations with high fidelity. Doing so provides a continuous function that corresponds to the CFD method by a fraction of the computational cost. This work demonstrated that when the ANN model is used in place of the UCTD correlation, it accurately predicts the experimental dataset. Unlike the empirical correlations calibrated with the experimental data, the ANN model is entirely independent of the experiments in its conception. This statistical independence means that the accuracy of the ANN is due only to the model representation of the phenomena. The statistical independence of the ANN model provided a unique insight into the importance of each experimental study to the dataset. This work made it clear that the fact that half of the experimental dataset is composed of experiments performed by the same author introduces a bias to the overall
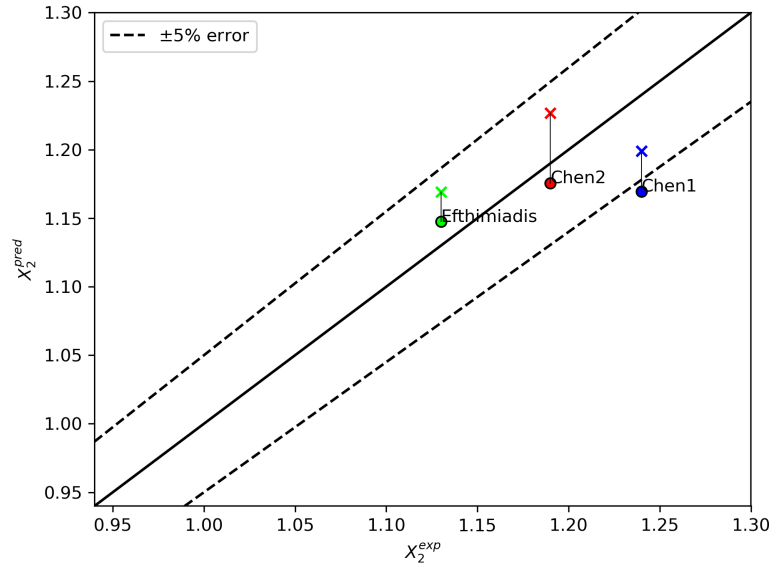
Figure 4.14: Comparison between the experimental data of X_2 and the predictions by the ANN model and UCTD.

statistics of the dataset. The ANN model also took advantage of the extended range of data of the CFD simulations. Since the ANN model based on the CFD dataset was representative of experiments, the CFD dataset provides more confidence that the ANN model is more accurate outside of the range of the experimental data than the extrapolations of the empirical correlations.

REFERENCES

[1] K. Deb and H. Jain, "An evolutionary many-objective optimization algorithm using reference-point-based nondominated sorting approach, part i: solving problems with box constraints," *IEEE transactions on evolutionary computation*, vol. 18, no. 4, pp. 577–601, 2013.

[2] Y. Liang, D. Zhang, Y. Chen, K. Zhang, W. Tian, S. Qiu, and G. Su, "An experiment study of pressure drop and flow distribution in subchannels of a 37-pin wire-wrapped rod bundle," *Applied Thermal Engineering*, vol. 174, p. 115283, 2020.

[3] K. Marten, S. Yonekawa, and H. Hoffmann, "Experimental investigation on pressure drop in tightly packed bundles with wire wrapped rods," in *IAHR Second International Specialists Meeting on Thermal-hydraulics in LMFBR Rod Bundles*, Rome, September, 1982, 1982.

[4] K. Marten, S. Yonekawa, and H. Hoffmann, "Experiments and correlations of pressure loss coefficients for hexagonal arranged rod bundles (p/d> 1.02) with helical wire spacers in laminar and turbulent flows," tech. rep., Kernforschungszentrum Karlsruhe GmbH (Germany, 1987.

[5] E. Merzari, A. Obabko, P. Fischer, and M. Aufiero, "Wall resolved large eddy simulation of reactor core flows with the spectral element method," *Nuclear Engineering and Design*, vol. 364, p. 110657, 2020.

[6] L. Brockmeyer, E. Merzari, J. Solberg, and Y. Hassan, "One-way coupled simulation of fiv in a 7-pin wire-wrapped fuel pin bundle," *Nuclear Engineering and Design*, vol. 356, p. 110367, 2020.

[7] N. Goth, P. Jones, T. D. Nguyen, R. Vaghetto, Y. Hassan, N. Salpeter, and E. Merzari, "Ptv/piv measurements of turbulent flows in interior subchannels of a 61-pin wire-wrapped hexagonal fuel bundle," *International Journal of Heat and Fluid Flow*, vol. 71, pp. 295–304, 2018.

[8] N. Goth, P. Jones, D. Nguyen, R. Vaghetto, Y. Hassan, A. Obabko, E. Merzari, and P. F. Fischer, "Comparison of experimental and simulation results on interior subchannels of a 61-pin wire-wrapped hexagonal fuel bundle," *Nuclear Engineering and Design*, vol. 338, pp. 130–136, 2018.

[9] M. S. Song, J.-H. Jeong, and E. S. Kim, "Flow visualization on sfr wire-wrapped 19-pin bundle geometry using mir-piv-plif and comparisons with rans-based cfd analysis," *Annals of Nuclear Energy*, vol. 147, p. 107653, 2020.

[10] M. Childs, R. Muyshondt, R. Vaghetto, D. T. Nguyen, and Y. Hassan, "Experimental study on the effect of localized blockages on the friction factor of a 61-pin wire-wrapped bundle," *Journal of Fluids Engineering*, vol. 142, no. 11, p. 111211, 2020.

[11] K. Rehme, "Geometry-dependence of the pressure loss in rod bundles with coiled wire spacers and longitudinal flow," *Translation of Dissertation*, 1967.

[12] W. Baumann, V. Casal, H. Hoffmann, R. Möller, and K. Rust, "Brennelemente mit wendelförmigen abstandshaltern für schnelle brutreaktoren," *KfK-768. Also EURFNR-571*, 1968.

[13] T. Reihman, "An experimental study of pressure drop in wire wrapped fftf assemblies," *Report No. BNWL-1207*, 1969.

[14] E. Novendstern, "Turbulent flow pressure drop model for fuel rod assemblies utilizing a helical wire-wrap spacer system," *Nuclear Engineering and Design*, vol. 22, no. 1, pp. 28–42, 1972.

[15] K. Rehme, "Pressure drop correlations for fuel element spacers," *Nuclear technology*, vol. 17, no. 1, pp. 15–23, 1973.

[16] F. Engel, R. Markley, and A. Bishop, "Laminar, transition, and turbulent parallel flow pressure drop across wire-wrap-spaced rod bundles," *Nuclear science and engineering*, vol. 69, no. 2, pp. 290–296, 1979.

[17] S.-K. Cheng and N. E. Todreas, "Hydrodynamic models and correlations for bare and wire-wrapped hexagonal rod bundles—bundle friction factors, subchannel friction factors and mixing parameters," *Nuclear engineering and design*, vol. 92, no. 2, pp. 227–251, 1986.

[18] S. Chen, R. Petroski, and N. Todreas, "Numerical implementation of the cheng and todreas correlation for wire wrapped bundle friction factors-desirable improvements in the transition flow region," *Nuclear Engineering and Design*, vol. 263, pp. 406–410, 2013.

[19] S. Chen, Y. Chen, and N. Todreas, "The upgraded cheng and todreas correlation for pressure drop in hexagonal wire-wrapped rod bundles," *Nuclear Engineering and Design*, vol. 335, pp. 356–373, 2018.

[20] G. C. Tomaz, Y. M. Chen, R. Vaghetto, and Y. Hassan, "Recalibration of the uctd correlation for friction factor in wire-wrapped rod bundles using multi-objective genetic algorithms," in *The 19th International Topical Meeting on Nuclear Reactor Thermal Hydraulics, NURETH-19*, 2022.

[21] R. Grazzini and D. Tirelli, "Experimental determination of pressure drop of pec reactor fuel element," tech. rep., Comitato Nazionale per l'Energia Nucleare, 1971.

[22] R. R. Sahu, V. Prakash, R. Prabhakar, and R. D. Kale, "Influence of spacer wire lead on the pressure drop in prototype fast breeder reactor subassembly," in *The Seventh Asian Congress of Fluid Mechanics*, p. 593, Allied Publishers, 1997.

[23] M.-H. Chun and K.-W. Seo, "An experimental study and assessment of existing friction factor correlations for wire-wrapped fuel assemblies," *Annals of nuclear energy*, vol. 28, no. 17, pp. 1683–1695, 2001.

[24] S. K. Choi, I. K. Choi, H. Y. Nam, J. H. Choi, and H. K. Choi, "Measurement of pressure drop in a full-scale fuel assembly of a liquid metal reactor," *J. Pressure Vessel Technol.*, vol. 125, no. 2, pp. 233–238, 2003.

[25] M. Berthoux and T. Cadiou, "The thermal hydraulics in a rod bundle representative of the start-up core of the allegro gas cooled fast reactor—experimental and numerical approaches," *Nuclear engineering and design*, vol. 240, no. 10, pp. 3372–3386, 2010.

[26] G. Kennedy, K. Van Tichelen, and H. Doolaard, "Experimental investigation of the pressure loss characteristics of the full-scale myrrha fuel bundle in the complot lbe facility," in *Proc. 16th Int. Conf. Nuclear Reactor Thermal-Hydraulics (NURETH-16)*, p. 61, 2015.

[27] S.-K. Chang, D.-J. Euh, H. S. Choi, H. Kim, S. R. Choi, and H.-Y. Lee, "Flow distribution and pressure loss in subchannels of a wire-wrapped 37-pin rod bundle for a sodium-cooled fast reactor," *Nuclear Engineering and Technology*, vol. 48, no. 2, pp. 376–385, 2016.

[28] S.-K. Chang, D.-J. Euh, S. Kim, H. S. Choi, H. Kim, Y. J. Ko, S. R. Choi, and H.-Y. Lee, "Experimental study of the flow characteristics in an sfr type 61-pin rod bundle using iso-kinetic sampling method," *Annals of Nuclear Energy*, vol. 106, pp. 160–169, 2017.

[29] H. Ohshima and Y. Imai, "Numerical simulation method of thermal-hydraulics in wire-wrapped fuel pin bundle of sodium-cooled fast reactor," 2017.

[30] G. Padmakumar, K. Velusamy, B. Prasad, and K. Rajan, "Hydraulic characteristics of a fast reactor fuel subassembly: An experimental investigation," *Annals of Nuclear Energy*, vol. 102, pp. 255–267, 2017.

[31] J. Pacio, K. Litfin, T. Wetzel, G. Kennedy, and K. Van Tichelen, "Thermal-hydraulic experiments supporting the myrrha fuel assembly," 2017.

[32] R. Vaghetto, P. Jones, N. Goth, M. Childs, S. Lee, D. Thien Nguyen, and Y. A. Hassan, "Pressure measurements in a wire-wrapped 61-pin hexagonal fuel bundle," *Journal of Fluids Engineering*, vol. 140, no. 3, 2018.

[33] D. Fan, T. Peng, Y. Tang, Q. Zhao, W. Tian, D. Liu, R. Li, D. Wang, and L. Gu, "Periodicity and transversal pressure distribution in a wire-wrapped 19-pin fuel assembly," *International Journal of Energy Research*, vol. 45, no. 8, pp. 11837–11850, 2021.

[34] T. Eppinger, K. Seidler, and M. Kraume, "Dem-cfd simulations of fixed bed reactors with small tube to particle diameter ratios," *Chemical Engineering Journal*, vol. 166, no. 1, pp. 324–331, 2011.

[35] A. G. Dixon, M. Nijemeisland, and E. H. Stitt, "Systematic mesh development for 3d cfd simulation of fixed beds: contact points study," *Computers & Chemical Engineering*, vol. 48, pp. 135–153, 2013.

[36] S. Rebughini, A. Cuoci, and M. Maestri, "Handling contact points in reactive cfd simulations of heterogeneous catalytic fixed bed reactors," *Chemical Engineering Science*, vol. 141, pp. 240–249, 2016.

[37] U. Bieder, V. Barthel, F. Ducros, P. Quéméré, and S. Vandroux, "Cfd calculations of wire wrapped fuel bundles: modeling and validation strategies," in *Workshop Proceedings of Computational Fluid Dynamics for Nuclear Reactor Safety Applications (CFD4NRS-3)*, p. 90, 2010.

[38] M.-O. G. Delchini, E. L. Popov, and D. W. Pointer, "Simulations of the turbulent flow in the thermal-hydraulic out-of-reactor safety (thors) with the cfd code star-ccm+1,"

[39] J.-H. Jeong, M.-S. Song, and K.-L. Lee, "Rans based cfd methodology for a real scale 217-pin wire-wrapped fuel assembly of kaeri pgsfr," *Nuclear Engineering and Design*, vol. 313, pp. 470–485, 2017.

[40] O. Bovati, M. A. Yildiz, Y. Hassan, and R. Vaghetto, "Rans simulations for transition and turbulent flow regimes in wire-wrapped rod bundles," *International Journal of Heat and Fluid Flow*, vol. 90, p. 108838, 2021.

[41] R. Gajapathy, K. Velusamy, P. Selvaraj, P. Chellapandi, and S. Chetal, "Cfd investigation of helical wire-wrapped 7-pin fuel bundle and the challenges in modeling full scale 217 pin bundle," *Nuclear Engineering and Design*, vol. 237, no. 24, pp. 2332–2342, 2007.

[42] P. Zhao, J. Liu, Z. Ge, X. Wang, and X. Cheng, "Cfd analysis of transverse flow in a wire-wrapped hexagonal seven-pin bundle," *Nuclear Engineering and Design*, vol. 317, pp. 146–157, 2017.

[43] K. Podila and Y. Rao, "Assessment of cfd for the canadian scwr bundle with wire wraps," *Progress in Nuclear Energy*, vol. 77, pp. 373–380, 2014.

[44] I. B. Celik, U. Ghia, P. J. Roache, and C. J. Freitas, "Procedure for estimation and reporting of uncertainty due to discretization in cfd applications," *Journal of fluids Engineering-Transactions of the ASME*, vol. 130, no. 7, 2008.

[45] M. Abadi, A. Agarwal, P. Barham, E. Brevdo, Z. Chen, C. Citro, G. S. Corrado, A. Davis, J. Dean, M. Devin, S. Ghemawat, I. Goodfellow, A. Harp, G. Irving, M. Isard, Y. Jia, R. Jozefowicz, L. Kaiser, M. Kudlur, J. Levenberg, D. Mané, R. Monga, S. Moore, D. Murray, C. Olah, M. Schuster, J. Shlens, B. Steiner, I. Sutskever, K. Talwar, P. Tucker, V. Vanhoucke, V. Vasudevan, F. Viégas, O. Vinyals, P. Warden, M. Wattenberg, M. Wicke, Y. Yu, and X. Zheng, "TensorFlow: Large-scale machine learning on heterogeneous systems," 2015. Software available from tensorflow.org.

[46] A. Paszke, S. Gross, F. Massa, A. Lerer, J. Bradbury, G. Chanan, T. Killeen, Z. Lin, N. Gimelshein, L. Antiga, A. Desmaison, A. Kopf, E. Yang, Z. DeVito, M. Raison, A. Tejani, S. Chilamkurthy, B. Steiner, L. Fang, J. Bai, and S. Chintala, "Pytorch: An imperative style, high-performance deep learning library," in *Advances in Neural Information Processing Systems 32* (H. Wallach, H. Larochelle, A. Beygelzimer, F. d'Alché-Buc, E. Fox, and R. Garnett, eds.), pp. 8024–8035, Curran Associates, Inc., 2019.

[47] G. Cybenko, "Approximation by superpositions of a sigmoidal function," *Mathematics of control, signals and systems*, vol. 2, no. 4, pp. 303–314, 1989.

[48] K. Hornik, "Approximation capabilities of multilayer feedforward networks," *Neural networks*, vol. 4, no. 2, pp. 251–257, 1991.

[49] U. Shaham, A. Cloninger, and R. R. Coifman, "Provable approximation properties for deep neural networks," *Applied and Computational Harmonic Analysis*, vol. 44, no. 3, pp. 537–557, 2018.

[50] G. Sun and S. Wang, "A review of the artificial neural network surrogate modeling in aerodynamic design," *Proceedings of the Institution of Mechanical Engineers, Part G: Journal of Aerospace Engineering*, vol. 233, no. 16, pp. 5863–5872, 2019.

[51] K. Elsayed and C. Lacor, "Cfd modeling and multi-objective optimization of cyclone geometry using desirability function, artificial neural networks and genetic algorithms," *Applied Mathematical Modelling*, vol. 37, no. 8, pp. 5680–5704, 2013.

[52] S. Sahebzadeh, A. Rezaeiha, and H. Montazeri, "Cfd-based surrogate modelling of urban wind farms using artificial neural networks: double rotor arrangements," in *Journal of Physics: Conference Series*, vol. 2042, p. 012093, IOP Publishing, 2021.

[53] H. C. Kim, S. H. Han, and Y. J. Lee, "Integrity monitoring method for dry storage casks using artificial neural network," *Nuclear Engineering and Design*, vol. 366, p. 110741, 2020.

[54] X. Guo, W. Li, and F. Iorio, "Convolutional neural networks for steady flow approximation," in *Proceedings of the 22nd ACM SIGKDD international conference on knowledge discovery and data mining*, pp. 481–490, 2016.

[55] F. Agostinelli, M. Hoffman, P. Sadowski, and P. Baldi, "Learning activation functions to improve deep neural networks," *arXiv preprint arXiv:1412.6830*, 2014.

[56] H. Tang, K. C. Tan, and Z. Yi, *Neural networks: computational models and applications*, vol. 53. Springer Science & Business Media, 2007.

[57] D. E. Rumelhart, G. E. Hinton, and R. J. Williams, "Learning representations by back-propagating errors," *nature*, vol. 323, no. 6088, pp. 533–536, 1986.

[58] J. Duchi, E. Hazan, and Y. Singer, "Adaptive subgradient methods for online learning and stochastic optimization.," *Journal of machine learning research*, vol. 12, no. 7, 2011.

[59] T. Tieleman and G. Hinton, "Lecture 6.5-rmsprop, coursera: Neural networks for machine learning," *University of Toronto, Technical Report*, vol. 6, 2012.

[60] L. Deng, J. Li, J.-T. Huang, K. Yao, D. Yu, F. Seide, M. Seltzer, G. Zweig, X. He, J. Williams, *et al.*, "Recent advances in deep learning for speech research at microsoft," in *2013 IEEE International Conference on Acoustics, Speech and Signal Processing*, pp. 8604–8608, IEEE, 2013.

[61] G. Hinton, L. Deng, D. Yu, G. E. Dahl, A.-r. Mohamed, N. Jaitly, A. Senior, V. Vanhoucke, P. Nguyen, T. N. Sainath, *et al.*, "Deep neural networks for acoustic modeling in speech recognition: The shared views of four research groups," *IEEE Signal processing magazine*, vol. 29, no. 6, pp. 82–97, 2012.

[62] D. P. Kingma and J. Ba, "Adam: A method for stochastic optimization," *arXiv preprint arXiv:1412.6980*, 2014.

[63] L. Huang, Y. Zhou, F. Zhu, L. Liu, and L. Shao, "Iterative normalization: Beyond standardization towards efficient whitening," in *Proceedings of the IEEE/CVF Conference on Computer Vision and Pattern Recognition*, pp. 4874–4883, 2019.

[64] H. Kim, Y. M. Chen, and Y. Hassan, "Prediction of pressure drop in hexagonal wire-wrapped rod bundles using artificial neural network," *Nuclear Engineering and Design*, vol. 381, p. 111365, 2021.

[65] D. Krstajic, L. J. Buturovic, D. E. Leahy, and S. Thomas, "Cross-validation pitfalls when selecting and assessing regression and classification models," *Journal of cheminformatics*, vol. 6, no. 1, pp. 1–15, 2014.

[66] J. Pacio, S.-K. Chen, Y.-M. Chen, and N. Todreas, "Analysis of pressure losses and flow distribution in wire-wrapped hexagonal rod bundles for licensing. part ii: Evaluation of public experimental data," *Nuclear Engineering and Design*, p. 111606, 2021.